Numerical Modeling of Subglacial Sediment Deformation

Anders Damsgaard

PhD dissertation, July 2015
Department of Geoscience, Graduate School of Science and Technology, Aarhus University

Numerical Modeling of Subglacial Sediment Deformation

Anders Damsgaard

Department of Geoscience
Graduate School of Science and Technology
Aarhus University

anders.damsgaard@geo.au.dk
https://cs.au.dk/~adc

PhD dissertation
July 2015

Supervisor
Prof. David Lundbek Egholm
Department of Geoscience, Aarhus University, Denmark

Co-supervisor
Prof. Jan A. Piotrowski
Department of Geoscience, Aarhus University, Denmark

External supervisor
Prof. Slawek Tulaczyk
Department of Earth and Planetary Sciences, University of California Santa Cruz, USA

Evaluation committee
Dr. Anders Vest Christiansen (chairman)
Department of Geoscience, Aarhus University, Denmark

Dr. Poul Christoffersen
Scott Polar Research Institute and Department of Geography, University of Cambridge, UK

Prof. Martin Truffer
Geophysical Institute, University of Alaska Fairbanks, USA

PhD submission
July 3rd, 2015

Address
Department of Geoscience
Aarhus University
Høegh-Guldbergs Gade 2
DK-8000 Aarhus C
Denmark
Phone: (+45) 87 15 45 00
E-mail: `geologi@au.dk`

Cover image
Canadian Rockies photographed on the way to American Geophysical Union Fall Meeting 2014.

This thesis was created using the LaTeX 2_ε markup language and the Memoir document class. The text is set in Charter and FiraSans, and the source code is set in `Source Code Pro`. This document is formatted for two-sided printing.

Abstract

Glacier and ice sheet mass balance is sensitive to climate change. The geological record has revealed that the polar ice sheets in the past responded rapidly to periods of warming, most likely caused by dynamic changes in ice flow patterns. The rapid ice-sheet dynamical changes observed in the past may cause mass loss in the near future to exceed current best estimates.

Ice flow in larger ice sheets focuses in fast-moving streams due to mechanical non-linearity of ice. These ice streams often move at velocities several magnitudes larger than surrounding ice and consequentially constitute a majority of the ice-sheet mass flux. Understanding their physical behavior and sensitivity to changes is of greatest importance for describing ice sheet configuration in the past, present and future.

In-situ measurements and interpretations from the Pleistocene sedimentary record have revealed that many glaciers move by deforming their sedimentary beds. Several modern ice streams, in particular, move as plug flows due to basal sediment deformation. An intense and long-winded discussion about the appropriate description for subglacial sediment mechanics followed this discovery, with good reason. The mechanical behavior is likely very important for the evolution of ice-sheet flow in a changing climate, and secondly directly influences the genesis of subglacial landforms seen in previously glaciated areas.

Previous studies of subglacial sediment mechanics have relied on field and laboratory experiments. The approach in this PhD project has been to understand fundamental granular and fluid deformation, and apply the insights to improve the understanding the processes governing mechanical stability of subglacial granular materials. For this purpose a numerical formulation for granular and fluid mechanics has been implemented and applied. The computational approach allowed for analysis in unsurpassed detail during progressive deformation.

The computational experiments show that granular deformation at glacial velocities conforms to the rate-independent Mohr-Coulomb plasticity. In select cases, however, viscous effects from meltwater deformation can provide additional rate-dependent strengthening. The strengthening may act to stabilize patches of the deforming bed, triggering differential advection and hydrological exchange between the bed and the ice-bed interface.

We also show that granular advection during shear deformation is dependent on effective pressure, potentially causing unstable growth of bumps at the ice-bed interface. The process creates wavy subglacial bumps similar to common geomorphological features in past glaciated areas, but the proposed instability mechanism was until now incompatible with commonly accepted till rheology models.

Variation in pore-water pressure causes reorganization in the internal stress network and leads to slow creeping deformation. The rate of creep is non-linearly dependent on the applied stresses. Granular creep can explain slow glacial velocities previously associated with elastic or viscous ice deformation. If a glacier dominated by subglacial creep experiences prolonged events of strong surface melt or increased driving stresses, the plastic strength limit can cause rapid acceleration downslope due to imbalance of stresses.

Dansk sammendrag (Summary in Danish)

Massebalancen af gletsjere og store iskapper er følsom overfor klimaforandringer. Den geologiske stratigrafi har vist at indlandsisen på Antarktis, Grønland og de tidligere ismasser i Nordeuropa og Nordamerika hurtigt reagerede på varmere klimaforhold, hvilket højest sandsynligt skyldes ændringer i deres flydemønstre. Disse hurtige ændringer kan forårsage afsmeltning af is i den nære fremtid der overgår de bedste nuværende estimater.

Bevægelsen af is i større isskjolde fokuseres i hurtigt flydende isstrømme på grund af mekanisk non-linearitet af is. Disse isstrømme bevæger sig flere magnituder hurtigere end den omkringliggende is, og forårsager derfor hoveddelen af istransporten fra områder med total akkumulation indlands til kystområder med massetab til smeltning og kælving. Det er derfor nødvændigt at forstå deres fysiske forhold og følsomhed overfor ændringer for at kunne beskrive ismassernes konfiguration i fortiden, nutiden og fremtiden. Målinger og tolkninger fra nutidige og gletsjerafjelringer fra Pleistocæn har vist at mange gletsjere bevæger sig ved at deformere deres sedimentære underlag, og flere nutidige isstrømme bevæger sig udelukkende grundet underlagets deformation. Denne opdagelse startede en intens debat omkring hvilken matematisk formulering der er bedst dækkende for sedimenternes mekaniske egenskaber. Det er vigtigt at forstå disse deformationsprocesser da de potentielt er meget vigtig for udviklingen af indlandsis under et skiftende klima og er grundlæggende for dannelsen af landskabstræk der ses i tidligere glacierede områder.

Tidligere studer af gletsjersedimenternes mekanik har bygget på målinger i felten og ved laboratorieeksperimenter. Tilgangen har i dette PhD projekt været at forsøge at forstå grundlæggende processer under deformation af granulære materialer og væsker, og at anvende den opnåede indsigt til at forstå hvilke processer der styrer de mekaniske egenskaber af sedimentære lag under is. Til dette formål er en numerisk formulering for granulær og væskemekanik implementeret og anvendt. Denne tilgang har tilladt hidtil uovertruffent detaljerede analyser under igangværende deformation.

Computereksperimenterne viser at granulær deformation ved glaciale hastigheder følger den rateuafhængige Mohr-Coulomb plasticitet. I særlige tilfælde viser det sig dog at viskøse effekter fra smeltevandet mellem sedimentkornene kan forårsage forstærkning af sedimentet som er afhængig af deformationsraten. Forstærkningen kan stabilisere områder i det sedimentære underlag hvilket ændrer mønstret af sedimenttransport og driver vandudveksling mellem sediment og gletsjerunderlag. Vi viser også at granulær transport under deformation afhænger af det effektive stress, hvilket kan skabe ustabil vækst af forhøjninger ved gletsjerunderlaget. Processen danner bølgede topografier som har fælles træk til hyppigt observerede landskabsformer i tidligere glacierede områder. Hypotesen omkring ustabil vækst har tidligere været inkompatibel med alment accepterede modeller for sedimentmekanik. Ændringer i porevandstryk viser sig at drive reorganisering i det interne stressnetværk og kan forårsage langsom krybende sedimentdeformation. Hastigheden af kryb afhænger af de påførte stresser. Granulært kryb kan forklare langsomme ishastigheder som tidligere har været forbundet med elastisk eller viskøs deformation af isen selv. Hvis en gletsjer, hvis bevægelse er domineret af dette kryb, pludseligt oplever længere perioder med høj overfladeafsmeltning eller større drivende stresser, kan den plastiske grænse for sedimentstyrke forårsage kraftig acceleration grundet uligevægt af systemets stresser.

Acknowledgments

I would like to express the highest appreciation for my supervisor David L. Egholm, that for the entirety of my PhD studies has showed the greatest generosity with time and funds for tools and traveling. Through countless friendly and patient conversations he has helped me understand the physical and mathematical concepts along the way.

Jan Piotrowski is thanked for encouraging me to seek a PhD fellowship, and for introducing to glaciology and glacial sedimentology. My interest in the field was developed through excellent lectures that in a pertinent manner presented the past and current hot research topics in the field.

I thank Slawek Tulaczyk and his group for hospitality during my stays at the University of California, Santa Cruz. Through the time spent there I gained a strong interest in understanding physical processes in the West Antarctic Ice Sheet.

The coauthors of my papers are thanked for helpful discussions, their ability to see opportunities, for helping evolve ideas, and for putting the results into a wider perspective.

I would also like to thank my fellow PhD students at the Department of Geoscience, Aarhus University, who made it possible to combine work and play which made a way the last four years fly by. The Department of Geoscience and the Graduate School of Science and Technology have provided great surroundings for the study.

Finally, I would like to thank my family, Susan and Sonja, and closest relatives for supporting me through it all.

Preface

The PhD project was carried out at the Department of Geoscience, Aarhus University, including a total of two months research stay at the Department of Earth and Planetary Sciences, University of California Santa Cruz, USA.

The PhD study started May 1 2011, and has been supervised by Prof. David Lundbek Egholm, Prof. Jan A. Piotrowski (both Aarhus University (AU)) and Prof. Slawek Tulaczyk (University of California, Santa Cruz). Other collaborators include Nicolaj Krogh Larsen (AU), Christian Fredborg Brædstrup (AU), Lucas H. Beem (California Institute of Technology) and Karol Tylmann (Nicolaus Copernicus University in Toruń). The project ends with the submission of this dissertation on July 3 2015.

The PhD project was part of the *Ice, Water and Sediment* (IWS) research initiative led by Prof. David Lundbek Egholm. The overarching goal of the IWS project is to improve the understanding of different subglacial processes and their interplay by linking geological observations to basic physical principles in computational models. The IWS project was funded by the Danish Council for Independent Research (DFF) under the Sapere Aude programme, and the Graduate School of Science and Technology, Aarhus University, cofunded this PhD project.

The thesis is based on the following papers, which constitute the principal scientific contribution:

1. A. Damsgaard, D.L. Egholm, J.A. Piotrowski, S. Tulaczyk, N.K. Larsen, and K. Tylmann. Discrete element modeling of subglacial sediment deformation. *Journal of Geophysical Research: Earth Surface*. 118, 2230–2242 (2013).

2. A. Damsgaard, D.L. Egholm, J.A. Piotrowski, S. Tulaczyk, N.K. Larsen, and C.F. Brædstrup. A new methodology to simulate subglacial deformation of water saturated granular material. *Submitted to The Cryosphere*.

3. A. Damsgaard, D.L. Egholm, L.H. Beem, N.K. Larsen, S. Tulaczyk, and J.A. Piotrowski. Creep, stick and slip in subglacial granular beds forced by variations in melt-water pressure. *In prep*.

The papers are accompanied by a review in order to (i) introduce research questions that have formed the basis of this study (chapter 1), (ii) present results and discuss the implications of these findings in the broader context of the scientific field (chapter 2), and (iii) draw up the conclusions from this work and mention future aspects (chapter 3). After the research articles (chapters 4–6) the thesis concludes with two chapters expanding on the applied numerical methodologies, intended to familiarize the reader with design choices and the computational framework (chapters 7 and 8).

The listed papers and the present summary make up the dissertation, which has been submitted to the Faculty of Science and Technology, Aarhus University, Denmark.

Paper not included in the thesis

4. C.F. Brædstrup, A. Damsgaard, D.L. Egholm. Ice-sheet modelling accelerated by graphics cards. *Computers & Geosciences*. 72, 210–220 (2014).

Published abstracts not included in the thesis

Publications before 2013 bear my previous name "A.D. Christensen".

1. A.D. Christensen, D.L. Egholm, and J.A. Piotrowski. Numerical modelling of subglacial sediment deformation. Geophysical Research Abstracts. 13, EGU2011-7829.

2. A.D. Christensen, D.L. Egholm, and J.A. Piotrowski. Numerical modelling of sediment deformation by glacial stress. International Union for Quaternary Research Congress 2011, Bern, Switzerland.

3. A.D. Christensen, D.L. Egholm, J.A. Piotrowski, and S. Tulaczyk. Discrete element modelling of subglacial sediment deformation. Geophysical Research Abstracts. 14, EGU2012-2931.

4. O.R. Clausen, D.L. Egholm, R. Wesenberg, and A.D. Christensen. Salt movements and faulting of the overburden — can numerical modeling predict the fault patterns above salt structures? Geophysical Research Abstracts. 14, EGU2012-1615.

5. J.A. Piotrowski, K. Tylmann, W. Narloch, W. Wysota, A. Damsgaard, D.L. Egholm, N.K. Larsen, and J. Lesemann. Subglacial mosaic of stable and deforming spots under the Scandinavian Ice Sheet: field, laboratory and numerical data. Canadian Quaternary Association biannual meeting, Aug. 2013.

6. A. Damsgaard, D.L. Egholm, J.A. Piotrowski, S. Tulaczyk and N.K. Larsen. Numerical modelling of granular subglacial deformation using the discrete element method. Geophysical Research Abstracts. 15, EGU2013-4026.

7. C.F. Brædstrup, D.L. Egholm, S.V. Ugelvig, A. Damsgaard, and J.L. Andersen. Feedbacks between subglacial dynamics and long-term glacial landscape evolution. American Geophysical Union Fall Meeting 2013, San Francisco, CA, USA.

8. A. Damsgaard, D.L. Egholm, J.A. Piotrowski, S. Tulaczyk, and N.K. Larsen. Discrete element modeling of subglacial sediment deformation. American Geophysical Union Fall Meeting 2013, San Francisco, CA, USA.

9. A. Damsgaard, D.L. Egholm, J.A. Piotrowski, S. Tulaczyk, N.K. Larsen, and C.F. Brædstrup. Numerical modeling of particle-fluid mixtures in a subglacial setting. American Geophysical Union Fall Meeting 2014, San Francisco, CA, USA.

10. A. Damsgaard, D.L. Egholm, J.A. Piotrowski, S. Tulaczyk, and N.K. Larsen. Oscillations in till strength due to particle-fluid feedbacks. International Union for Quaternary Research Congress, 2015, Nagoya, Japan.

Conferences

1. European Geosciences Union (EGU), General Assembly, Vienna, Austria. April 4–8, 2011. Poster presentation.

2. XVIII International Union for Quaternary Research (INQUA) Congress, Bern, Switzerland. July 21–27, 2011. Poster presentation.

3. European Geosciences Union (EGU), General Assembly, Vienna, Austria. April 22–27, 2012. Two poster presentations.

4. European Geosciences Union (EGU), General Assembly, Vienna, Austria. April 7–12, 2013. Poster presentation.

5. Society for Industrial and Applied Mathematics, Conference on Mathematical and Computational Issues in the Geosciences. June 17–20, 2013.

6. III International Conference on Particle-Based Methods. Fundamentals and Applications, Stuttgart, Germany. September 18–20, 2013.

7. American Geophysical Union (AGU), Fall Meeting, San Francisco, USA. December 9–13, 2013. Oral presentation.

8. American Geophysical Union (AGU), Fall Meeting, San Francisco, USA. December 15–19, 2014. Poster presentation.

9. XIX International Union for Quaternary Research (INQUA) Congress, Nagoya, Japan. July 26 to August 2, 2015. Oral presentation.

Contents

List of Figures

List of Tables

Acronyms and abbreviations

CFD computational fluid dynamics. 64, 110, 114

CFL Courant-Friedrichs-Lewy. 62, 114

CUDA compute unified device architecture. 64, 90

DEM discrete element method. x, 2, 16, 27, 28, 36–39, 41–44, 46–56, 60, 97–104, 110, 114, 117

FDM finite difference method. 39, 110, 112

FEM finite element method. 39, 110

FVM finite volume method. 39, 110

GPU graphics processing unit. 27, 62, 64, 90, 103

IBI ice-bed interface. 8, 16, 19–21, 23–25, 28, 49, 58, 79

LBM Lattice Boltzmann method. 110

MD molecular dynamics. 100

NS Navier-Stokes. 110, 111

SPH smoothed-particle hydrodynamics. 110

WIS Whillans Ice Stream (previously named Ice Stream B). 5, 10, 15, 19

Symbols

A dot denotes that the symbol is a temporal derivative while bold symbols denote multidimensional vectors.

β fluid solver parameter [-]. 111, 112

$\beta_{\mathbf{f}}$ fluid adiabatic compressibility [Pa^{-1}]. 61, 66, 93, 95, 115, 116

C cohesion [Pa]. 10

d particle diameter [m]. 63

$\boldsymbol{\delta}$ Kronecker delta (identity matrix), $\delta_{ij} = 1$ for $i = j$ and $\delta_{ij} = 0$ for $i \neq j$. 7

$\dot{\boldsymbol{\delta}}$ inter-particle contact displacement velocity [$\mathrm{m\,s}^{-1}$]. 41

$\delta_{\mathbf{n}}$ inter-particle contact normal displacement [m]. 30, 40, 60, 90, 91, 101

$\dot{\delta}_{\mathbf{n}}$ inter-particle contact normal displacement velocity [$\mathrm{m\,s}^{-1}$]. 30, 41, 101, 102

$\boldsymbol{\delta}_{\mathbf{t}}$ inter-particle contact tangential displacement [m]. 30, 40, 90, 91, 102

$\dot{\boldsymbol{\delta}}_{\mathbf{t}}$ inter-particle contact tangential displacement velocity [$\mathrm{m\,s}^{-1}$]. 30, 41, 102

Δx cell size along x [m]. 116

Δy cell size along y [m]. 116

Δz cell size along z [m]. 116

E Young's modulus [Pa]. 101

$\boldsymbol{\epsilon}$ strain tensor [-]. 7, 8

$\dot{\boldsymbol{\epsilon}}$ strain rate tensor [s^{-1}]. 8

$\boldsymbol{F}$ sum of body forces [N]. 92, 100

$\boldsymbol{f}_{\mathbf{g}}$ gravitational force vector [N]. 91, 100

$\boldsymbol{F_i}$ interaction force between solid and fluid phase per fluid volume [$\mathrm{N\,m^{-3}}$]. 111, 113

$\boldsymbol{f_i}$ interaction force between solid and fluid phase [N]. 60, 63, 64, 113

$\boldsymbol{f_n}$ normal inter-particle contact force vector [N]. 30, 40, 41, 60, 90, 91, 100–102

$\boldsymbol{f_t}$ tangential inter-particle contact force vector [N]. 30, 40, 41, 60, 90, 91, 100, 102

$\boldsymbol{g}$ gravitational acceleration vector [$\mathrm{m\,s^{-2}}$]. 40, 64, 66, 91, 92, 95, 100, 110, 111

γ shear strain [-]. 8, 12, 51

$\dot{\gamma}$ shear strain rate [$\mathrm{s^{-1}}$]. 8–12, 18, 38

γ_n grain contact-normal viscosity [N/(m/s)]. 30, 101

γ_t grain contact-tangential viscosity [N/(m/s)]. 30, 102

I inertia parameter [-]. 38, 40, 43, 66, 100

i particle index [-]. 40, 60, 90, 100, 102, 113

j particle index [-]. 40, 60, 90, 100

k intrinsic permeability [$\mathrm{m^2}$]. 61, 63, 67, 93, 115, 116

k_c intrinsic permeability prefactor [$\mathrm{m^2}$]. 63, 64, 66–68, 70, 93

k_n inter-particle normal elastic stiffness [$\mathrm{N\,m^{-1}}$]. 40–43, 60, 66, 90, 95, 101

k_t inter-particle tangential elastic stiffness [$\mathrm{N\,m^{-1}}$]. 40–43, 60, 66, 90, 91, 95, 102

$\boldsymbol{L}$ spatial domain size [m]. 43, 66

m particle mass [kg]. 40, 41, 60, 92, 100

μ internal friction coefficient [-]. 10, 60, 95

μ_d inter-particle dynamic friction coefficient [-]. 41–43

μ_f dynamic fluid viscosity [Pa s]. 61, 66, 93, 95, 111, 115, 116

μ_s inter-particle static friction coefficient [-]. 41–43, 102

m_w wall mass [kg]. 43, 66

N effective normal stress [Pa]. 9–12, 18, 23, 85, 95, 96

$\boldsymbol{n}$ inter-particle contact normal unit vector [-]. 40, 41, 60, 91, 92, 100–102

n_c particle contact set [-]. 40, 100

N_p number of particles [-]. 43, 66, 95

ν Poisson's ratio [-]. 101

$\boldsymbol{\Omega}$ particle angular position [rad]. 51, 92

$\boldsymbol{\omega}$ particle angular velocity [$\mathrm{rad\,s^{-1}}$]. 40, 41, 50, 51

$\dot{\boldsymbol{\Omega}}$ particle angular velocity [$\mathrm{rad\,s^{-1}}$]. 91, 92, 102

$\ddot{\boldsymbol{\Omega}}$ particle angular acceleration [$\mathrm{rad\,s^{-2}}$]. 40, 92, 100

$p_\mathbf{f}$ fluid pressure [Pa]. 61, 64, 85, 93, 111–113, 115, 116

$\nabla p_\mathbf{f}$ gradient of fluid pressure [$\mathrm{Pa\,m^{-1}}$]. 116

ϕ porosity [-]. 12, 19, 61, 63, 93, 111, 112, 115, 116

$\bar{r}$ mean particle radius [m]. 38–43, 66, 91, 95, 100–102

ρ grain material density [$\mathrm{kg\,m^{-3}}$]. 8, 38, 43, 66, 95, 115

$\rho_\mathbf{f}$ fluid density [$\mathrm{kg\,m^{-3}}$]. 64, 66, 92, 95, 110–112, 115

$\boldsymbol{\sigma}$ Cauchy stress tensor [Pa]. 7–9, 111

σ_0 defined normal stress [Pa], see also N. 38, 43, 47, 51, 53, 54, 66

σ' effective (measured) normal stress [Pa], see also N. 42, 43

$\boldsymbol{T}$ sum of torques [N m]. 92, 100

t time [s]. 42, 60, 93, 111, 112, 115, 116

τ macroscopic shear stress [Pa]. 9–12, 14, 15, 18, 23, 42, 43, 85

$\boldsymbol{\tau}$ deviatoric stress tensor [Pa]. 7, 111

$\tau_\mathbf{p}$ peak macroscopic shear strength [Pa]. 17, 38, 53, 54

$\tau_\mathbf{u}$ ultimate (critical state) macroscopic shear strength [Pa]. 12, 17, 38, 54

$t_\mathbf{c}$ particle contact duration [s]. 102

Δt computational time step [s]. 40, 41, 43, 66, 101, 103, 104, 111, 112, 115, 116

$t_\mathbf{total}$ total simulation time [s]. 43, 66

u shear velocity [$\mathrm{m\,s^{-1}}$]. 14, 15, 23, 42, 43, 51

$\boldsymbol{v}_\mathbf{f}$ fluid flow velocity [$\mathrm{m\,s^{-1}}$]. 61, 110–112, 115

$V_\mathbf{g}$ grain volume [$\mathrm{m^3}$]. 63, 64, 92

$\boldsymbol{x}$ particle positional vector [m]. 39, 40, 60, 91, 92, 104, 116

$\dot{\boldsymbol{x}}$ particle linear velocity [$\mathrm{m\,s^{-1}}$]. 39, 41, 91, 92, 102–104, 115, 116

$\ddot{\boldsymbol{x}}$ particle linear acceleration [$\mathrm{m\,s^{-1}}$]. 92, 100, 103, 104

$\dddot{\boldsymbol{x}}$ particle linear acceleration [$\mathrm{m\,s^{-1}}$]. 104

$\boldsymbol{x}_{\mathrm{f}}$ fluid cell center position vector [m]. 63, 93

Chapter 1

Introduction

Changes in global ice volume through the Quaternary period have caused eustatic sea level variations of up to 120 m (e.g. Ruddiman, 2007). A total melting of the present global ice volume (33×10^6 km^3 or 69% of Earth's freshwater volume) is equivalent to approximately 70 m sea level rise (e.g. Benn and Evans, 2014). Remote sensing developments have provided global coverage and observations with high certainty, allowing detailed interpretations of the state of the cryosphere, including ice sheet thicknesses and velocities (e.g. Tedesco, 2015). During the last two decades, the Greenland and Antarctic ice sheets glaciers have been losing mass, a trend contributing to the continuous eustatic sea level increase since around 1900 (IPCC, 2013). Projections of climate predict continuous temperature increases in the coming century, fueling interest in understanding ice sheet response and resultant sea level rise (e.g. Alley et al., 2005; Grinsted et al., 2010; IPCC, 2013).

First-order response time of glacier ice to changes in forcing is generally slow due to the high viscosity and heat capacity of ice. Dynamical changes in ice-sheet flow patterns can, however, lead to configurations causing rapid melting of large ice volumes, and the understanding of non-linear thresholds in the glacial systems are consequentially key to understanding the involved sensitivities.

In the palaeo-record ice sheet response has often been non-linear and rapid to changes in climate (e.g. Clark, 1994; Bentley, 1997; Overpeck et al., 2006). This suggests that thresholds caused by dynamical ice flow changes are important mechanisms to ice sheet configuration. The buttressing effect of ice shelves is an example of a non-linear threshold in the glacial system. The disintegration of the Larsen B ice shelf in 2002 caused immediate response in the tributary glaciers. The resistance to flow from the ice shelf was suddenly lost and the tributary glaciers accelerated (Rignot et al., 2004; Scambos et al., 2004; Wuite et al., 2015; De Rydt et al., 2015). Other ice shelves on the Antarctic Peninsula are likely heading towards collapse in the coming decades, as ice shelf thinning is accelerating due to increased oceanic melting (e.g. Paolo et al., 2015).

Ice streams, defined as regions of fast flowing ice (Swithinbank, 1954; Bennett, 2003), are responsible for more than 90% of the Antarctic ice sheet mass flux (Morgan et al., 1983; Rignot et al., 2011). Since seismic surveys (Alley et al., 1986; Blankenship et al., 1986; Anandakrishnan et al., 1998; Anandakrishnan, 2003) and borehole measurements (Engelhardt et al., 1990) revealed that the Antarctic ice streams are moving on deformable and high-porosity sedimentary beds, the me-

chanical implications to ice flow dynamics have been intensely debated. Drilling campaigns have found that ice streams flow as plug flow, and shear deformation primarily takes place in the subglacial till (Engelhardt and Kamb, 1998). Controversial early field studies on a smaller glacier reported that till deforms in a rate-dependent manner with a mildly non-linear viscosity (Boulton and Hindmarsh, 1987), strengthening with increased shearing velocities. Contrasting, laboratory studies have described subglacial till as a mechanically highly non-linear material (e.g. Kamb, 1991; Iverson et al., 1998; Tulaczyk et al., 2000a; Iverson, 2010), a fact that carries the potential to cause large changes in behavior upon moderate forcings. Viscous behavior, on the other hand, dampens variations in flow (e.g. Kamb, 1991; Bennett, 2003; Tulaczyk, 2006).

Projections of ice flow response in a changing climate depend on mathematical ice sheet models that strive to produce best estimates of dynamical ice flow changes. Analytical and numerical continuum mathematical modeling of highly non-linear rheologies such as subglacial till is notoriously difficult (Schoof, 2006; Schoof, 2010a), which has caused studies to often assume only mildly non-linear viscous behavior for till (e.g. Alley et al., 1987b; Hindmarsh, 1998; Huybrechts and Wolde, 1999; Pollard and DeConto, 2009; Joughin et al., 2014), leading projections that may ultimately fall short of describing dynamical changes caused by thresholds in till strength. Recent developments in regularization techniques of till plasticity allow numerical ice flow models to approximate a Mohr-Coulomb parameterization of subglacial till mechanics (Schoof, 2006; Bueler and Brown, 2009; Schoof, 2010a; Bougamont et al., 2011), which proves the point that the right numerical techniques allow for approximation of highly non-linear till mechanics in ice flow models.

In this PhD study subglacial till is approached as a granular material without *a priori* assumptions about macroscopic rheology, with the overarching goal to improve our understanding of its mechanical properties. Granular materials are known for their ability to change phase (e.g. Jaeger and Nagel, 1992; Jaeger et al., 1996; Herrmann, 2002), where each phase is characterized by distinct mechanical properties (e.g. GDR-MiDi, 2004; Krimer et al., 2012). Some of the main questions investigated in this PhD project are:

- Is the discrete element method (DEM) viable for numerical studies of subglacial sediment deformation?
- What is the appropriate constitutive relation for granular materials deforming under subglacial conditions?
- What controls the distribution of subglacial strain with depth, and what are the implications for sediment flux and till continuity?
- What is the appropriate methodology to simulate coupled granular and fluid dynamics in the subglacial bed?
- Do water pressure dynamics caused by subglacial deformation influence till rheology and flux?
- How does variable input of meltwater influence stability of the subglacial bed?

The granular approach and numerical methodology has provided detailed insight in the sediment internals and mechanics in various settings, allowing me to consider the above questions in this thesis. The following chapter will provide background information on the scientific development on understanding and describing till mechanics. The first included manuscript (chapter 4) considers the granular dynamics alone, while the latter two incorporate influence of pore-fluid dynamics (chapters 5 and 6). The above questions will be revisited in chapter 3, "Conclusions and future aspects".

Chapter 2

Subglacial deformation of sediments

Many glacier bases are at the pressure melting point due to the weight of the overlying ice, frictional heating during deformation, and warming by the geothermal heat flux. These processes allow for the presence of liquid water in the subglacial environment. Thawed glacier beds often consist of melt-water saturated granular materials, consisting of either reworked older sedimentary deposits or mobilized products from erosion, collectively termed till (e.g. Clarke, 2005; Evans et al., 2006; Cuffey and Paterson, 2010).

Glacial deformation of till has been described since the late 19th century (McGee, 1894; MacClintock and Dreimanis, 1964), but was not widely recognized as a significant glacier movement mechanism before the late 1970s. Field measurements on an Icelandic glacier bed published in Boulton et al. (1974) and Boulton and Jones (1979) for the first time clearly demonstrated that shearing of glacial till could comprise a significant fraction of the observed surface movement, and deformation was facilitated through high pore-water pressures. The large Pleistocene ice sheets in the Northern Hemisphere flowed on areas of thick deposits of unlithified sediments, spawning a lively discussion about glacier stability, subglacial landform development and sediment transport, which continues to this day (e.g. Boulton, 1986; Piotrowski, 1987; Alley et al., 1987b; Boyce and Eyles, 1991; Clark, 1994; Hallet et al., 1996; Murray, 1997; Fowler, 2000; Piotrowski et al., 2001; Schoof, 2007). The relevance of subglacial deformation to ice flow in the present Antarctic and Greenland ice sheet beds was at the time of G. S. Boulton;s results less than clear, however. Seismic surveys on the Antarctic ice sheet (Whillans Ice Stream (previously named Ice Stream B) (WIS)) a few years later finally revealed that the 1 km thick ice stream flowed on water-saturated subglacial sediment with a 5 m to 6 m thick upper layer of high porosity (Blankenship et al., 1986; Alley et al., 1986). It was argued that the large porosities were indicative of active deformation, and shear movement in these sediments contributed significantly to the overall flow. a few years later finally revealed that the 1 km thick ice stream Palaeo ice-streaming was inferred from mega-scale glacial linear landforms of highly sheared sediments, that were indicative of active sediment advection beneath fast moving ice (e.g. Denton and Hughes, 1981). The role of subglacial sediment deformation processes to the flow of the Greenland ice sheet was uncertain until recently, where radar mapping of the major North-East Greenland Ice

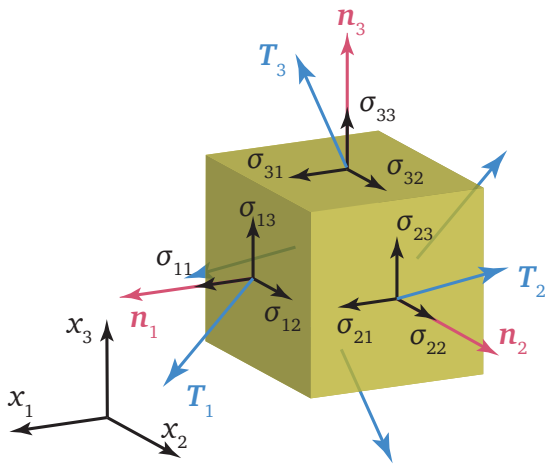

Figure 2.1. Component-wise decomposition of stress vectors ($\boldsymbol{T}$) acting on the surfaces of a rectilinear orthogonal cube yields the Cauchy stress tensor.

Stream revealed that it also flows on deformable sediments (Christianson et al., 2014). Fast ice flow and areas of unlithified subglacial sediment seemed to be closely related (e.g. Anandakrishnan et al., 1998; Tulaczyk et al., 1998).

In this chapter I will briefly describe relevant concepts from continuum mechanics before reviewing previous research into the mechanical behavior of till, mostly adhering to chronological order. Finally I will relate the findings of my study to the previous research. The review is based on the referenced literature and the informative reviews by Murray (1997), Alley et al. (1997), Piotrowski et al. (2001) Clarke (2005), Evans (2005), Kavanaugh and Clarke (2006), Evans et al. (2006), Cuffey and Paterson (2010), Iverson (2010), Iverson and Zoet (2015), and Flowers (2015).

2.1 Fundamentals of continuum modeling

Mathematical modeling of deformation requires description of stress and strain and a constitutive relation linking the two. In mathematical models of glacier flow the stresses driving deformation are most commonly inferred from local or regional ice geometry, and response in ice deformation and geometry is the desired result from the model. In the following, I will present the most important concepts of continuum modeling based on Segall (2010) and Gerya (2010).

Stress

Stress is a vector $\boldsymbol{T}$ relative to a surface. The complete stress-state in a three-dimensional body can be described by the second-order Cauchy stress tensor, which decomposes each stress vector acting on three orthogonal and axis-parallel surfaces

into components of the global coordinate system (Fig. 2.1):

$$\boldsymbol{\sigma} = \begin{bmatrix} \sigma_{11} & \sigma_{12} & \sigma_{13} \\ \sigma_{21} & \sigma_{22} & \sigma_{23} \\ \sigma_{31} & \sigma_{32} & \sigma_{33} \end{bmatrix} \tag{2.1}$$

Rotation occurs if the stress tensor is asymmetric around the diagonal. The diagonal components ($\sigma_{11}, \sigma_{22}, \sigma_{33}$) describe the orthogonal normal stresses, and the mean value of normal stresses defines pressure: $\sigma_{kk}/3 = -p$. The off-diagonal components in the stress tensor and normal stress isotropy denote the deviatoric stress ($\boldsymbol{\tau}$):

$$\boldsymbol{\sigma} = -p\boldsymbol{\delta} + \boldsymbol{\tau} \tag{2.2}$$

where $\boldsymbol{\delta}$ is the Kroneker delta, also referred to as the identity matrix:

$$\boldsymbol{\delta} = \begin{bmatrix} 1 & 0 & 0 \\ 0 & 1 & 0 \\ 0 & 0 & 1 \end{bmatrix} \tag{2.3}$$

The deviatoric stress is also a second order tensor:

$$\boldsymbol{\tau} = \begin{bmatrix} \tau_{11} & \tau_{12} & \tau_{13} \\ \tau_{21} & \tau_{22} & \tau_{23} \\ \tau_{31} & \tau_{32} & \tau_{33} \end{bmatrix} \tag{2.4}$$

Strain

Deformation takes place when two points in a material move relatively to each other. The relative movement can be defined as gradients in velocity, which in a three-dimensional Cartesian frame can be expressed by component-wise partial derivatives in a second rank tensor:

$$\nabla \boldsymbol{v} = \begin{bmatrix} \partial v_1/\partial x_1 & \partial v_1/\partial x_2 & \partial v_1/\partial x_3 \\ \partial v_2/\partial x_1 & \partial v_2/\partial x_2 & \partial v_2/\partial x_3 \\ \partial v_3/\partial x_1 & \partial v_3/\partial x_2 & \partial v_3/\partial x_3 \end{bmatrix} \tag{2.5}$$

If the material is not rotating the displacement gradient vector is symmetric:

$$\frac{\partial v_i}{\partial x_j} = \frac{\partial v_j}{\partial x_i}, \quad \text{where } i \neq j \tag{2.6}$$

At small displacements gradients the components of the displacement gradient tensor can be associated with small strains. The infinitesimal strain tensor describes strain from symmetric velocity gradients:

$$\epsilon_{ij} \equiv \frac{1}{2}\left(\frac{\partial v_i}{\partial x_j} + \frac{\partial v_j}{\partial x_i}\right) \tag{2.7}$$

The full strain tensor $\boldsymbol{\epsilon}$ is:

$$\boldsymbol{\epsilon} = \begin{bmatrix} \epsilon_{11} & \epsilon_{12} & \epsilon_{13} \\ \epsilon_{21} & \epsilon_{22} & \epsilon_{23} \\ \epsilon_{31} & \epsilon_{32} & \epsilon_{33} \end{bmatrix} \tag{2.8}$$

Simple shear, or isochoric plane deformation, takes place when only one velocity gradient component has a non-zero value, and can be expressed as a single shear-strain scalar γ in the strain tensor. For simple shear along the first dimension:

$$\boldsymbol{\epsilon} = \begin{bmatrix} 0 & \gamma & 0 \\ \gamma & 0 & 0 \\ 0 & 0 & 0 \end{bmatrix} \tag{2.9}$$

or, alternatively, as strain rate:

$$\dot{\boldsymbol{\epsilon}} = \begin{bmatrix} 0 & \dot{\gamma} & 0 \\ \dot{\gamma} & 0 & 0 \\ 0 & 0 & 0 \end{bmatrix} \tag{2.10}$$

Simple shear is often assumed during subglacial deformation as glacier movement occurs parallel to the ice-bed interface (IBI) and the IBI and lower boundary of the till are assumed parallel.

Conservation laws

Continuum modeling relies on principles of conservation of material mass, linear and angular momentum and energy, which are fundamental laws of nature in closed systems. The conservation laws are most commonly derived using Leibniz's theorem, and the reader is referred to continuum mechanics literature for complete derivation of the balance laws (e.g. Griebel et al., 1998; Segall, 2010; Gerya, 2010).

Balance of mass

Conservation of mass can in Lagrangian vector form be written as

$$\frac{D\rho}{Dt} + \rho \nabla \cdot \boldsymbol{v} = 0 \tag{2.11}$$

which implies that local changes in density (ρ) are balanced by divergence in the flow field ($\nabla \cdot \boldsymbol{v}$). In many cases the materials are considered to be *incompressible*, which means that their density is constant ($D\rho/Dt = 0$). That assumption reduces the conservation equation to:

$$\nabla \cdot \boldsymbol{v} = 0 \tag{2.12}$$

Balance of linear momentum

In an isolated system the total momentum is conserved, which is useful for relating stress and strain. Cauchy's first law of motion states that the sum of all forces is equal to the total body and surface force. It is a more general form of Newton's second law, and in its Lagrangian form reads:

$$\rho \frac{D\boldsymbol{v}}{Dt} = \rho \boldsymbol{f} + \nabla \cdot \boldsymbol{\sigma} \tag{2.13}$$

where $\boldsymbol{f}$ is a body force. If acceleration can be neglected the velocity change over time is small ($D\boldsymbol{v}/Dt \approx 0$), and the balance equation reduces to *Stokes flow*:

$$0 = \rho \boldsymbol{f} + \nabla \cdot \boldsymbol{\sigma} \tag{2.14}$$

Constitutive relations

Constitutive laws describe the relationship between stress and strain or, in other words, how a material deforms due to internal or external forcings. Forward-in-time modeling is done by inserting known stresses ($\boldsymbol{\sigma}$) and body forces into the momentum equation (Eq. 2.13 or 2.14) and solving the system of equations.

In the following section I will review the research efforts to establish a general constitutive relation for till rheology, and expand on the consequences for ice sheet stability, subglacial sediment transport, and channelized flow of subglacial meltwater.

2.2 Deduction of a rheological model for till

Field observations proved that sediment deformation in many cases is an important constituent of glacier flow (e.g. Boulton et al., 1974; Boulton and Jones, 1979). This realization required rethinking of the approach to mathematical modeling of glaciers, as previous mathematical models had considered glacier flow on stable hard-rock beds only (e.g. Weertman, 1957; Lliboutry, 1968; Kamb, 1970; Iken, 1981; Fowler, 1981), and initiated a continuing discussion about the appropriate constitutive relation applicable to till rheology. The discussion has mostly centered on deducting the relationship between shear stress τ_{12} (hereafter denoted τ) and shear-strain rate $\dot{\gamma}$, which is required for mathematical modeling of sediment deformation.

The simplest proposed rheological law for shear deformation in subglacial beds is the linear (Newtonian) viscous constitutive relation:

$$\dot{\gamma} = \frac{1}{2\nu}\tau \tag{2.15}$$

where ν is the till viscosity. Due to its simplicity and lack of better constrained formulations, this model was popular in early mathematical models including till deformation. The law is also similar to the widely used sliding law proposed by Weertman (1957); $u = C\tau^n$. Viscosity values for Eq. 2.15 constrained from measurements in boreholes span a variety of values (Murray, 1997), from 10^9 Pa s in the subglacial till of Trapridge Glacier, Yukon Territory, Canada, (Fischer and Clarke, 1994) to 10^{12} Pa s in the frozen bed of Bakaninbreen, Svalbard (Porter and Murray, 2001). Laboratory triaxial tests on Lake Michigan Lobe till, Laurentide Ice Sheet, yielded a viscosity on the order of 10^9 Pa s to 10^{11} Pa s (Jenson et al., 1996), but the methodology surrounding these results is not clear.

Boulton and Hindmarsh (1987) argued that their measurements of shear stress (τ) and strain rate ($\dot{\gamma}$) data from the subglacial bed of Breidamerkurjökull, Iceland, were more adequately explained by either a non-linear viscous flow law or a Bingham viscoplastic model. The proposed non-linear flow law was identical to the empirical soft-bed sliding law proposed by Budd et al. (1979) and of the form:

$$\dot{\gamma} = a\frac{\tau^n}{N^m} \tag{2.16}$$

The parameter a was termed the *softness parameter* or *rate factor* and scales to the inverse value of shear viscosity. The viscosity can in the above formulation be interpreted as being dependent on effective normal stress (N). The best fit was achieved with $a = 3.99$, $n = 1.33$ and $m = 1.8$ with a correlation coefficient value

of 0.987. Stress exponent values of $n = 1$ and $m = 0$ correspond to a Newtonian (linear) fluid. The effective pressure dependence on viscosity in the constitutive relation causes increased strain rates due to till deformation during high pore-water pressure events, consistent with observations of fundamental proportionality between glacier surface melting rates and flow flow velocities (e.g. Willis, 1995; Zwally et al., 2002).

Boulton and Hindmarsh (1987) alternatively proposed a non-linear Bingham fluid model:

$$\dot{\gamma} = a \frac{[\tau - \tau_c]_+^n}{N^m} \tag{2.17}$$

The $[\tau - \tau_c]_+$ notation means that negative values of $\tau - \tau_c$ yield zero. The yield strength (τ_c) is determined by the Mohr-Coulomb criterion (Terzaghi, 1943):

$$\tau_c = C + \mu N \tag{2.18}$$

C is the material cohesion and μ is the internal friction coefficient[1]. The values fitted by Boulton and Hindmarsh (1987) of $a = 7.62$, $n = 0.625$, $m = 1.25$, $\mu = 0.625$ and $C = 3.75$ kPa resulted in a slightly lower correlation coefficient of 0.986.

Equations 2.16 and 2.17 can be rearranged and generalized to highlight the assumed rate-dependence on till strength, with a yield strength term for the Bingham model:

$$\tau = \left(\frac{\dot{\gamma} N^m}{a} \right)^{1/n} + \underbrace{C + \mu N}_{\text{Yield strength}} \tag{2.19}$$

Both rheological models are with the fitted values only mildly non-linear, and produce results similar to the linear model (Eq. 2.15) at strain rates larger than $\sim$7 a^{-1} (Fig. 2.2).

The methodology surrounding the stress measurements by Boulton and Hindmarsh (1987) was not accounted for in the paper, and concerns were raised about the stress field in the ice-marginal area of sampling (e.g. Hooke et al., 1997). Subsequent studies of till rheology, presented in the following, indicated that it was more appropriate to use a highly non-linear constitutive relation, and the validity of the results from Boulton and Hindmarsh (1987) are today highly questioned. Clarke (1987) proposed a slightly different Bingham-type flow law from theoretical considerations, with $n = 1$, $m = 0$, and a different parameterization of effective pressure N.

A few years later Kamb (1991) presented laboratory studies on a till sample recovered through a borehole from beneath WIS at the *Upstream B* (UpB) site. The till sample was fine grained and weak, with a shear strength of only a few kPa in the state it was recovered (Kamb, 1991; Kamb, 2001). B. Kamb performed both stress and rate-controlled direct shear tests, and concluded that the till sample deformed as a highly non-linear Mohr-Coulomb material (Eq. 2.18), a result directly contrasting the previous interpretation by Boulton and Hindmarsh (1987). In the stress-controlled experiments B. Kamb noted a small but declining shear displacement when the sample was stressed with less than the plastic yield strength. As shear stress exceeded the shear strength, movement accelerated as the material was unable to sustain stress balance. The general relationship between stress

[1]The angle of internal friction (ϕ) relates to the internal friction by $\mu = \tan\phi$

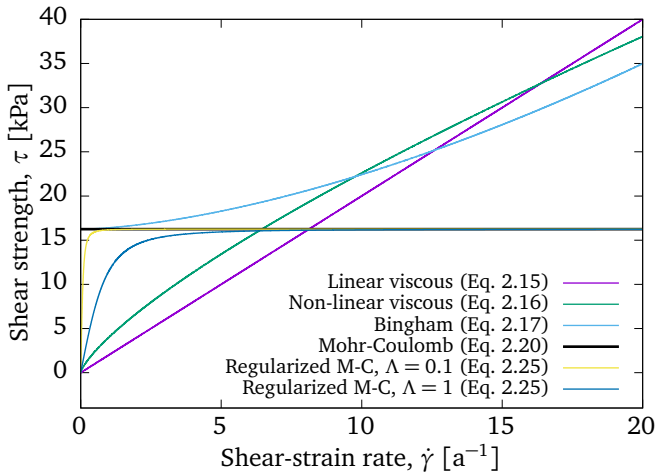

Figure 2.2. Stress-strain behavior of various proposed rheological models for till. The non-linear viscous law, the Bingham flow law, and the Mohr-Coulomb strength were plotted using fitted values by Boulton and Hindmarsh (1987) and a effective normal stress of $N = 20$ kPa.

and strain rates in perfect plastic materials is 0 beneath the yield stress and unconstrained by the material above it, as friction provided by the Mohr-Coulomb material is insufficient to obtain stress balance:

$$\dot{\gamma} = \begin{cases} 0, & \text{if } \tau < C + \mu N \\ > 0, & \text{otherwise} \end{cases} \tag{2.20}$$

B. Kamb noted that the non-linearity in strength had possible implications for ice stream dynamics, and that the low strength likely caused flow-limiting friction for Whillans Ice Stream to be supplied elsewhere.

The diversity of field data on till behavior was expanded by campaigns on smaller mountain glaciers, accompanied with significant advances in instrumentation (Blake et al., 1992). Blake et al. (1994) presented first results of subglacial deformation beneath Trapridge Glacier, Canada, and noted that subglacial movement in and over the till bed contributed more than half the observed surface velocity. Glacier velocities varied diurnally, a finding that linked observations on surface melt with subglacial movement through variations in basal water pressure. Melt-water modulated the mechanical coupling between ice and bed. Observed stick-slip behavior could be accounted for by frictional sliding between idealized elastic blocks of ice and sediment (Fischer and Clarke, 1997), demonstrating the importance of till elasticity on shorter time scales.

Iverson et al. (1995) and Hooke et al. (1997) investigated basal mechanics with tiltmeters, pressure transducers, and various till strength instruments, emplaced through boreholes in the basal till beneath Storglaciären, Sweden. Hooke et al. (1997) demonstrated that *in-situ* till behavior adhered to the plastic Mohr-Coulomb constitutive relation (Eq. 2.18), and noted a very slight increase in strength

with increasing rates:

$$\dot{\gamma} = \begin{cases} 0, & \text{if } \tau < C + \mu N \\ \beta \dot{\gamma}_0 \mathrm{e}^{k\frac{\tau}{\tau_0}}, & \text{otherwise} \end{cases} \tag{2.21}$$

where $\beta = \mathrm{e}^k$, and $\dot{\gamma}_0$ and τ_0 are reference shear-strain rate and shear stress values, respectively. Both publications noted that the effect of water pressure modulations is two fold; till strength decreases with increasing water pressure as effective stress decreases. Secondly, the mechanical coupling between glacier and its bed varies with effective pressure. Decreases in contact area during increasing basal water pressures cause glacier acceleration, and the proportion of frictional resistance provided elsewhere than the bed increases.

In general, *in-situ* observations on subglacial processes through boreholes allow detailed studies of strain and the influence of pore-water pressure dynamics, but offer little knowledge and control over e.g. the driving stress τ. The direct shear measurements used in the laboratory by Kamb (1991) was limited to relatively low values of shear strain (γ). The direct shear apparatus works by breaking a cylindrical sample perpendicularly to its length axis, causing boundary friction to increase and sample contact area to decrease with increasing shear strain (e.g. Bowles, 1992).

Annular ring-shear experiments are not bound by these constraints in control over stress and shear strain, and the ring-shear studies by N. R. Iverson and S. Tulaczyk have provided both comprehensive and detailed insight into till mechanics. Iverson et al. (1997a) and Iverson et al. (1998) demonstrated that till strength, both for coarse and clay rich specimens, is mostly independent on deformation rate, unlike the rate dependence in the viscous models (Eq. 2.19), and instead determined by effective normal stress, as previously concluded by Kamb (1991) and Hooke et al. (1997). The coarse till had a slightly higher angle of internal friction, and the clay-rich till had a slightly larger amount of cohesion (Iverson et al., 1998).

Tulaczyk et al. (2000a) revisited the till samples from the UpB site previously described by Kamb (1991) with laboratory tests of uniaxial compression, triaxial deformation and rotational ring-shear tests. The latter methodology proved that the till from the UpB site, once in the critical failure state, had a constant ultimate shear strength τ_u regardless of shear strain. Results from the triaxial tests concluded that the till shear strength, like the previous till samples (Kamb, 1991; Iverson et al., 1997a), was adequately described by the Mohr-Coulomb constitutive relation (Eq. 2.18) and that strength was practically independent of shear strain and shear-strain rate. Assuming that subglacial till remained in the critical state, S. Tulaczyk realized that effective pressure N and shear strength τ was directly proportional to the till porosity (ϕ). This allowed him to formulate a relationship which expresses shear strength as a function of the void ratio $e = 1 - \phi$, which he called the *undrained plastic-bed model* (Tulaczyk et al., 2000b):

$$\tau = a \exp(-be) \tag{2.22}$$

where a and b are two positive empirical constants. The evolution of porosity can be coupled with local or regional models of subglacial hydrology (e.g. Bougamont et al., 2011; Wel et al., 2013), and/or water supply and removal by thaw-freeze processes (Christoffersen and Tulaczyk, 2003a; Christoffersen and Tulaczyk, 2003b; Bougamont et al., 2011).

The nearly plastic rheological description of subglacial till had by the late 1990s gained wide empirical support, but was not yet widely accepted. This was perhaps caused by the deadlock a rate-independent description introduced for the traditional approach by mathematical modelers. The proposed relationships based on Mohr-Coulomb plasticity did not offer a straight-forward relation to subglacial sliding velocities.

It was argued that the proposed plastic till rheology was inappropriate for describing subglacial mechanics beneath ice streams, as the limited strength a Mohr-Coulomb bed can provide was inconsistent with the stability of the West Antarctic ice streams (Hindmarsh, 1998). Tulaczyk et al. (2001) argued that the flow-limiting friction in these cases was provided by side boundaries, e.g. ice-stream margins, and highlighted how ice shelves with zero basal friction were a clear-cut example of such a balance between driving stress and lateral friction.

Further concerns were raised by Hindmarsh (1997) and Fowler (2003), who argued that the plastic rheology observed in small spatial-scale laboratory devices and field studies not correctly described larger-scale behavior of subglacial beds. Their idea was that the integrated response of many small-scale plastic failures may produce large-scale viscous behavior. Tulaczyk (2006) countered the argument of scale dependence on rheology by demonstrating that the stick-slip behavior of the $\sim$10 000 km^2 ice plain at the mouth of Whillans Ice Stream (e.g. Bindschadler et al., 2003) conformed to the predicted behavior of a nearly plastic bed, forced by a driving stress fluctuating around the Mohr-Coulomb plastic yield strength.

More field data collected under Trapridge Glacier was given a rigorous analysis by Kavanaugh and Clarke (2006), who compared the theoretical mechanical response of several proposed rheological models against their field measurements. The analysis included diffusion of pore-water pressure, which influences deformation in all rheologies dependent on effective pressure. They found the best correlation between modeled response and field measurements with the Coulomb-plastic model.

Borehole campaigns mostly yield point measurements and no control over till composition. Larger-scale *in-situ* experiments were performed the Svartisen Subglacial Laboratory, which through a system of tunnels gives direct access to the subglacial bed beneath Engabreen, an outlet glacier of Svartisen, Norway. Iverson et al. (2007) placed an heavily instrumented synthetic till prism beneath the ice, and controlled pore-water pressure with a pump. The ice entrained the uppermost sediment by regelation infiltration. Till shear strength behaved according to the Mohr-Coulomb criterion (Eq. 2.18), and movement happened through slip at the pressure-melting point isothermal for low water pressures, where till strength exceeded subglacial shear stress. Pervasive deformation of the till took place at high water pressures which weakened the till.

Recent technological developments have allowed for year-long *in situ* observations by wireless probes placed in the subglacial bed (Hart et al., 2006; Martinez et al., 2009). The probes include a variety of sensors, including recording of stresses on the 13 cm long pill-shaped enclosure, water pressure, tilt and electrical resistance. Hart et al. (2009) and Hart et al. (2011) employed these probes under the Norwegian Brikdalsbreen through boreholes. They flushed away some of the basal till, inserted the probes into this space, and let the till close around them. From the measured data they argued that the till rheology was time-variable, altering between elastic and viscous deformation governed by pore-water pressure. The high-water pressure periods were associated with rate-dependent strength and

continuous rotation (Jeffery, 1922). Hart et al. (2011) reported a best fit between case-stress data and tilt rates by a Bingham viscoplastic flow law with a stress exponent value of 1, i.e. a linear viscosity above the yield strength. They did not find a consistent relationship between effective pressure and shear strain, which they somewhat puzzling argue is crucial for a plastic till rheology. The study implicitly assumes that driving glacier stresses are supported only by basal strength, as local stresses are thought to directly influence local strain rates. Previous studies argue that the resistance provided by soft glacier beds in many cases is too weak to support the driving stresses (e.g. Kamb, 1991; Iverson et al., 1995; Hooke et al., 1997; Joughin et al., 2009). The reported linear relationship between strain rate and effective stress may not represent local conditions, but instead result from flow variations of the glacier as a whole in response to annual and daily variations in surface melt.

Basal movement on a Mohr-Coulomb plastic bed

Progress in the mathematical description of hard limits in subglacial strength was made by Schoof (2005), who proposed a hard-bed sliding law including cavitation:

$$f = \left(\frac{u}{u+\Lambda}\right)^{p-1} \tag{2.23}$$

u is the basal sliding rate, f is a dimensionless coefficient of friction and a dimensionless parameter Λ scales with bed roughness. Frictional resistance is limited with increasing sliding velocities, as cavities grow and the contact surface area between ice and bed is reduced, a limit known as *Iken's bound* (Fowler, 1986; Fowler, 1987; Schoof, 2005; Zoet and Iverson, 2015). The degree of non-linearity is determined by the value $p > 1$. Schoof (2010a) demonstrated that a law of the same type as the hard-bed sliding law with cavitation is suitable for mathematically describing Coulomb frictional sliding, assuming that the entire basal domain is not exceeding the yield stress. The regularized form of the Coulomb friction sliding law more closely than previous efforts approximates the rate-independence of Mohr-Coulomb plasticity, while retaining the one-to-one correlation between rate and stress. The regularized friction function is due to its continuousness simpler to handle by analytical and numerical methods:

$$f = \frac{u}{\sqrt{u^2+\Lambda^2}} \tag{2.24}$$

The expression can be used to scale the yield strength predicted by the Mohr-Coulomb equation (Eq. 2.18):

$$\tau = (C + \mu N)\frac{u}{\sqrt{u^2+\Lambda^2}} \tag{2.25}$$

The equation intersects the $(u, \tau) = (0, 0)$ point, but rapidly grows to asymptotically approach the Mohr-Coulomb plastic limit (Fig. 2.2). The value of the dimensionless parameter Λ describes the growth rate or non-linearity at low strain rates (Fig. 2.2).

Constraining basal rheology from ice flow inversion

Detailed GPS records revealed that several Antarctic marine-terminating ice streams flow with surface velocities influenced by the tidal stage (e.g. Bindschadler et al.,

2003; Gudmundsson, 2006; King et al., 2011). The observed correlation between tidal forcing and flow response is non-linear, with the stick-slip behavior on the downstream ice plain of WIS as the most notable example. Velocities here vary three orders of magnitude during a tidal cycle (Bindschadler et al., 2003; Tulaczyk, 2006). Bindschadler Ice Stream, also a tributary to the Ross Ice Shelf, West Antarctica, shows velocity variations by a factor of three (Anandakrishnan et al., 2003). The surface velocity of the more narrow Rutford Ice Stream, West Antarctica, which flows into the Filchner-Ronne Ice Shelf varies by 10 to 20% (Gudmundsson, 2006). Several studies noted that investigations into the flow dynamics may yield information about the subglacial sediment rheology on a large spatial scale.

It is commonly assumed that tidal flexure of the ice shelf-ice stream system cause variations in the ice stream basal stress (e.g. Bindschadler et al., 2003; Gudmundsson, 2007; King et al., 2011), typically reducing to the form:

$$\tau = \bar{\tau} + K\rho_{\mathrm{w}} g h(t) \tag{2.26}$$

where $\bar{\tau}$ is the mean basal shear stress, K is a scaling factor, ρ_{w} is ocean water density, and $h(t)$ is the tidal elevation at time t. The inferred evolution of stresses was coupled to a sliding formulation similar to the hard-bed sliding law proposed by Weertman (1957) or a pressure-independent variant of the non-linear sliding law proposed by Boulton and Hindmarsh (1987) (Eq. 2.16):

$$u = c\tau^n \tag{2.27}$$

u is basal sliding velocity, which for the Antarctic ice streams moving by plug flow corresponds to their surface velocity. A stress exponent (n) of 1 denotes linear (Newtonian) viscosity, while $n = \infty$ corresponds to perfect plastic behavior.

Studies of stress balance showed that the driving stresses on Whillans ice plain, downstream of Whillans Ice Stream, were balanced by local basal friction (Joughin et al., 2004). Tulaczyk (2006) showed that the stick-slip behavior of WIS follows a highly non-linear rheology with a stress exponent value between 9.4 and 13.3.

Gudmundsson (2007) presented a conceptual model for Rutford Ice Stream. Inferred changes in driving stress, coupled with a sliding law of the above type with $n = 3$, produced strikingly similar displacements relative to GPS data. King et al. (2010) confirmed the stress exponent value of 3 at the same ice stream in an expanded analytical modeling analysis. King et al. (2011) performed the same analysis for GPS data collected near the grounding line on Larsen C ice shelf on the Antarctic peninsula, and found a best fit with a stress exponent value of 2.94. The models did not include the viscoelastic effects of the ice stream itself, however. This shortcoming was handled by Gudmundsson (2011), who developed a numerical flow-band (2d) model for the system. He reported less certainty in determining a specific stress exponent value than in previous studies, but noted that moderately large values in the range of 2 to 10 replicated the main qualitative features of the displacement record at Rutford Ice Stream.

The attention was turned to Bindschadler Ice Stream by Walker et al. (2012) who, akin to the work by Gudmundsson (2011), employed a numerical viscoelastic flowline model for investigating the basal sliding properties. Depending on the elastic modulus in the ice, they obtained best fits between surface displacement data and model behavior with stress exponent values between 10 and 15, more closely resembling the large-scale near-plastic behavior for WIS (Tulaczyk,

2006). Rosier et al. (2014) used a three-dimensional full-Stokes[2] viscoelastic ice flow model in a geometry similar to Rutford Ice Stream, and showed that inclusion of horizontal limits such as ice stream shear margins and the grounding line did not alter previous estimates of the stress exponent value of 3. Goldberg et al. (2014) used a two-dimensional plan-view viscoelastic numerical model with a regularized Mohr-Coulomb formulation for basal friction (Eq. 2.25), shear margins, and a grounding line. When investigating stick-slip behavior on Whillans Ice Plain they confirmed that the large-magnitude variation was caused by highly non-linear basal strength.

In both Thompson et al. (2014) and Rosier et al. (2015) three-dimensional viscoelastic ice flow models are employed to study transmission of tidal perturbations inland through the ice. Thompson et al. (2014) were unable to reproduce the observed flow dynamics of Rutford Ice Stream reported by Gudmundsson (2011) by ice flexure alone. Tidal perturbations of the stress field in the ice undergoes rapid damping up-ice, causing tidal variations in stress unlikely to be sufficient to significantly alter ice flow velocities. Instead they hypothesized that the tidal variation in water pressure at the grounding line is diffusing up under the ice through water flow at the ice-bed interface (IBI). This hypothesis requires large hydraulic conductivity usually associated with channelized subglacial water flow. Tidal variations in pore-water pressure alter the effective stress instead of shear stresses (Eq. 2.26), and previous studies had used a sliding law independent of normal stress (Gudmundsson, 2007; Gudmundsson, 2011; Rosier et al., 2014). Rosier et al. (2015) employed a pressure-dependent non-linear viscous sliding law like proposed by Boulton and Hindmarsh (1987) (Eq. 2.16), and included a subglacial model of hydraulic diffusion. They reported a best fit against Rutford Ice Stream data with a stress exponent value of 3.

The applicability of GPS measurements to deduct basal rheology is an ongoing discussion. I note that systems responding to perturbations in stress to a relatively low power of 3 may to a greater extent contain ice-deformational resistance to flow in their stress balance, as a stress-exponent value of around 3 is often measured for the rheology of polycrystalline ice (e.g. Glen, 1955; Hooke, 1981). Precursive inversion of the system stress balance must be performed to assess whether ice flow dynamics in a given location primarily reveal insight into rheology of basal, marginal or external process. Further investigation into subglacial hydrology in these environments is required, since flow oscillations seem to be strongly connected to hydrological changes (Thompson et al., 2014; Rosier et al., 2015).

Insight into granular rheology from computational experiments

The discrete element method (DEM) methodology adopted in my studies has several simplifications with regards to describing grain shape, grain size, grain-size distribution, and spatial scale, mainly caused by severe computational expenses. The method is, however, widely applied and considered the *de facto* standard for simulating granular materials (e.g. Hinrichsen and Wolf, 2004; Radjaï and Dubois, 2011). Granular material-specific processes, such as phase transitions and shear induced dilation and weakening are lacking adequate continuum-formulations (e.g. Gennes, 1999). The granular model developed for our studies has allowed us to

[2]Referring to a flow solution including the full nine-component Cauchy stress tensor (Eq. 2.1) in the momentum equation for steady state flow (Eq. 2.14).

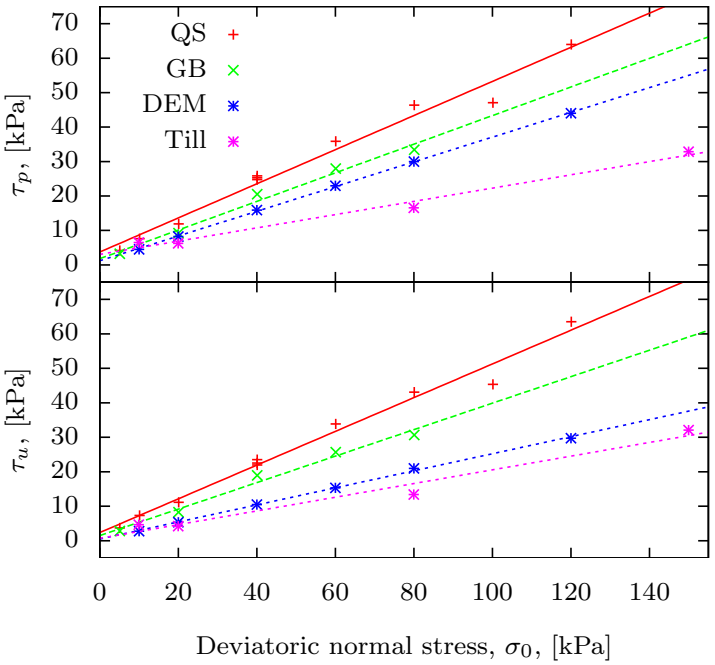

Figure 2.3. Mohr-Coulomb failure analysis of three laboratory granular materials (quartz sand, glass beads, and a till) and one numerical material (DEM). The Mohr-Coulomb constitutive relation (Eq. 2.18) was fitted to peak (τ_p) and critical state (τ_u) strengths. Figure also on p. 54.

test granular response to various forcings and draw parallels to subglacial processes.

In paper 1 of this thesis (Ch. 4 and Damsgaard et al. (2013)) we demonstrate that two simple granular materials, a numerically simulated granular material, and a till all yield according to the Mohr-Coulomb criterion (Fig. 4.14) and independent of deformation rate at glacial velocities. When the material is in a consolidated pre-failure state, the deformational strength evolves with early shear strain. Early deformation is associated with a mostly linear increase to a peak shear strength. Subsequent strain in the critical state is characterized by a somewhat lower strength when the shear zone is fully developed and weakened due to increased porosity (Fig. 4.4, p. 44). It is unclear at present if the sediment beneath variable moving ice consolidates to the pre-failure state during slow flow events (Iverson, 2010), but stagnant periods may cause the bed to significantly harden. Subsequent deformation events will have to overcome the peak strength before the bed weakens to the critical state value.

We investigated the influence of pore water on granular rheology in paper 2 (Ch. 5). We showed that in a few select cases, the viscosity of water contributes to the yield strength from the granular phase as an additional strengthening process caused by dilation. The dilatant hardening is dependent on shear rate and diminishes after the sediment ends its volumetric expansion in the critical state.

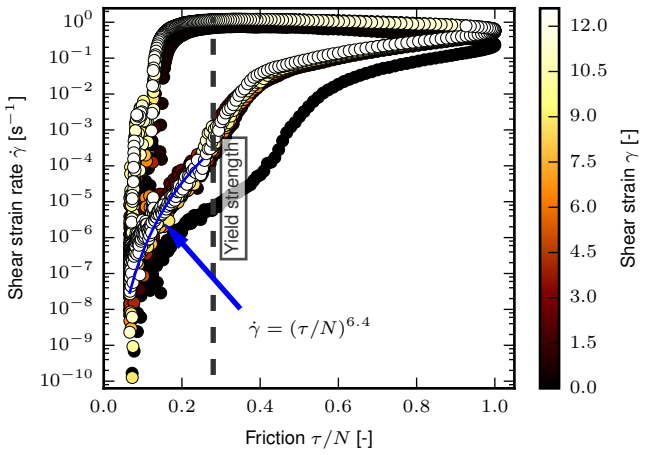

Figure 2.4. Non-linear viscous behavior during pre-failure creep in numerical deformation experiments. Figure also on p. 89.

The behavior is consistent with the theoretical considerations by Iverson (2010), and demonstrates that the hardening is caused by micromechanical processes of contact strengthening due to gradients in pore-water pressure.

In paper 3 (Ch. 6) we demonstrate that granular materials can display slow creep beneath the Mohr-Coulomb yield strength due to changes in internal stresses, which previously was not considered in Mohr-Coulomb models (Eq. 2.20 and 2.21). We demonstrate how changes in effective stress caused by variations in pore-water pressure cause reorientation in the orientation of maximum compressive stress. The stress-supporting contact network in the sediment consists of a finite number of grain contacts with variable orientation. If the normal or shear stress changes, a fraction of the contacts will fail and grain pairs slide on their mutual contact interface. These failures will increase loading on the remaining contacts and cause slight deformation until a new stable packing is obtained. The displacement is larger for low effective stresses as the lower packing density allows for larger grain displacements (Fig. 2.4). The rate dependence on stress disappears when the sediment is forced above the Mohr-Coulomb yield stress. The relationship between strain rate and stress during creep can be fitted with a non-linear viscous relationship of the form:

$$\dot{\gamma} = \left(\frac{\tau}{N}\right)^{n} \tag{2.28}$$

where the stress exponent n in the numerical experiments depends on consolidation state and pore-water perturbation amplitude. In our experiments we fit exponent values ranging from 6 to 11, which depicts significantly more non-linear behavior than the stress exponent values fitted by Boulton and Hindmarsh (1987). The viscoplastic Bingham model (Eq. 2.17) depicts zero deformation beneath the plastic yield strength, and rate-dependent non-linear strengthening above the plastic strength.

The proposed flow for creep, combined with the rate-dependence above the yield stress, law most closely resembles the regularized Mohr-Coulomb law by

Schoof (2010a). Velocities are small beneath the yield stress and stresses are limited by the Mohr-Coulomb stress at larger driving stresses.

The constitutive relation for creep presented above fits the results from our computational experiments, but I note that further research on various materials is required for corroborating the creep behavior in sediments forced with variable pore-fluid pressure. Slow creep is known from landslides and hillslopes, which can display downslope movement under the angle of repose due to transient stress perturbations (Terzaghi, 1951; Carson and Kirkby, 1972; Iverson, 1986; Iverson and Major, 1987; Roering et al., 2001; Malet et al., 2002; Schulz et al., 2009; Handwerger et al., 2015). The results produced here may be applicable to a wider range of geological processes, pending further investigation.

2.3 Distribution of strain in the subglacial bed

The type of constitutive relation for the subglacial sediment directly influences the distribution of strain in the subglacial bed, which in turn determines the transport of till (Fig. 2.5). The transient evolution of till bed thickness by advection can be expressed through the Exner equation for sediment mass balance (Exner, 1925; Kyrke-Smith and Fowler, 2014), derived from the advection equation. I expanded the relation with a term $\dot{S}$ denoting the rate of local sediment deposition or erosion by glacier base melt-out or freeze-on:

$$\frac{\partial H}{\partial t} = \frac{1}{1-\phi}\left(\nabla \cdot \boldsymbol{q} + \dot{S}\right) \tag{2.29}$$

H is the bed surface elevation, ϕ is the porosity and $\boldsymbol{q}$ is the flux of till. The implications of subglacial deformation depth upon sediment mass balance was intensely discussed as proposed transport rates seemed to exceed realistic sediment production rates (e.g Cuffey and Alley, 1996; Alley et al., 1997; Alley, 2000).

A material behaving as a linear viscous fluid deforms at low Reynolds numbers as a laminar flow with constant strain rate through its entire thickness (e.g. Alley et al., 1987a). In the Bingham flow model (Eq. 2.17) deformation occurs at all depths where shear stress exceeds shear strength. The shape of the curve above this limit is determined by the stress exponent (e.g. Alley, 1989b). Deformation in idealized perfect plastic materials focuses in a single plane following the weakest strength (Alley, 1989b).

The 5 to 6 m thick porous zones observed with seismic and *in-situ* borehole measurements were interpreted as indicative of deep active deformation (Blankenship et al., 1986; Alley et al., 1986; Engelhardt et al., 1990), and, in turn, supporting a viscous notation of till rheology (e.g. Alley et al., 1989b; Boulton et al., 2001). Later *in-situ* measurements at the UpB site on WIS by Engelhardt and Kamb (1998) disputed this interpretation, as deformation between the IBI and the upper 3 cm accounted for 83% of the total displacement. This observation was seemingly in better agreement with laboratory and most field data of a plastic till rheology.

Modeling work by Beget (1986) and Beget (1987) demonstrated that till rheology likely influenced Pleistocene glacier profiles and flow. Low till strength resulted in low surface slopes as seen on contemporary West Antarctic ice streams.

Assuming a linear-viscous rheology, Alley et al. (1989a) estimated that the subglacial transport rate beneath WIS is 10^2 to $10^3\,\mathrm{m^3\,a^{-1}}$ per meter width at the grounding line, equivalent to an erosion rate of $0.4\,\mathrm{mm\,a^{-1}}$ over the entire

drainage basin (Murray, 1997). This value lies within the inferred erosion rates in the Northern Hemisphere during the Pleistocene glaciations but unlikely for the long-glaciated Antarctic continent (Hallet et al., 1996). MacAyeal (1992) assumed a linear-viscous till rheology for subglacial till in a numerical model for West Antarctic ice sheet flow, and argued that build-up of weak subglacial till layers can destabilize the ice sheet. Alley (1991) discussed that advection in the subglacial bed may explain the widespread till sheets at the southern margin of the Laurentide ice sheet. Jenson et al. (1995) computed till fluxes in a linear-viscous bed from various estimates of till viscosity and found that large viscosity values caused deep deformation. The resultant subglacial sediment transport rates ranged from $10\,m^3\,a^{-1}$ to $100\,m^3\,a^{-1}$ of glacier width. The largest flux estimate was given for the Norwegian Channel ice stream by Nygård et al. (2007), who inferred a transport rate of $8000\,m^3\,a^{-1}$ during a short period of streaming during the last glacial stage.

The plastic model did not seem to agree with most subglacial measurements of deep deformation. Iverson et al. (1998) realized that the granularity of till constituents cause the minimum thickness of deformation to focus in a shear zone, with a width dictated by grain size (Iverson et al., 1998). This distribution of strain in granular materials implies that the deformational depth under a glacier, with water pressure below flotation, never is a single plane (Alley, 1989b). Dilatant hardening processes during deformation of consolidated sediments additionally has the potential to affect strain distribution in granular materials (Iverson et al., 1998). Ploughing of large clasts through the subglacial bed additionally contributes to the distribution of strain to greater depths (Brown et al., 1987; Iverson et al., 1994; Iverson et al., 1999; Tulaczyk et al., 2001; Thomason and Iverson, 2008). Finally, variations in pore-water pressure at the IBI are able to cause significant deviations from hydrostatic pressure in low-permeability tills, which are exponentially damped with depth. Remnant signals of high-pressure periods can cause the weakest point of failure to reside far below the IBI, causing the material on top to be transported passively with minor to no deformation (Tulaczyk et al., 2000a; Truffer et al., 2000).

Truffer et al. (2000) presented tiltmeter results from Black Rapids Glacier, Alaska, USA, and found that more than half the surface velocity originated from subglacial sediment deformation, surprisingly not at the IBI or the upper parts of the till, but at least two meters below the ice-bed interface. Under hydrostatic pressure distribution in the pore water, the effective pressure and, in turn, sediment strength is lowest at the top (Eq. 2.18). Truffer et al. (2000) suggested that annual variations in pore-water pressure at the IBI slowly diffused into the subglacial bed, causing a minimum in strength at several meters depth.

Several clues in the sedimentary record seemed to argue against the existence of deep and widespread deforming beds under the Pleistocene ice sheets, however. Piotrowski and Tulaczyk (1999) interpreted Weichselian ice movement near Kiel, North Germany, to take place mainly by sliding at the IBI. Pervasive deformation of the subglacial bed would homogenize the till due to shear-induced granular diffusion (Weertman, 1968; Hooyer and Iverson, 2000b). The presence of undeformed sedimentary structures was indicative of low to no shear strain in the bed. Thin stringers of well-sorted sediments were interpreted as melt-water deposited during high-water pressure events at the decoupled ice-bed interface. Piotrowski et al. (2001) provided further arguments against pervasive and viscous deformation from sedimentological studies on subglacial tills. They elaborated that the pres-

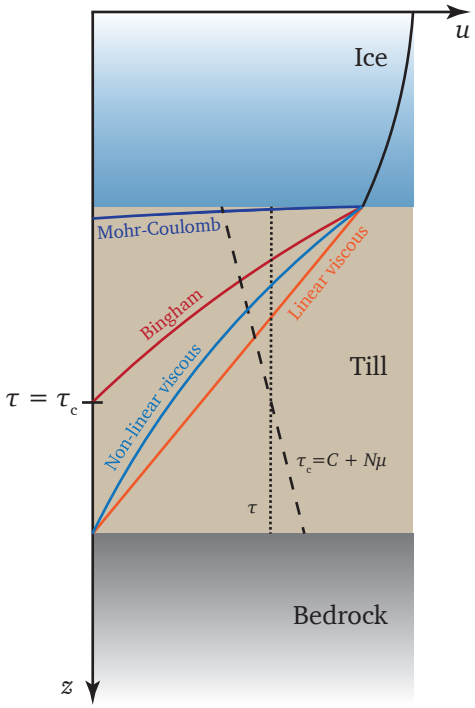

Figure 2.5. Distribution of strain in the subglacial till for different rheological models. The till is homogeneous with a hydrostatic pressure distribution, causing the effective pressure and strength to increase linearly with depth. The linear and non-linear viscous rheologies have no yield strength and deform at all depths. The linear rheological model deforms with constant rate at all depths. The Bingham model causes deformation at all depths where stress exceeds strength ($\tau > \tau_c$). The strain distribution in a Mohr-Coulomb material is determined by material granularity, ploughing from large clasts or ice keels, strain-hardening processes and water-pressure deviations from hydrostatic pressure distribution.

ence of any sharp sedimentary contact, e.g. lower contacts of tills, sedimentary structures in preserved outwash deposits, thin sand stringers in tills, and preservation of pre-glaciation landscapes were incompatible with pervasive and deep deformation. In addition, relatively well preserved fragile components such as heavily weathered boulders or shell fragments embedded in the tills were unlikely to survive large shear strains. Instead, Piotrowski et al. (2001) argued that ice flow at several locations primarily took place by sliding at the IBI, and that the majority of sediment was transported englacially.

Strain distribution in granular modeling

Laboratory shear tests often show thin zones of deformation caused by frictional strengthening from the sample chamber walls (Iverson et al., 1998; Tulaczyk et

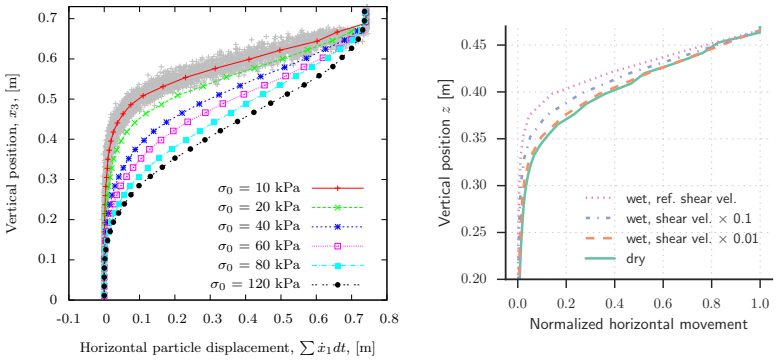

Figure 2.6. Displacement-depth profiles from the numerical experiments. (Left) Strain distribution for dry granular shear at various normal stresses, also on p. 47. (Right) Strain distribution for wet granular shear at different shear velocities, also on p. 72.

al., 2000a; Iverson and Iverson, 2001), in the same way as shear margins of ice streams influence flow rates (Nye, 1952; Raymond, 1996; Joughin et al., 2004). We avoided this artificial frictional strengthening by using *periodic* lateral boundaries. If a simulated grain moves out of one of the sides, it reappears on the opposite side of the model. Grain pairs can also be in mechanical contact although placed at opposite boundaries.

In paper 1 included in this thesis (Damsgaard et al. (2013), Ch. 4) we show that the shear zone thickness in cohesion-less granular material has a certain minimum width, controlled by grain size, and a concave down shape (Fig. 2.6, left). Sharp velocity discontinuities require interaction over at least 5–10 grain sizes. The shear zone becomes wider with increasing effective pressure as internal force chains strengthen. Compacted granular materials require volumetric expansion to deform, as grains need to move past each other (Reynolds, 1885; Mead, 1925). The dilation in shear zones weakens the sediment as the average number of intergrain contacts is reduced, increasing the likelihood that contacts are unfavorably oriented relative to the stress.

The discussion of subglacial sediment transport does not only affect our understanding of glacial stability (e.g. Alley and Whillans, 1991; MacAyeal, 1992; Clark, 1994), but also likely governs processes behind formation of subglacial landforms such as drumlins. Hindmarsh (1998) and Fowler (2000) showed that a till with a pressure-dependent viscosity amplifies small perturbations in basal topography. The initially small perturbations grow as kinematic waves due to spatially variable transport rates. Schoof (2007) revisited this idea and noted that the instability theory of drumlin formation is likely relevant irregardless of till rheology. He noted that the only prerequisite is that the till flux ($\boldsymbol{q}$ in Eq. 2.29) is dependent on effective normal stress, since bed-normal stresses are larger at the stoss side of bed bumps than on the lee side. The increase in transport capacity predicted by our numerical granular experiments (Fig. 2.6, left) on the stoss side produces a relatively large till flux, whereas the transport capacity decreases on the lee side. This transport variability, if applicable to the subglacial environment, is likely to grow preex-

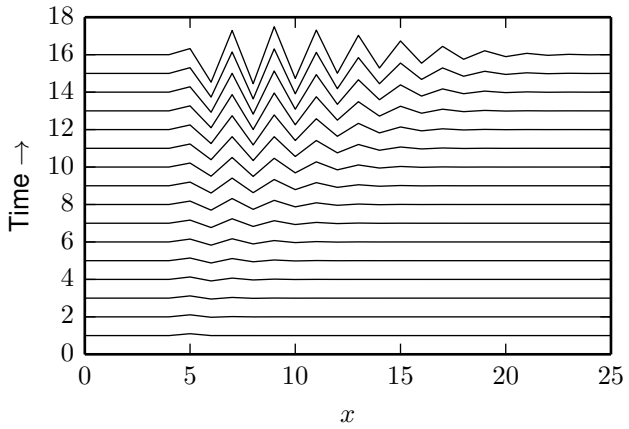

Figure 2.7. Instability growth due to differential sediment transport in the deforming bed. Flow towards the right.

isting bumps in the deformable bed, possibly leading to wavy landforms on larger scales such as drumlins (e.g. Clark, 2010), ribbed moraines (e.g. Dunlop et al., 2008) and correlate to regularly varying subglacial stress patterns inverted from Antarctic glaciers (e.g. Joughin et al., 2004; Sergienko and Hindmarsh, 2013).

The instability growth is illustrated in the following simple one-dimensional example. I assume a constant effective normal stress N and driving stress τ, and a constant shear velocity at the IBI. The stress is projected onto the bed-normal vector:

$$N_\perp = N\cos\alpha + \tau\sin\alpha \tag{2.30}$$

where α is the local bed slope. Assuming that the depth of deformation depends on the bed-normal stress scaled by a factor c, the sediment flux q_x can be approximated by:

$$q_x \approx \frac{1}{2} c N_\perp u \tag{2.31}$$

where u is the horizontal velocity. The evolution of the bed topography H is governed by the divergence of sediment flux by assuming no sediment exchange with the glacier base:

$$\frac{\partial H}{\partial t} = \frac{\partial q_x}{\partial x} \tag{2.32}$$

A small bump is placed at $x = 5$, which seeds the instability mechanism due to differential sediment transport (Fig. 2.7). The bump leaves several down-flow ripples, which progressively decrease in amplitude. The instability process is analogous to ripple or dune formation (e.g. Kennedy, 1969; Werner, 1995). All processes share the common feature that transport rates are larger on the stoss side than on the lee side.

The above example does not include the presumably important feedbacks from subglacial hydrology or the bed-smoothing effect due to ice viscosity and elasticity. It does, however, demonstrate the potential for landform development due to

pressure-dependent till advection in the deforming bed, and that this instability theorem is agreeable with Mohr-Coulomb plasticity.

Paper 2 in this thesis (Ch. 5) shows that if the sediment has a low permeability and is in a pre-failure state, dilatant-hardening processes strengthen the material and can either increase or decrease the depth of deformation. If the water pressure at the IBI is constant, the depth of deformation decreases as hardening processes are less important here (Fig. 2.6, right). If the water pressure at the IBI decreases during deformation due to limited regional recharge, strain is expected to be distributed over larger depths. The strength of the dilatant hardening processes is governed by the ratio between rate of volumetric change and permeability, where the strengthening is more important at larger ratio values.

2.4 Subglacial channels

Subglacial water directly influences the effective pressure, which is a first-order control of basal friction. This relationship is included in most modern hard-bed sliding laws (e.g. Fowler, 1986; Schoof, 2005), and most soft-bed sliding laws discussed above (Eqs. 2.16, 2.17, 2.18, and 2.25). Several studies have noted the importance of the subglacial hydraulic system to overall glacier movement, both on soft and hard beds (e.g. Piotrowski, 1997; Iken and Truffer, 1997; Ng, 2000a; Zwally et al., 2002; Schoof, 2010b; Iverson, 2010; Bartholomaus et al., 2011; Stevens et al., 2015).

Subglacial water flows opposite to the hydropotential gradient governed by ice surface topography, bed topography, and water pressure (e.g. Cuffey and Paterson, 2010), and can take place through several modes of flow (e.g. Flowers, 2015). In the distributed flow mode water flows along a thin film or through a system of linked cavities at the IBI. On soft beds or fractured bedrock water can flow through the substratum as groundwater. Discrete flow happens where channels are melted, abraded or cracked into the ice, substratum, or a combination of the two. Earliest mathematical models of subglacial hydrology included one of the drainage modes, e.g. channelized flow on hard beds (e.g. Röthlisberger, 1969; Nye, 1976) or groundwater flow in the subglacial till (e.g. Shoemaker, 1986; Lingle and Brown, 1987).

Distributed drainage modes (interfacial water films, linked cavities, groundwater) are inefficient at evacuating subglacial water, and as a consequence generally weaken the subglacial bed as they reduce the mechanical coupling between ice and bed. Channelized flow is the most efficient mode of water transport, but requires large water fluxes to balance the closure rates of ice and substratum. Due to their efficient drainage, channels often have a lower water pressure than adjacent areas and form a dendritic network draining the IBI. The efficient drainage lowers subglacial water pressure and increases the effective pressure between ice and bed, in turn increasing basal friction. Theoretical considerations and observations show that subglacial meltwater production in many cases exceeds the capacity of the distributed system, and flow localizes in more transport-efficient channels. The variability between these two modes is the most important control on ice sheet stability (e.g. Schoof, 2010b). Jökulhlaups are a notable example of how sudden large-volume input of water to the subglacial bed overwhelm the subglacial hydrological system, causing a transient evolution of distributed to channelized flow, often associated with glacier acceleration (e.g. Bartholomew et al., 2010; Stevens

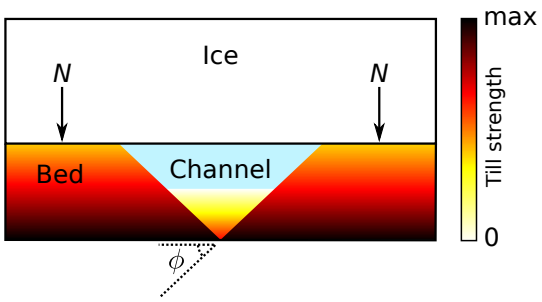

Figure 2.8. Cross-sectional geometry of the stress states in an idealized channel incised into subglacial till with Mohr-Coulomb plasticity. ϕ denotes the material angle of internal friction.

et al., 2015). Recent developments have improved the mathematical description of coupled distributed and channelized drainage modes on hard beds, e.g. linked cavities and R-channels (Schoof, 2010b; Werder et al., 2013) or a IBI water sheet and R-channels (Creyts and Schoof, 2009; Hewitt, 2011).

Walder and Fowler (1994) defined a model for subglacial channelized on soft beds. Their model combines melting of the glacier bottom into a semicircular Röthlisberger-type channel (Röthlisberger, 1972; Nye, 1976) through turbulent heat dissipation, counteracted by creep closure due to cryostatic pressure, as well as sediment erosion from the channel flow at the channel base, counteracted by slight non-linear viscous till creep closure (Eq. 2.16, Boulton and Hindmarsh (1987) and Fowler and Walder (1993)). The treatment of sediment transport in the model was subsequently improved by Ng (2000b). Later model formulations by Kyrke-Smith and Fowler (2014) discarded the mathematical distinction between discrete channels and distributed water sheets, and unified the description as a continuous water sheet with variable thickness that can approach channelized flow.

The channel formulation of Walder and Fowler (1994) extended by Ng (2000b) has shown to successfully reproduce observed events of subglacial drainage (Carter et al., 2015). The till channel model (Walder and Fowler, 1994; Ng, 2000b) has been criticized due to the choice of till rheology (e.g. Hindmarsh, 1997). The water sheet model including sediment deformation (Kyrke-Smith and Fowler, 2014) uses the mildly non-linear viscous Bingham model (Eq. 2.17, Boulton and Hindmarsh (1987)), which has not been verified experimentally. Other models of soft-bed subglacial channels have avoided the explicit treatment of subglacial till deformation by letting the lower channel surface evolve by the same dynamics governing channel incision into the ice (Wel et al., 2013).

From the work done in this thesis, I propose future research on a new model for subglacial till channels, where the stability is based on the well established Mohr-Coulomb constitutive relation for till mechanics (Eq. 2.18, Fig. 2.8). As in previous formulations for subglacial channel evolution, the channel is expected to deepen by a stream-power law scaling erosion rate with water flux (e.g. Walder and Fowler, 1994). The evolution of the channel geometry is analyzed by assuming traditional granular behavior, however. The channel flanks and sediment volumes beneath the angle of internal friction are loaded by the effective stress supplied at the ice-bed interface and lithostatic pressure, while a wedge directly beneath the

channel is only loaded by its own lithostatic pressure. Under hydrostatic pressure distribution, lithostatic pressure causes the shear strength to increase linearly with depth, while pore-pressure fluctuations can cause deviations in shear strength (e.g. Tulaczyk et al., 2000a; Fowler, 2010). The erosion and deposition of sediments by the channel flow is expected to be governed by the Hjulström relation between water flow velocity, sediment grain size, and transport capacity (Hjulstrom, 1939). The erosion predicted from the Hjulström relation will be scaled by a stream power-type law where erosion depends on water shear stress and grain size (e.g. Wilcock, 1998; Whipple and Tucker, 1999).

The numerical model for granular and pore-water interaction developed in this thesis can be used to test the channel geometry, stability, and response to different rates of erosion. Subglacial sediment transport by channelized water is potentially important to spatial patterns of glacier erosion (Alley et al., 2003). Similarly, transport of sediment in channels has the potential to control downstream channel dynamics as flowing pathways can become clogged by sediment if flow velocities decrease. As water flow in the channel increases its transport capacity, erosion is expected to increase channel cross-sectional area in a self-similar geometry, dictated by sediment mechanical properties. Episodes of rapid decrease in channel pressure are expected to cause spontaneous channel closure as liquefaction draws sediment into the channel. Subsequent water pulses are required to reestablish the channel geometry, which initially increases water pressure distribution spatially and weakens the frictional resistance of the bed.

As discussed in the previous, understanding subglacial hydraulic systems is in many cases key to understanding glacier flow. The theoretical evolution of subglacial water flow is extremely sensitive to the model and parameter choice. Current models of soft-bed channelized flow rely on constitutive models for till behavior which are considered in conflict with the majority of empirical data. This discrepancy underpins the need of reconsidering the channel-governing processes.

Chapter 3

Conclusions and future aspects

The coupled computational model of discrete element method (DEM) and pore-water has in this study provided in-depth understanding of processes and mechanics of slowly deforming water-saturated granular beds. The time spent on the computationally demanding DEM simulations has been reduced by offloading all parts of the numerical algorithm for computation on the massively parallel graphics processing unit (GPU) platform. The experiments have revealed detailed insight into the diversity of granular rheology (Ch. 2, 4–6), granular advection (Ch. 2, 4, and 5), and pore-water interaction (Ch. 5 and 6).

In the following I will revisit the main research questions from the introduction (Ch. 1) and briefly summarize the findings of this PhD project. Afterwards I will present some opportunities for improving the computational model and widen its applicability.

Is the DEM viable for numerical studies of subglacial sediment deformation?

The DEM is the most commonly used method to simulate granular materials, since continuum methods still are unable to capture their rich physical properties. However, the DEM is computationally expensive as it requires fine temporal discretization (Ch. 4 and 7). The physical interaction of clay particles is well constrained (e.g. Yao and Anandarajah, 2003), but numerical simulation of a wide grain-size distribution as shown in most tills is not possible due to several computational constraints:

- The length of the numerical time step is dictated by grain size and elastic properties. A clay-sized particle causes a time step is on the order of 10^{-15} s, increasing the computational requirements by a factor of 10^8 relative to the experiments presented as part of this PhD project.

- The contact search distance between grains is determined by the largest grain size (Ch. 7). A wider range of grain sizes causes heavier computational requirements during the grain contact search.

- Many tills display a fractal grain-size distribution, implying that the largest grain size dictates the number and sizes of smaller grains above a lower size limit (e.g. Hooke and Iverson, 1995). The grain-size distribution of till often

is described by a fractal dimension of −2.9, which means that for each 1 cm particle there are on the order of 10^{11} particles smaller than it.

Facing these limitations, we chose instead to use the DEM to investigate the most fundamental dynamics in simple granular materials, and apply the achieved insights to the subglacial setting while acknowledging the simplifying assumptions. This approach was successful and has improved our understanding of subglacial deformation of unlithified sediments.

What is the appropriate constitutive relation for granular materials deforming under subglacial conditions?

Our results from laboratory and numerical shear experiments conformed to the notation that till and other granular materials deform in a nearly rate-independent manner when stressed above the Mohr-Coulomb yield strength (Ch. 2 and 4). Viscosity known from *Bagnold* granular flows is not important as the average kinetic energy per grain is low relative to the contact duration (GDR-MiDi, 2004). Shear strength undergoes rapid changes during early deformation as the shear zone evolves into a layer of high porosity, but ultimately remains at a critical-state value.

What controls the distribution of subglacial strain with depth, and what are the implications for sediment flux and till continuity?

Shear strain in granular materials does not conform to a single surface, but the granularity of sediments imposes a minimum shear band thickness scaled by grain size and effective stress normal to the bed (Ch. 4 and 5). The relationship to effective normal stress may cause growth of bumps at the ice-bed interface (IBI), analogous to the instability mechanism of ice flow over viscous till beds proposed by Hindmarsh (1998) and Fowler (2000).

What is the appropriate methodology to simulate coupled granular and fluid dynamics in the subglacial bed?

Initial development and implementation of a full Navier-Stokes method for pore water proved suboptimal for simulating flow in low permeability materials (Ch. 8). Darcian flow is adequate for describing pore-water dynamics in the subglacial bed, however (Ch. 5 and 8, Goren et al. (2011)). Due to low fluid and grain velocities, fluid-drag forces are negligible. The interaction between the granular and fluid phase is mainly caused by local pore-pressure deviations from the hydrostatic pressure distribution and porosity changes.

Do water pressure dynamics caused by subglacial deformation influence till rheology and flux?

Deformation of consolidated granular materials causes volumetric expansion (Ch. 4). If the rate of pore space growth outpaces the diffusion of hydraulic pressures, significant reductions in pore-water pressure occur (Ch. 5, Iverson et al. (1998)). The pore-pressure drop pushes surrounding grains together and effectively strengthens the granular skeleton. The hardening is rate dependent and

transient, and may stabilize patches in the subglacial bed leading to differential strength and landform development (Piotrowski, 1987; Clark, 2010).

How does variable input of meltwater influence stability of the subglacial bed?

Pore-water pressure exerts a first-order control on sediment strength as it modifies the yield strength. Events of high pore-water pressure cause a basal weakening which may cause widespread basal deformation, but in many cases instead reduces mechanical coupling between ice and bed (Hooke et al., 1997; Fischer and Clarke, 1997).

Hydraulically driven transient stress perturbations can cause slow creep deformation beneath the yield strength, caused by reorganization in the internal network of stresses in the granular bed (Ch. 2 and 6).

3.1 Extending the numerical model

Heat budgeting

The model can be extended to include heat production, advection, and diffusion. Energy is released on the contacts between grains during relative motion (Goren and Aharonov, 2007; Galindo-Torres et al., 2012), and during viscous deformation of the pore fluid (e.g. Gerya, 2010; Cuffey and Paterson, 2010). A value commonly used for the thermal pressurization coefficient is 0.5 MPa K^{-1} (Rempel et al., 2003; Goren and Aharonov, 2007). This value implies that a 1 K warming of pore water in the undrained case increases the pore-water pressure with 500 kPa. An increase in pore-water pressure decreases effective pressure, causing lower sediment strength.

The thermal softening due to lowered effective normal stress is expected to be transient like the dilatant hardening described in Ch. 5, and by the same extent regulated by the ratio between deformation rate and pore-pressure diffusion rate.

Debris-rich basal ice

Glaciers commonly experience the largest internal deformation near the glacier bed due to the non-linearity of Glen's law (Glen, 1955; Hooke, 1981). The basal ice is often rich in debris, and the deformational properties of this zone may be significantly different from clean ice due to sediment content and stratification (Hubbard and Sharp, 1989; Christoffersen and Tulaczyk, 2003a). Deformation in this layer is potentially important for glacier motion and sedimentary processes (Hubbard and Sharp, 1989; Hart, 1998; Alley et al., 1998; Piotrowski et al., 2001).

A new variant of the pore-fluid equations (Ch. 8) could be derived where the pore-fluid flows according to Glen's law for non-linear creep of polycrystalline ice, and numerically implemented by iteratively solving for the full Cauchy stress tensor. Instead of simulating nearly inviscid melt-water in the granular pores, this method would allow for computational deformation experiments of debris-rich basal ice.

Coupled with a solution for heat, the non-linearity of ice rheology this is likely to focus deformation in thinner bands as the temperature directly influences the

creep factor A in the equation for ice rheology (Glen, 1955; Cuffey and Paterson, 2010). Heat production during deformation is likely different between clean and dirty ice layers, further enhancing differences in deformational properties.

Breakable grain bonds

Three immediately apparent shortcomings of the current granular model is the inability to handle cohesion, complex grain shapes and grain crushing. All three limitations can be handled by including a formulation allowing for breakable bonds between grains. Complex grain shapes can be constructed by filling a volume with smaller grains and constructing bonds between them. With an included model for bonding, experiments can be performed testing hypotheses regarding development of grain fabric and modification of the grain-size distribution with progressive shear strain.

Here I include an example formulation based on the incremental algorithm of beam mechanics presented by Potyondy and Cundall (2004), but expanded with viscous damping terms. The incremental method is simpler to implement than the more complex total method proposed in Wang et al. (2006) and Wang (2009). The bonds react to tensile, shear, torsion and bending strain (Tab. 3.1). When the bond strains exceed a defined limit ($\bar{\sigma}_c < \bar{\sigma}^{\max}$ or $\bar{\tau}_c < \bar{\tau}^{\max}$), the bond is deleted meaning the inter-grain contact is broken.

Table 3.1. Inter-grain bond description

Definition	Physical meaning
$\boldsymbol{f}_{\mathrm{n}}{}^{i} = -\boldsymbol{f}_{\mathrm{n}}{}^{j} = k_n A \delta_{\mathrm{n}}{}^{ij} + \gamma_{\mathrm{n}} \dot{\delta}_{\mathrm{n}}{}^{ij}$	Contraction/expansion of bond
$\boldsymbol{f}_{\mathrm{t}}{}^{i} = -\boldsymbol{f}_{\mathrm{t}}{}^{j} = -k_t A \boldsymbol{\delta}_{\mathrm{t}}{}^{ij} - \gamma_{\mathrm{t}} \dot{\boldsymbol{\delta}}_{\mathrm{t}}{}^{ij}$	Shear of bond
$\boldsymbol{t}_{\mathrm{n}}^{j} = -\boldsymbol{t}_{\mathrm{n}}^{i} = k_n J \boldsymbol{\Omega}_{\mathrm{n}}^{ij} + \gamma_{\mathrm{n}} \dot{\boldsymbol{\Omega}}_{n}^{ij}$	Twist of bond
$\boldsymbol{t}_{t}^{j} = -\boldsymbol{t}_{t}^{i} = -k_n I \boldsymbol{\Omega}_{t}^{ij} - \gamma_{\mathrm{t}} \dot{\boldsymbol{\Omega}}_{t}^{ij}$	Bend of bond
$\bar{\lambda}$	Bond radius multiplier
$\bar{r} = \bar{\lambda} \min(r^i, r^j)$	Effective bond radius
$A = \pi \bar{r}^2$	Bond cross sectional area
$I = \frac{1}{4} \pi \bar{r}^4$	Contact parallel moment of inertia
$J = \frac{1}{2} \pi \bar{r}^4$	Contact normal (polar) moment of inertia
$\bar{\sigma}_c$	Tensile strength
$\bar{\tau}_c$	Shear strength
$\bar{\sigma}^{\max} = -\lvert\lvert \boldsymbol{f}_n^i \rvert\rvert / A + \lvert\lvert \boldsymbol{t}_t^i \rvert\rvert \bar{r} / I$	Maximum tensile stress
$\bar{\tau}^{\max} = \lvert\lvert \boldsymbol{f}_t^i \rvert\rvert / A + \lvert\lvert \boldsymbol{t}_n^i \rvert\rvert \bar{r} / J$	Maximum shear stress

The cohesive bond force is linear-elastic like the implemented repulsive contact force (Ch. 7 Cundall and Strack, 1979; Damsgaard et al., 2013). The viscous terms are included to allow for energy dissipation, and can be excluded by setting the viscosities ($\gamma_{\mathrm{n,t}}$) to zero. The bonds can transmit both force ($\boldsymbol{f}$) and torque ($\boldsymbol{t}$) between particles. For a bonded particle pair, members denoted with superscripts i and j, the bond force is calculated on a base of the relative contact linear displacement ($\delta_{\mathrm{n}}{}^{ij}$) and contact rotational displacement ($\boldsymbol{\Omega}^{ij}$). The relative linear and rotational displacement is decomposed into the current contact plane normal and tangential components (table 3.1), and applied to particles i and j according to Newton's third law. After calculating the bond force and torque components, the corresponding maximum tensile ($\bar{\sigma}^{\max}$) and shear stress ($\bar{\tau}^{\max}$) is calculated

according to beam theory. If one of these values exceed the defined bond tensile ($\bar{\sigma}_c$) or shear strength ($\bar{\tau}_c$), the bond is removed.

Fabric evolution

Till fabric is a characterization of the *in-situ* orientation of a stochastic population of elongated particles. The similarity in orientation of gravel-sized grains or clay matrix is usually described by the eigenvalue method (Mark, 1973; Elias, 2006). The degree of clustering (S_1: eigenvalue) around the preferred orientation (V_1: principal eigenvector) can be used as a proxy for the cumulative shear strain in subglacial till (Hart, 1994; Hooyer and Iverson, 2000b; Thomason and Iverson, 2006; Iverson et al., 2008). The precise rotational behavior of elongated clasts during shear has long been a subject of discussion, however (Larsen and Piotrowski, 2003; Elias, 2006). Two processes have been proposed for fabric development in a subglacial deforming bed, dependent on the appropriate model of till rheology:

- Jeffery (1922) rotation: Rotational movement occurs due to velocity gradients. Clasts are free to rotate and the continuous rotation results in a weak fabric ($S_1 \approx 0.6$). This mode of rotation is appropriate for clasts in viscous materials (Hicock and Dreimanis, 1992; Hart, 1994; Thomason and Iverson, 2006).
- March (1932) rotation: Rotational movement occurs due to deviatoric stresses. Elongated and platy particles attend a stable position perpendicular to maximum compressive stress, resulting in a strong fabric ($S_1 \approx 0.8$). This rotation mode is observed in plastic materials (Hooyer and Iverson, 2000b; Larsen and Piotrowski, 2003; Thomason and Iverson, 2006; Iverson et al., 2008).

The bond-methodology described above can be used to simulate elongated grains, offering the possibility to continuously monitor the fabric development under different normal stress magnitudes and shear velocities. It is expected that the numerical model displays March rotation, similar to the laboratory experiments by Hooyer and Iverson (2000b), but sediment liquefaction on the lee side of ploughing bumps may cause continuous rotation.

Development of grain-size distribution

Active subglacial transport can modify the material grain size distribution by particle breakage or abrasion, and the bimodal or polymodal distributions found in till may be a result of these two comminution mechanisms (Boulton, 1978; Haldorsen, 1981; Benn and Evans, 2014). Hooke and Iverson (1995) and Iverson et al. (1996) argued that failure of grains in force-chain networks during shear significantly modifies the particle sizes, leading to a self-similar and fractal grain-size distribution. During comminution the finer components become increasingly important for distributing the stresses through the system. The mesh spacing in the system of force chains is a function of the typical grain size. The mesh size is expected to decrease with comminution, in effect homogenizing the stress network. In this state the amplitude of the stress fluctuations during shear decrease, and intergranular sliding and abrasion is favored to crushing. Iverson et al. (1996) argue that large remnant clasts survive due to isolation from other large clasts by

the finer components. The reduction of aggregate sizes during progressive shear and the evolution in the force chain mesh can be analyzed by choosing sensible values of the bond tensile ($\bar{\sigma}_c$) and shear strength ($\bar{\tau}_c$) in the bonded granular model.

Papers and research notes

Chapter 4

Paper 1: *Discrete element modeling of subglacial sediment deformation*

Anders Damsgaard[1], David L. Egholm[1], Jan A. Piotrowski[1], Slawek Tulaczyk[2], Nicolaj K. Larsen[1], and Karol Tylmann[3]

1. Department of Geoscience, Aarhus University, Aarhus C, Denmark.
2. Department of Earth and Planetary Sciences, University of California, Santa Cruz, California, USA.
3. Department of Earth Sciences, N. Copernicus University, Toruń, Poland.

Printed in *Journal of Geophysical Research: Earth Surface*, vol. 118, 2230–2242, 2013.

Abstract

The discrete element method (DEM) is used in this study to explore the highly nonlinear dynamics of a granular bed when exposed to stress conditions comparable to those at the bed of warm-based glaciers.

Complementary to analog experiments, the numerical approach allows a detailed analysis of the material dynamics and the shear zone development during progressive shear strain. The geometry of the heterogeneous stress network is visible in the form of force-carrying grain bridges and adjacent, volumetrically dominant, inactive zones. We demonstrate how the shear zone thickness and dilation depends on the level of normal (overburden) stress, and we show how high normal stress can mobilize material to great depths. The particle rotational axes tend to align with progressive shear strain, with rotations both along and reverse to the shear direction.

The results from successive laboratory ring-shear experiments on simple granular materials are compared to results from similar numerical experiments. The simulated DEM material and all tested laboratory materials deform by an elasto-plastic rheology under the applied effective normal stress.

These results demonstrate that the DEM is a viable alternative to continuum models for small-scale analysis of sediment deformation. It can be used to simulate the macromechanical behavior of simple granular sediments, and it provides an opportunity to study how microstructures in subglacial sediments are formed during progressive shear strain.

4.1 Introduction

Deformation of subglacial sediment may be a major contributor to the overall movement of warm-based glaciers and ice streams(e.g. Alley et al., 1986; Boulton and Hindmarsh, 1987; Engelhardt et al., 1990; Kamb, 1991; Boulton, 1996), and it is also suspected to influence the periodic dynamics ofsurge-type glaciers (Boulton and Jones, 1979; Clarke et al., 1984; Evans and Rea, 1999; Murray et al., 2000; Murray et al., 2003). In addition, subglacial deformation is sometimes regarded as the primary mechanism for sediment advection/discharge (e.g. Kjær et al., 2006; Nygård et al., 2007). However, the physics of subglacial sediment deformation are still debated, and the deformation mode remains one of the most controversial elements of glacier dynamics (e.g. Boulton and Hindmarsh, 1987; Hindmarsh, 1998; Fowler, 2003; Tulaczyk, 2006; Cuffey and Paterson, 2010).

Based on field measurements of deep sediment deformation, Boulton and Hindmarsh (1987) suggested that subglacial sediment behaves like a viscoplastic material. Visco-plastic continuum models have since been popular among computational ice-sheet models (e.g. Alley et al., 1987b; Hindmarsh, 1998; Fowler, 2000; Ng, 2000b), for which the rate-dependent viscous models offer a convenient one-to-one relationship between stress and strain rate. Contrasting this approach, Schoof (2006) described a possible implementation of a basal boundary condition with a plastic yield stress to glacial flow models. The coupled system of glacial hydrology and nonlinear basal sediment behavior has been reported to be of great importance for stick-slip events (Bueler and Brown, 2009; Bougamont et al., 2011; Bougamont and Christoffersen, 2012).

As noted by e.g. Kamb (1991) and Iverson (2010), laboratory shear-experiments on subglacial sediment do not confirm the rate-dependent viscous-plastic model,

but instead indicate that subglacial sediment deforms due to Coulomb slip, independently of the applied strain rate. Tulaczyk et al. (2000a) and Iverson and Iverson (2001) demonstrated that subglacial till, deforming according to the Mohr-Coulomb plastic rheology, may also produce the deep-seated deformation profiles that are observed in the field and often associated with a visco-plastic behavior.

However, subglacial sediment is first and foremost a granular material with an inherent ability to change mechanical behavior, depending on the stress state, deformation rate, and pore water pressure. This study presents the first effort to apply the discrete element method (DEM) (also called the distinct element method) (Cundall and Strack, 1979) for studying the granular physics of subglacial till deformation. This method was first suggested in this context by Iverson and Iverson (2001) and Fowler (2003).

We explore the applicability of the DEM as an alternative to the continuum-based visco-elastic-plastic methods for modeling subglacial deformation. A discrete modeling approach can capture the highly nonlinear dynamics of subglacial deformation, as demonstrated by laboratory shear experiments on subglacial sediment samples (Iverson et al., 1997a; Tulaczyk, 1999; Thomason and Iverson, 2006; Rathbun et al., 2008; Iverson, 2010). As a supplement to laboratory experiments, numerical modeling offers complete control over all model parameters, such as grain size distribution , geotechnical properties of the material, and boundary conditions. This facilitates a more transparent experimental setup whereby it is possible to repeat experiments and quantify the effects of all input parameters. The numerical approach allows a detailed analysis of the particle kinematics, during and after the experiment. This small-scale analysis exceeds the capacity of laboratory experiments, but the numerical experiments are however constrained by the number of particles and simplifying assumptions about the particle shapes.

Here we first present previous studies on the topic of granular mechanics. We then describe the details of the applied numerical model, as well as the setup and results of shear experiments. We take a closer look at the internal characteristics of the shear zone from the numerical experiments, and the implications for subglacial deformational processes. Finally, we compare the modeled macroscopical mechanical behavior to the results of laboratory ring-shear experiments on different granular materials.

4.2 Granular mechanics during shear

In the field of glacial micromorphology, micro-scale deformation structures have been categorized as either brittle, ductile or polyphase, suggesting a natural variability in the mode of deformation (Meer, 1993; Meer, 1996; Menzies, 2000; Larsen et al., 2006; Phillips et al., 2013; Vaughan-Hirsch et al., 2013). Generally, the physical properties of granular materials cannot be fully described by ideal viscous or elasto-plastic continuum relationships . Depending on the average kinematic energy of each grain or particle, a granular assemblage can assume properties of solid-like, fluid-like, or even gaseous states (e.g. Jaeger et al., 1996). At rest, under the influence of gravity and confining stress, granular matter forms a stable packing and behaves like a solid, and the same material can take a range of packing densities, dependent on the style of deposition and the stress history (Herrmann, 2002). Overall, the rheology of all dry granular materials is strain-rate independent at low shearing velocities, where they deform in a pseudo-static

state. If granular materials deform under higher shearing velocities, particle inertia dominates and deformation becomes rate dependent (*Bagnold flow*) (Zhang and Campbell, 1992; Campbell, 2006; Krimer et al., 2012). In confined shear experiments, the dimensionless inertia parameter I is defined by:

$$I = \dot{\gamma}\bar{r}\sqrt{\frac{\rho}{\sigma_0}} \tag{4.1}$$

where $\dot{\gamma}$ is the shear strain rate, $\bar{r}$ is the mean particle radius, ρ is the material density, and σ_0 is the magnitude of the normal stress (GDR-MiDi, 2004). Experiments and simulations show that the material deforms in a pseudo-static and rate-independent manner when $I < 10^{-3}$ (GDR-MiDi, 2004).

Aharonov and Sparks (2002) conducted two-dimensional DEM simulations of shear experiments on granular material, and recognized two different modes of strain localization, depending on the applied levels of shear velocity and normal stress. With relatively low normal stress and high shear velocity, the deformation was characterized by shallow deformation in a persistent boundary layer shear zone. In contrast, the deformation was deep and distributed for higher stress levels and lower shearing velocities.

Reynolds (1885) and Mead (1925) recognized that initially consolidated, rigid granular materials, subjected to a shearing stress, require an increase in volume (dilatancy) to deform. When the shearing motion stops, the shear zone collapses and compacts due to the compressive stress. The shear strain is often localized in shear zones, which can have a range of sizes, dependent on the boundary conditions and material properties. The minimal thickness in non-cohesive materials is in the order of 5–10 grain diameters (Gennes, 1999). Herrmann (2001) suggested a typical shear band thickness minimum, based on considerations of the force acting to mobilize particles. As a result of contact friction between neighboring particles, the magnitude of the mobilization force is inversely proportional to the distance along the stress bearing force chains. This stabilizing effect causes the shear induced particle velocity to decay exponentially with the distance from the center of the shear band.

If elastic deformation is ignored, the behavior of granular materials (including tills) can be approximated by the Mohr-Coulomb failure criteron (e.g. Boulton and Jones, 1979; Nedderman, 1992; Hooke et al., 1997; Clarke, 2005; Iverson, 2010). For Mohr-Coulomb materials, the macromechanical angle of internal friction (ϕ) and the cohesion (C) are defined from the linear representation of the value of the material *peak* or *ultimate* shear strength (τ_{p}, τ_{u}) under a range of normal stress magnitudes (σ_0):

$$\tau_{p,u} = C_{p,u} + \sigma_0 \tan(\phi_{p,u}) \tag{4.2}$$

Most materials can display a range of shear strengths, depending on the consolidation state. Consolidated materials in a pre-failure state typically have a higher peak value of shear strength (τ_p) than materials in the *critical state* with a fully developed, active shear zone and a residual, ultimate shear strength (τ_u) (Schofield and Wroth, 1968; Nedderman, 1992). Similarly, the material cohesion can change during deformation. In particlular, the peak cohesion is higher than the ultimate cohesion if the cohesive bonds between grains are not reestablished after breaking.

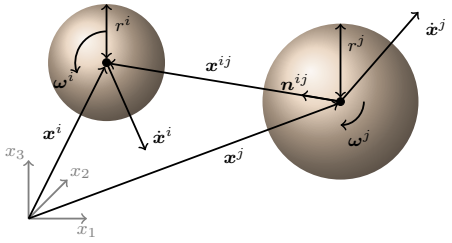

Figure 4.1. The DEM particles are represented by spheres with center position $\boldsymbol{x}$ and radius r. The velocity vector of a particle is denoted $\dot{\boldsymbol{x}}$, and the angular velocity vector is $\boldsymbol{\omega}$. A particle pair is characterized by the inter-particle vector $\boldsymbol{x}^{ij}$, and the contact normal vector $\boldsymbol{n}^{ij}$.

4.3 The discrete particle model

The Discrete Element Method DEM wasinitially formulated by Cundall and Strack (1979). The computational method simulates the physical behavior of discontinuous materials in a way that is ideal for reproducing the highly nonlinear dynamics of granular materials. The DEM has, in addition to geotechnical simulations (e.g. Cheng et al., 2003; Potyondy and Cundall, 2004), already been used for simulating various sedimentological transport modes, such as debris flows (Yohannes et al., 2012), bedload transport (Drake and Calantoni, 2001), aeolian saltation (Sun et al., 2001), mechanical sorting (e.g. Rosato et al., 2002; Kudrolli, 2004), as well as sandbox deformation experiments (Egholm et al., 2007; Egholm et al., 2008) and mechanical properties of fault gouges in the earthquake generation process (e.g. Morgan and Boettcher, 1999; Morgan, 1999; Morgan, 2004; Mair and Abe, 2008).

The DEM simulates the micromechanical behavior and interaction of discrete, unbreakable particles with their own mass and inertia, under the influence of e.g. gravity and boundary conditions such as moving walls. The particulate nature of the DEM is optimal not only for capturing the discrete nature of granular physics, but also for simulating the large strains observed in soft subglacial beds. In contrast, mesh-based continuum numerical methods (e.g. the finite element method (FEM), the finite difference method (FDM), and the finite volume method (FVM)) cannot simulate high deformation without frequent re-meshing, which is often a very complicated and computationally expensive task. Additionally, the shear zone dynamics in standard continuum plasticity models are often affected by the grid resolution and the mesh-line orientation (Rudnicki and Rice, 1975; Borst, 1991).

The DEM includes deformation-induced porosity changes as an inherent property because, like true sediment grains, model particles must move past each other. In addition, the DEM responds naturally with granular-style deformation patterns, which can take place in a distributed manner over larger parts of the volume, or in localized shear zones.

In the applied DEM formulation, the particles are represented as spheres, which reduces the complexity of the contact search and dynamics. The geometric extent of each particle is represented by a position vector $\boldsymbol{x}$, and a radius r. Each particle

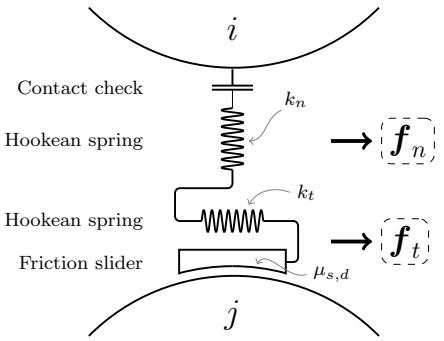

Figure 4.2. Schematic representation of the contact model components, normal and tangential to the contact plane.

has individual kinematic attributes, as illustrated in Figure 4.1. Based on the net force acting on each particle, the resulting movement is calculated in every small time step (Δt) by application of Newton's law of motion for particles of constant mass. For a particle i with n_c contacts, the sums of translational and rotational forces are expressed by:

$$m^i \ddot{\boldsymbol{x}}^i = \underbrace{m^i \boldsymbol{g} + \sum_j^{n_c} \left(\boldsymbol{f}_{\mathrm{n}}{}^{ij} + \boldsymbol{f}_t^{ij} \right)}_{\text{Sum of translational forces}} \tag{4.3}$$

$$I^i \ddot{\boldsymbol{\Omega}}^i = \underbrace{\sum_j^{n_c} \left(-\left(r^i + 0.5 ||\delta_{\mathrm{n}}{}^{ij}|| \right) \boldsymbol{n}^{ij} \times \boldsymbol{f}_{\mathrm{t}}{}^{ij} \right)}_{\text{Sum of torques}} \tag{4.4}$$

where m is the particle mass, $\boldsymbol{g}$ is the gravitational force vector, I is the moment of inertia, and $\boldsymbol{\omega}$ is the angular velocity. A dot denotes time derivation, a bold formatted symbol represents a three-dimensional vector.

A particle is in contact with another particle or a wall if the volumes overlap. For a pair of spherical particles, hereafter denoted with superscripts i and j, the contact search is a simple operation, involving only the particle center coordinates and radii. The particle overlap is

$$\delta_{\mathrm{n}}{}^{ij} = ||\boldsymbol{x}^{ij}|| - (r^i + r^j) \tag{4.5}$$

where $\boldsymbol{x}^{ij} = \boldsymbol{x}^i - \boldsymbol{x}^j$ is the inter-particle vector. Particles overlap when $\delta_n^{ij} < 0$, in which case the force components normal ($\boldsymbol{f}_{\mathrm{n}}$) and tangential ($\boldsymbol{f}_{\mathrm{t}}$) to the contact plane are assumed to obey a conventional linear-elastic contact model (Figure 4.2): contact model

$$\boldsymbol{f}_{\mathrm{n}}{}^{ij} = -k_{\mathrm{n}} \delta_{\mathrm{n}}{}^{ij} \boldsymbol{n}^{ij} \quad \text{and} \quad \boldsymbol{f}_{\mathrm{t}}{}^{ij} = -k_{\mathrm{t}} \boldsymbol{\delta}_{\mathrm{t}}{}^{ij} \tag{4.6}$$

where $\boldsymbol{n}^{ij} = \boldsymbol{x}^{ij} / ||\boldsymbol{x}^{ij}||$ is the contact normal vector. k_{n} and k_{t} are the linear-elastic (Hookean) spring coefficients. The tangential displacement along the contact plane ($\boldsymbol{\delta}_{\mathrm{t}}{}^{ij}$) is calculated incrementally by temporal integration of the tangen-

tial contact velocity, and saved for the duration of the contact. The contact velocity $\dot{\boldsymbol{\delta}}$ is found from the translational and rotational velocities of the particles in contact (Hinrichsen and Wolf, 2004):

$$\dot{\boldsymbol{\delta}}^{ij} = (\dot{\boldsymbol{x}}^i - \dot{\boldsymbol{x}}^j) + r^i(\boldsymbol{n}^{ij} \times \boldsymbol{\omega}^i) + r^j(\boldsymbol{n}^{ij} \times \boldsymbol{\omega}^j) \tag{4.7}$$

The contact velocity is further decomposed into normal ($\dot{\delta}_\mathrm{n}$) and tangential ($\dot{\boldsymbol{\delta}}_\mathrm{t}$) components. The magnitude of the tangential force is limited by the Coulomb-friction criterion of static and dynamic friction:

$$||\boldsymbol{f}_\mathrm{t}{}^{ij}|| \leq \begin{cases} \mu_\mathrm{s}||\boldsymbol{f}_\mathrm{n}{}^{ij}|| & \text{if } ||\dot{\boldsymbol{\delta}}_\mathrm{t}|| = 0 \\ \mu_\mathrm{d}||\boldsymbol{f}_\mathrm{n}{}^{ij}|| & \text{if } ||\dot{\boldsymbol{\delta}}_\mathrm{t}|| > 0 \end{cases} \tag{4.8}$$

where the static friction coefficient (μ_s) is larger or equal to the dynamic friction coefficient (μ_d). If the tangential force exceeds the static friction, the contact starts to slip along the contact plane. Strain-softening behavior at the contact can be introduced by having a lower dynamic than static friction coefficient value.

The macroscopic geotechnical behavior of the simulated particle assemblage is generally a result of the self-organizing complexity of the particles, but it is influenced by the micro-mechanical parameters. As demonstrated by Belheine et al. (2009), the normal and shear stiffnesses (k_n, k_t) effectively control Young's modulus and Poisson's ratio, which are macroscopic parameters. The friction coefficients (μ_s, μ_d) control the level of dilatancy during deformation, which in turn governs the shear strength.

Our DEM implementation is three-dimensional. This allows for particle rotation around arbitrary axes, which facilitates particle interlocking and gives a realistic three-dimensional geometry of the inter-particle voids. Two-dimensional DEM models tend to overfacilitate particle rolling (e.g. Morgan, 1999), since the rotational axes of particles are always parallel. The enhanced rolling in a 2D setup ultimately results in low material shear strengths.

The kinematic grain behavior is time-integrated in a fully explicit manner, resulting in a simple three-step algorithm:

1. Contact search (Eq. 4.5): Inter-particle and wall-particle contacts are identified.
2. Interaction (Eq. 4.6, 4.7, 4.8): For each particle contact, the contact forces and rotational moments are calculated.
3. Integration (Eq. 4.3, 4.4): Particle kinematics are updated using the sum of forces and torques, and time is increased by Δt.

For the temporal integration, a second-order half-step leapfrog Verlet integration scheme is used (Fraige and Langston, 2004; Kruggel-Emden et al., 2008). The length of the time step must be small enough to allow multiple updates of the kinematics, while the elastic wave travels through even the smallest particle in the assemblage. We therefore define the time step value on the basis of the natural undamped frequency ($\omega_0 = \sqrt{k_\mathrm{n}/m}$) in a linear spring system ($\Delta t_\mathrm{crit} = 2/\omega_0$) (O'Sullivan and Bray, 2004), which is a function of the elastic p-wave velocity (v_p):

$$\Delta t = f\sqrt{\frac{\min(m)}{\max(k_n, k_t)}} = f\,\frac{\min(r)\sqrt{\frac{28}{9}\mathrm{m}^{-1}\pi\min(r)}}{v_p} \tag{4.9}$$

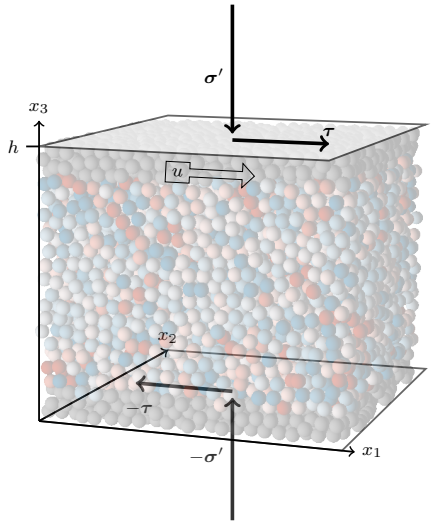

Figure 4.3. Model geometry in the numerical shear experiments. Grey particles have a fixed horizontal velocity; zero for the lower particles, and u for the upper particles. The resultant shear stress (τ) is a function of the time (t), the shear velocity (u), the effective normal stress (σ'), the material stiffnesses (k_n, k_t), and the coefficients of friction (μ_s, μ_d). The boundaries to the left, right, front, and back are periodic.

where $\min(m)$ is the smallest particle mass, and $\min(r)$ is the smallest particle radius. The constant f is introduced as a safety factor to account for the irregular contact network. It generally depends on the packing and the particle size distribution. In our experiments, a value of $f = 0.075$ was used (Zhang and Campbell, 1992).

To cope with the high computational requirements, the algorithm is formulated for graphics-processing unit (GPU) computation using the CUDA C API (Kirk and Hwu, 2010; NVIDIA, 2013b; NVIDIA, 2013a). The `sphere` DEM software is free and open source software, licensed under the GNU Public License v. 3[1]. The project is maintained at `https://github.com/anders-dc/sphere`.

Model configuration

We have adapted a model geometry where infinite shear strains can be obtained with periodic lateral boundaries (Figure 4.3). When a particle moves across a periodic boundary, it immediately re-enters through the opposite side. The particle contact search also works across these boundaries, so particle pairs can be in contact, although they are placed at opposite margins.

The particles are initially positioned randomly but without particles in physical contact. The particle assemblage is then gravitationally consolidated by running

[1] `https://gnu.org/licenses/gpl.html`

Table 4.1. Micromechanical properties and geometrical values for particles in the DEM shear experiment.

Parameter	Symbol	Value
Particle count	N_p	10000
Mean diameter	$2\bar{r}$	0.04 m
Std. deviation of diameter	σ	0.000187 m
Spatial domain dimensions	$\boldsymbol{L}$	$0.86 \times 0.86 \times 0.94$ m
Material density	ρ	2.6×10^3 kg m^{-3}
Normal stiffness	k_n	1.16×10^9 Nm^{-1}
Tangential stiffness	k_t	1.16×10^9 Nm^{-1}
Friction coefficient (static)	μ_s	0.3
Friction coefficient (dynamic)	μ_d	0.3
Normal stress range	σ_0	10 kPa to 120 kPa
Shear velocity	u	0.0369 ms^{-1}
Wall mass	m_w	6.42 kg
Time step length	Δt	6.33×10^{-7} s
Simulation length	t_total	20 s

the model through time, until the deficit potential energy, after temporarily being transformed to kinetic and rotational energy, is stored in the elastic components of the contacts, or is dissipated away by the frictional components of the system. Next, the particles are subjected to consolidation under a normal stress (σ_0), applied to the dynamic top wall. The particles are afterwards sheared at a constant velocity (u). The lowermost particles are fixed at their horizontal positions, while the uppermost particles are given a uniform, non-zero horizontal velocity. The fixed particles are defined to have a zero angular velocity. The shear stress (τ) and effective normal stress (σ') values are calculated as the sum of the force components acting on the upper fixed particles, along the axis of movement and normal to the top wall, respectively. The particle assemblage is free to dilate, as long as the upper stress boundary condition is satisfied. The numerical particles are indestructible, and the DEM experiments are therefore without grain crushing and abrasion.

The values of the physical and geometrical parameters are listed in Table 4.1. For simplicity, equal values are used for the normal and tangential stiffnesses, as well as for the static and dynamical coefficients of friction. The particle radii are drawn from a log-normal distribution.

The selected parameter values in the numerical experiments result in inertia parameter values (I, Eq. 4.1) between 7.5×10^{-4} and 2.2×10^{-4}. With these values, it is reasonable to assume that the material is deforming in a pseudo-static state without significant effects of particle inertia. The shearing velocity exceeds the deformation rate under glaciers by several orders of magnitude, but since the material deforms rate independently beneath $I = 10^{-3}$, the larger velocity only helps to minimize the computational time required.

4.4 Results

During the pre-shear consolidation phase, the numerical material compacts with exponentially decaying volumetric strain rates, which is typical for granular mate-

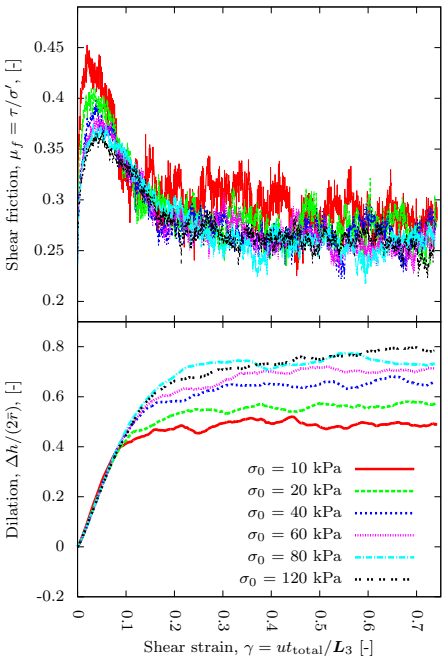

Figure 4.4. Shear friction (upper panel) and dilation (lower panel) as a function of shear strain, at different normal stress values in the DEM experiments.

rials (Nedderman, 1992). When sheared after consolidation, the numerical DEM material also behaves as a normally consolidated granular material, with clearly distinguishable peak and ultimate shear strength values (Figure 4.4). The peak and ultimate shear friction values depend on the level of normal stress. A high level of normal stress requires larger shear strains before the ultimate shear strength is reached. Furthermore, the magnitude of the total dilation increases with the magnitude of the normal stress.

The Mohr-Coulomb relationship (Eq. 4.2) is fitted to the shear stress data using a nonlinear least-squares Marquardt-Levenberg algorithm. The regressed coefficients and their asymptotic standard error values are $\phi_p = 32° \pm 0.31°$, $C_p = 1.2 \pm 0.21$ kPa in the peak failure state, and $\phi_u = 22° \pm 0.47°$ and $C_u = 0.51 \pm 0.31$ kPa in the critical failure state. The linear correlation confirms that the material deforms according to the Mohr-Coulomb theory. The measured values of the macromechanical angle of internal friction are within the range found in other tests involving real materials, ranging from 17° for smooth spherical particles to about 56° for angular particles (Nedderman, 1992).

Within the modelled material, stress is distributed heterogeneously along a complex network of force chains (Figure 4.5 and 4.6). Particles in a force chain are often subjected to stress magnitudes more than four times the macroscopic confining stress (Figure 4.5). The force chains are generally aligned with the direction of maximum compressive stress, resulting from the combined influence of the overburden normal stress and the shear movement (Figure 4.7). Therefore,

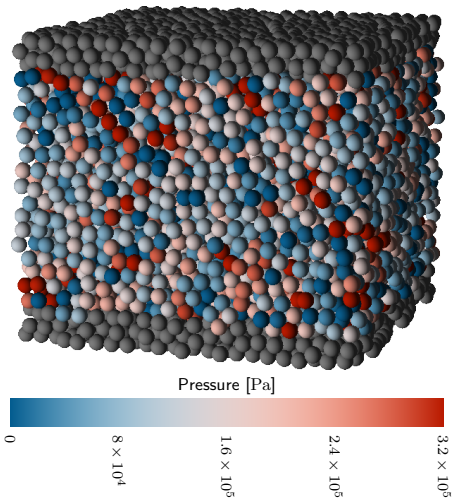

Figure 4.5. Visualization of the dispersive pressures of the heterogeneous stress network in the simulated material with $\sigma_0 = 80$ kPa.

force chains are predominantly vertical during consolidation and subhorizontal during shear. In the latter situation with shear, the force chain network is rapidly reconfiguring, even faster than the grain reorganization[2].

In the absence of friction from the sides, the shear zone develops near the top boundary since this configuration requires a minimum of material to be accelerated. Furthermore, the material strengthens with depth because the weight of the overburden material increases the normal stress and the shear strength of particle contacts (Eq. 4.8).

The numerical experiments demonstrate how the vertical particle displacement profiles depend on the applied normal stress (Figure 4.8). In the simulations with low normal stress, a shear band develops at the top boundary, and particle velocities decrease with depth. Due to the absence of a strong inter-particle cohesion, the deformation accumulates in shear bands of variable thickness instead of along sharp planes of failure (e.g. Tchalenko, 1970). The shear zone thickness is equivalent to approximately seven mean particle diameters. For higher levels of normal stress, the deformation profile is deeper and the shear zone thicker. The internal porosity values (Figure 4.9) are strongly connected to the corresponding deformation profile (Figure 4.8), since shear strain in normally consolidated materials increases the porosity in the absence of particle crushing. Overall, the experiments with the lowest normal stress values have the highest porosity values in the upper zone of the material, which is a consequence of the shallow band of active deformation. The experiments with high normal stress values show a deeper increase of porosity, owing to the increased shear zone thickness. The shear zone itself displays a complex system of self-organized particle mechanics in highly transient patterns (Figure 4.10). The particle contact stresses result in rolling or inter-particle slip,

[2]A supplementary animation is available at: `http://users-cs.au.dk/adc/files/shear-80kPa-pressures.mp4` (29 MB)

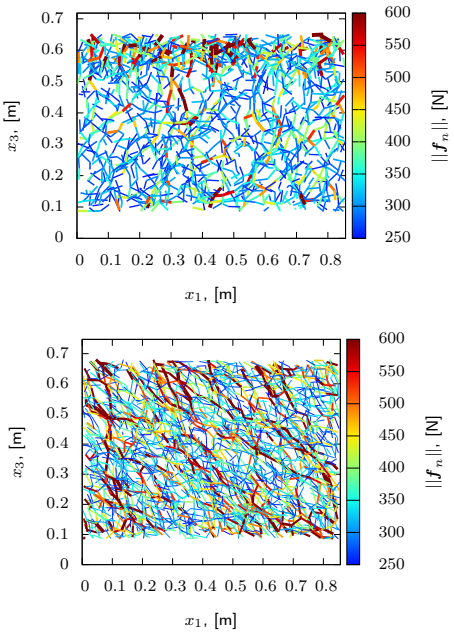

Figure 4.6. Force distribution in the non-fixed particles during consolidation (upper panel) and during shear (lower panel). $\sigma_0 =$ 80 kPa in both cases. The width and color of the line segments are determined by the magnitude of the contact normal force ($||\boldsymbol{f}_n||$). The shear movement in the lower plot takes place along the top boundary towards the right. Several of the contacts forces are greatly exceeding the upper limit of the color bar.

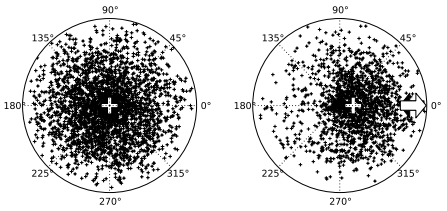

Figure 4.7. Trend and plunge of the 50% strongest DEM inter-particle normal forces ($\boldsymbol{f}_n$) during consolidation (left) and during shear (right). $\sigma_0 = 80$ kPa in both cases. The plots are equal-angle stereographic projections on the lower-hemisphere, with the stereonet equator situated in the horizontal (x_1,x_2)-plane. The white plus symbols denote the trend and plunge of the maximum compressive stress ($\boldsymbol{\sigma}' + \boldsymbol{\tau}$). The arrows in the right plot denote the shearing direction.

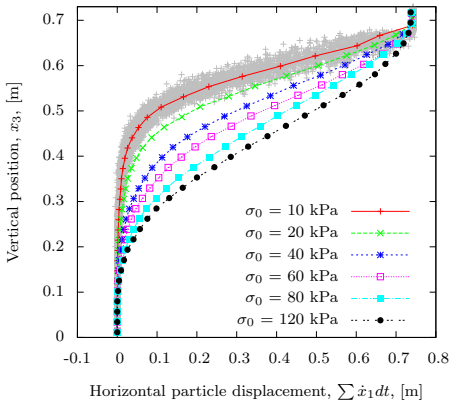

Figure 4.8. Laterally averaged strain-depth profiles at the end of the numerical DEM experiments with varying levels of overburden normal stress. The individual particle values for the $\sigma_0 = 10$ kPa experiment are underlain to visualize the horizontal variance of the displacement. The total shear distance is 0.738 m.

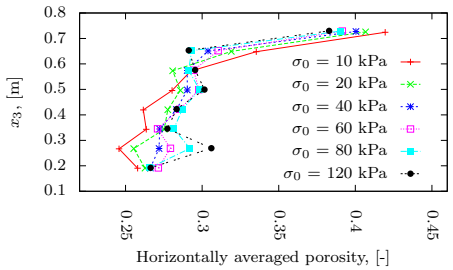

Figure 4.9. Porosity values of horizontally integrated slabs at the final time step in the numerical experiments.

depending on which kinematic response requires the minimal amount of activation energy.

4.5 Discussion

Force chains

Granular materials are by definition heterogeneous, and the force network providing the stability of the system is non-uniform (Jaeger et al., 1996). The force network is represented by the force chains that transmit stress through grain bridges or arches. Previous investigations have established that the mesh size of the force network has a characteristic size, about ten times larger than the grain diameter, although sensitive to grain size variance (Clement, 1999). It is likely that this length scale of the force network also defines the minimum thickness of shear zones.

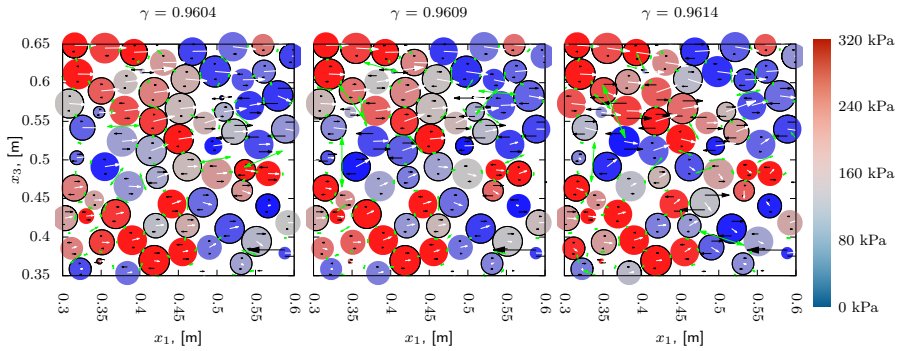

Figure 4.10. Particle kinematics inside the shear zone at three stages during the DEM experiment with $\sigma_0 = 80$ kPa. The particles are visualized as discs according to the intersection with the center (x_1,x_3)-plane. The particle color corresponds to the contact pressure, rotational velocities are indicated using black arrows, linear velocities with white arrows, and inter-particle slip velocities are shown with green arrows starting at the contact centre. Particles spinning positively around the second axis are marked with a black border. It should be noted that with this type of planar visualization the porosity appears larger than the true value, and the spherical particles may be in physical contact although they appear not to be here. A supplementary animation is available at `http://users-cs.au.dk/adc/files/shear-80kPa-plane.mp4` (53 MB).

Our numerical experiments demonstrate that the force chains carry stress of high magnitude. Although particle breakage is not part of the modelling method, the DEM simulations hence support the hypothesis that force chains are effective mechanisms of grain crushing, even distant from the rapidly deforming shear zones. Yet, grain size modification due to particle abrasion is likely favored inside the shear zone, where the relative movement between particles is greatest. Grain bridges in till are mainly aligned oblique to the shear direction, and are often associated with crushed grains (Hooke and Iverson, 1995; Iverson et al., 1996; Larsen et al., 2007). Hooke and Iverson (1995) and Iverson et al. (1996) showed that failure of grains in force chain networks during shear significantly modifies the particle sizes, leading to a self-similar, fractal grain size distribution. As the grain sizes decrease, the finer components become more active in distributing stresses through the system. Since the mesh spacing in the stress network is a function of the typical grain size, the force chain distance decreases, and the stress network becomes more homogeneous with less stress fluctuation (Iverson et al., 1996; Morgan, 1999; Iverson, 2010).

The failure of force chains in a subglacial bed can be caused by particle crushing, particle rotation, inter-particle sliding or a change in the stress field, for instance induced by changes in subglacial hydrology. If the bed fails to establish a new force chain, exerting flow-resistant friction to the glacier base, the force chain failure can result in a propagating instability, possibly resulting in a glacial slip

event. Clearly, the description of slip initiation and failure propagation in stress-limited systems requires more attention in future studies. A numerical DEM model, perhaps extended by angular particles for increased particle interlocking, is ideal for such studies, since it allows for a detailed quantification of the internal sediment mechanics at seismic time scales.

Variability of the vertical strain distribution

Our DEM simulations demonstrate a clear relationship between the applied normal stress and the depth of deformation (Figure 4.8). This result can be explained by considering the frictional strength of particle contacts. According to Mohr-Coulomb theory, the frictional strength of particle contacts depends on pressure, and force chain stability is therefore strengthened by high levels of normal stress. The strong force chains transmit stress over large distances, causing weak contact planes at greater depths to fail and the thickness of the deforming zone to increase.

In situ measurements of subglacial water pressure (e.g. Engelhardt et al., 1990; Murray and Clarke, 1995; Hooke et al., 1997; Engelhardt and Kamb, 1997; Hart et al., 2009; Bartholomaus et al., 2011), and sedimentary indications of palaeo-subglacial conditions (Piotrowski and Tulaczyk, 1999; Boyce and Eyles, 2000; Larsen et al., 2004; Piotrowski et al., 2001; Piotrowski et al., 2006), show that the magnitude of the porewater pressure often lies close to the ice overburden pressure, modulated by diurnal and seasonal variations. In such cases, our numerical results suggest a deformation profile of convex shape (Figure 4.8). The subglacial transport rate of a warm-based glacier with a well-developed drainage system, resting on a granular bed, thus seems to be controlled by the value of the normal stress, the effective diameter of the granular material, and the basal velocity. The granular frictional mechanisms included here are, however, not sufficient to explain very thick deformation profiles, which may be due to thermal effects, ice-bed interface (IBI) roughness, varying lithology, or hydrological feedbacks such as dilative hardening (e.g. Iverson et al., 1998; Evans et al., 2006; Kjær et al., 2006; Rathbun et al., 2013). However, the DEM results confirm that convex-upward displacement profiles are possible in Mohr-Coulomb granular materials, as also demonstrated by Tulaczyk et al. (2000a) and Iverson and Iverson (2001).

Dynamics of dilation and porosity

As a consequence of the relative movement of grains, normally consolidated granular materials initialy dilates during shear (Reynolds, 1885). The dilation stops when a critical stage is reached. Our numerical DEM setup behaves similarly. Furthermore, shifting configurations of the force chains cause frequent fluctuations of the DEM model thickness, although these are bound to decrease with increasing number of particles (Iverson et al., 1996; Morgan, 1999; Li and Aydin, 2010).

The implications of volumetric changes during shear band formation depend on the influence and properties of pore fluid flow. Importantly, the pore fluid can have two opposite effects, depending on the degree of grain crushing in the shear zone. Without significant grain crushing, the shear zone dilates under deformation. If the strain rate is sufficiently high, relative to the hydraulic permeability of the material, deformation decreases the local porewater pressure, which in turn increases the effective pressure. This increase in normal stress strengthens the material (Eq. 4.2) and causes dilatant hardening (Iverson et al., 1998). Such hard-

ening effects may drive migration of the shear zone. In contrast, shear zones may contract if grain crushing allows for repacking of the gains (Wafid et al., 2004; Iverson et al., 2010). This contraction lowers the shear strength because of the porewater pressure increases (Eq. 4.2). Furthermore, the fine-grained products of widespread grain crushing may accelerate this effect by decreasing the hydraulic conductivity and lowering the excess porewater pressure dissipation rate (Okada et al., 2004; Iverson et al., 2010). The effect of such strain induced softening is to stabilize the active shear zones.

In the absence of grain crushing and pore fluid transport, the DEM experiments indicate that the decrease of hydraulic pressure internally in the shear zone is a function of normal stress (Figure 4.9). A low level of normal stress results in the formation of a narrow shear zone with a highly reduced hydraulic pressure, whereas higher levels of normal stress result in a smaller pressure decrease. Still, the total deficit of hydraulic pressure is greater under high normal stresss because it affects a much thicker zone (Figure 4.4, bottom). The effects of dilatant hardening are thus expected to be stronger under higher normal stresses.

Our future numerical studies will focus on the mechanical interaction with a simulated pore fluid, by incorporating a full two-way coupling between pore fluid flow and the granular skeleton. This coupled methodology will allow small-scale investigations of the two-way interaction of moving grains and the inter-particle fluid, even with complex geometries of the upper, moving boundary, such as during ploughing (Tulaczyk et al., 2001; Thomason and Iverson, 2008). As highlighted by Iverson et al. (1998), the rheology of a grain-fluid mixture is likely to contain viscous components if the characteristic time scale for the diffusion of hydraulic pressures is smaller than the characteristic time scale for dilation.

Particle rotation

The particles in the numerical setup can have both translational and rotational movement components. Angular accelerations, velocities, and positions are handled as quaternions (three-dimensional rotation), whereby the direction of the quaternion denotes the rotational axis, and the quaternion length relates to the rotation magnitude. The rotation follows the right-hand rule, implying that a particle with an angular velocity of $\boldsymbol{\omega} = \{0, 1, 0\}$ rad s^{-1} represents a rotation around the second axis, where the upper tangential velocity points in the positive direction of the first axis.

Unidirectional rolling is assumed to dominate particle transport in the conceptual model of Meer (1997). However, our DEM experiments demonstrate that particles in contact prefer to roll in opposite directions in order to avoid large contact slips (Figure 4.10). Since the tangential contact strength is scaled by the magnitude of the normal force (Eq. 4.8), contacts between grains situated in a force chain are mechanically strong. For this reason, grains in force chains prefer to roll in opposite direction in order to avoid slips, while slip on contacts in the adjacent, low pressure areas are more frequent. During the small range of shear strain increments displayed in Figure 4.10, the stress-bearing force network is slightly relocated, and several grains change rotational direction. This shows how the micromechanical system to a large extent reconfigures itself through a relatively small range of shear strain values. Yet, it should be noted that the spheres of the numerical experiment likely favor rotation instead of slip, due to the absence of interlocking caused by grain angularity and elongation.

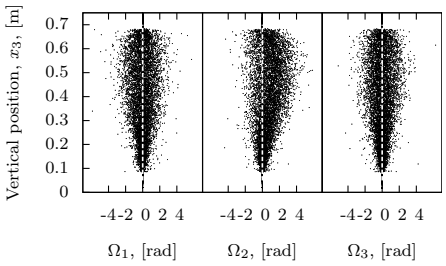

Figure 4.11. Scatter plots of the particle rotation, decomposed along each Euclidean axis. The results shown are from the last time step of the numerical DEM experiment with $\sigma_0 = 80$ kPa.

The angular position can for each particle be calculated by integrating the rotational velocity, i.e. $\mathbf{\Omega}^i = \int_0^t \boldsymbol{\omega}^i dt$. For the experiment with $\sigma_0 = 80$ kPa, the estimated mean values of the total rotation per Euclidean axis are $\hat{\mu}(\mathbf{\Omega}) = \{-0.0027, 0.50, -0.0053\}$ rad s^{-1}, with empirical variances of $s^2(\mathbf{\Omega}) = \{0.76, 1.1, 0.68\}$ (Figure 4.11). These results illustrate that the mean direction of the rotational axes has a strain signature, and that this trend in rotational direction is already developed at a shear strain of $\gamma = 1$. The relatively large variance values indicate, however, that rotational microstructures are to be expected in any orientation. The direction of shear strain can thus theoretically be deduced only from a very large dataset of rotational axis orientations. Rotational structures are often very abundant in tills (e.g. Meer, 1993; Menzies, 2000; Hiemstra and Rijsdijk, 2003) and they have been identified in thin sections both parallel and perpendicular to the shear stress direction, suggesting that they may form in various stress regimes and with an inherent variability in the orientation of the rotational axes.

Comparison to laboratory ring-shear experiments

Ring-shear machines have previously been used to investigate the mechanical behavior of till (e.g. Iverson et al., 1996; Iverson et al., 1997a; Iverson et al., 1998; Tulaczyk et al., 2000a; Müller and Schlüchter, 2000; Moore and Iverson, 2002), and the development of strain signatures (e.g. Iverson et al., 1996; Iverson et al., 1997a; Hooyer and Iverson, 2000b; Hooyer and Iverson, 2000a; Müller and Schlüchter, 2000; Thomason and Iverson, 2006; Larsen et al., 2006; Iverson et al., 2008). Here, stress measurements from ring-shear experiments are compared to the simulated DEM granular behavior. Our ring-shear apparatus (Figure 4.12, see also Larsen et al. (2006) and Bateman et al. (2012)) has a sample chamber volume of 14480 cm^3, a chamber width of 12.0 cm, and a chamber height of 8.0 cm. The centerline diameter is 54.0 cm. The upper platen is rotationally fixed, while the lower platen is moved at a constant velocity ($u = 1.67 \times 10^{-5}$ m s^{-1} = 1.0 mm min^{-1}). To quantify the distribution of strain, we inserted coarse (2–4 mm), angular quartz and feldspar grains as strain markers.

The geometry of the numerical setup (Figure 4.3) and the ring-shear apparatus (Figure 4.12) both allow infinite shear strains, owing to the absence of boundaries in the shear direction. On the other hand, factors that are likely to produce sig-

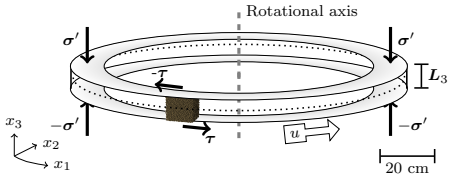

Figure 4.12. Geometry of the laboratory ring-shear apparatus sample chamber, which is filled with sediment during the shear tests. The dotted line marks the shearing gap in the side walls between the stationary upper loading platen and the lower mobile part.

Table 4.2. Fitted values of the Mohr-Coulomb relationship (eq. 2ultimate (u) failure stages of the materials.

Material	ϕ_p [°]	C_p [kPa]	ϕ_u [°]	C_u [kPa]
Quartz sand	45	3.7	44	2.4
Glass beads	37	1.8	35	1.5
DEM	32	1.2	22	0.51
Till	18	3.1	18	0.69

nificant differences between laboratory and numerical experiments are associated with side wall friction in the ring-shear sample chamber, the elastic response and acceleration of the mechanical parts in the ring-shear apparatus, and the difference in particle numbers.

In order to provide a wide framework for comparison, we performed laboratory experiments with several types of materials. The first material consisted of spherical glass beads with a mean grain size of approximately 4.0×10^{-4} m (best fitted with a log-normal distribution with $\mu = -5.5$ and $\sigma = 0.21$). The second material used was an industrially sorted, angular to subangular, aeolian quartz sand, also with a mean grain size of approximately 4.0×10^{-4} m (best log-normal fit with $\mu = -5.5$ and $\sigma = 0.26$). The experiments on these materials were performed under dry conditions. Also used for the comparison study was a previous Mohr-Coulomb failure analysis on a Weichselian-age basal till from the Scandinavian Ice Sheet (SU3 in Tylmann et al., 2013), performed in the same ring-shear apparatus. The till was sheared under water-saturated conditions with a hydrological connection through filters in the chamber top and bottom to atmospheric pressure. The till was poorly sorted with a bimodal grain size distribution with peaks in the sand and silt fractions.

We use the laboratory results to compare the simulated DEM granular behavior with that real materials under similar conditions. Due to the side wall friction, the magnitude of the material shear strength is likely to be higher in the laboratory materials. We can, however, compare the stress-strain dynamics observed by the two methods (Figure 4.13) and attempt to explain the differences in the material behavior (Figure 4.14, Table 4.2), bearing in mind the aforementioned caveats.

The shearing of a granular material from a pre-failure, normal consolidated state can be subdivided into multiple stages (cf. Li and Aydin, 2010), which we

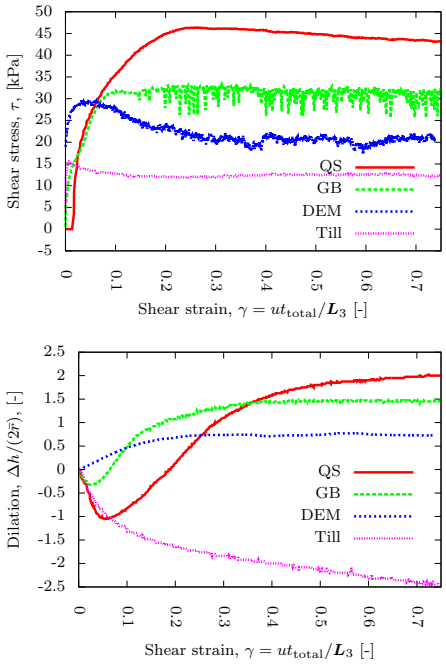

Figure 4.13. Shear stress (upper panel) and dilation (lower panel) as a function of shear strain, recorded during the laboratory shear tests on quartz sand (QS), glass beads (GB), till, and the numerical discrete element method material DEM. The normal stress is $\sigma_0 = 80$ kPa for all tests, except for the till, where $\sigma_0 = 85$ kPa. The till shear stress values are scaled to account for the differences in normal stress.

recognise in both the laboratory and the numerical setting:
Stage-1: The initial shearing motion results in contraction, caused by the combined effect of increased elastic deformation, and reorganization of the grains. Both effects are caused by the increased magnitude and reorientation of the maximum compressive stress ($\boldsymbol{\sigma'} + \boldsymbol{\tau}$). The increase in maximum compressive stress promotes consolidation, and decreases porosity (Nedderman, 1992; Tulaczyk et al., 2000a). The elastic response is increased if the grains are angular, which can stabilize the inter-grain contacts mechanically (Nedderman, 1992; Weatherley et al., 2012). The numerical DEM material does not exhibit contraction during stage-1 shear, since particles are spherical and for this reason cannot develop interlocking. The glass beads and the quartz sand both display a transient contraction during this stage. Owing to the angularity of grains, the quartz sand displays the strongest contraction and the longest duration of this stage.
Stage-2: The material dilates due to relative particle movement (Reynolds, 1885; Mead, 1925), and exhibits its peak shear strength value (τ_p). The shear zone evolves into a high-porosity layer (Gennes, 1999). The numerical material, the glass beads, and the quartz sand dilate during this stage. The numerical material dilates to approximately 0.75 grain diameters, the glass beads dilate to 1.5 grain

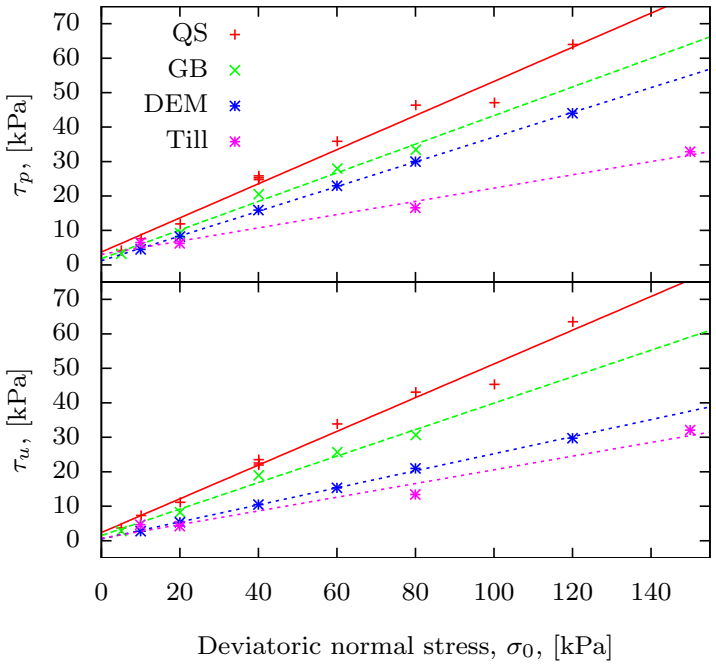

Figure 4.14. Mohr-Coulomb failure analysis of three laboratory granular materials and one numerical material. Equation 2 was fitted to the $(\sigma_0, \tau_{p,u})$-data sets using the nonlinear least-squares Marquardt-Levenberg algorithm. Upper: Peak shear strength values (τ_p). Lower: Ultimate shear strength values (τ_u).

diameters, the quartz sand to 2.0 grain diameters. The till continues to contract. This contraction is caused by the volumetric decrease due to micro and macro fabric development, and subsequent diffusion of the increased internal hydraulic pressures. In addition to this, a small volume of till was after the experiments observed to having been squeezed out of the sample chamber.
Stage-3: In the final stage, the shear zone becomes fully developed, as the material reaches the critical state. The shear strength decreases to the ultimate value (τ_u) and dilation stops (Schofield and Wroth, 1968). This behavior is observed in the numerical material, the quartz sand, and the till. The materials display no low-frequency volumetric and shear strength changes, only high-frequency fluctuations caused by fracturing of the grains or reorganization of the internal force-bearing network (Iverson et al., 1996; Li and Aydin, 2010). As observed in similar experiments (Mair et al., 2002), the glass beads show stick-slip behavior at this stage, owing to elasticity of the apparatus. No measurable products of grain crushing are detected, which rules out fracturing of grains as the cause of the fluctuations.

Particle shape and angularity

Comparing the stress-strain relationships of the DEM and the laboratory materials highlights the importance of grain shape and angularity for the macroscopical

geotechnical behavior. The initial elastic response, the peak shear strength, and the total dilation are all higher in the materials with angular grains, such as the quartz sand. The spherical materials, such as the glass beads and the numerical DEM particles, are mechanically weaker, and show lower values of dilation. For a normal stress of 80 kPa, the shear zone is approximately 4 mm thick in the glass beads and 6 mm thick in the quartz sand. As demonstrated by Mueth et al. (2000), spherical and smooth particles generally exhibit deformation in narrow shear bands. The shear strength of materials tends to increase with grain angularity (e.g. Mair et al., 2002; Anthony and Marone, 2005; Azéma et al., 2012). The shear strength also tends to increase with grain elongation (Azéma and Radjaï, 2010), which is a prerequisite for fabric development (Hooyer and Iverson, 2000b; Mair et al., 2002; Thomason and Iverson, 2006). Therefore, the simplified grain shape in the DEM relative to real materials evidently influences the levels of stress and dilation. Still, the Mohr-Coulomb model is equally valid for the numerical and laboratory materials.

Future studies will focus on expanding the numerical method to simulate inter-particle bonds (Potyondy and Cundall, 2004; Wang et al., 2006; Wang, 2009; Obermayr et al., 2013). With particle bonds, it is possible to include irregularly shaped, breakable aggregates of bonded spheres. By simulating angular particle clusters instead of loose spheres, the initial, low-strain elastic response during stage-1 shear may be improved due to greater inter-locking of particles inside force chains, which is likely to increase the material shear strength. The bond functionality will also enable studies of fabric development and modifications of grain size distribution during progressive shear.

Particle size distribution and mineralogy

In comparison to the DEM, the laboratory materials contain a wider range of particle sizes. Morgan and Boettcher (1999) showed that in two-dimensional shear experiments with a variety of grain size distributions, the presence of fine particles caused strain localization, which is consistent with the theory of the shear zone thickness being a function of the grain size (Gennes, 1999; Herrmann, 2001). Mair et al. (2002) demonstrated no significant shear strength differences between narrow and wide grain size distributions of spherical glass beads, whereas Morgan (1999) reported a slight shear strength decrease with the volumetric increase of fine, but micromechanically identical particles.

Clay minerals are known to behave different than coarser granulates, and a high clay content may therefore influence the macromechanical material behavior significantly (Iverson et al., 1997a). Often, shear zones in clay are more narrow due to the smaller grain size, and cohesion causes clays to deform by both folding, faulting, and fracturing (Eisenstadt and Sims, 2005). Clay particles interact not only with mechanical repulsion upon contact, but with a variety of physico-chemical interactions causing repulsion and attraction at different spatial configurations. Yao and Anandarajah (2003) introduced a methodology for simulating clay minerals in DEM models, which will serve as a basis for future quantification of the role of clays in glacial diamicts.

4.6 Conclusions

The discrete element method, although parameterized by micromechanical properties, is useful for modeling the macroscopic mechanical properties of simple granular materials, sheared under dry conditions. The concept of a numerical DEM model may complement analog experiments, since it allows a detailed investigation of the microphysics. The DEM displays dilation during deformation and self-organizing particle kinematics. Both effects are difficult to capture in conventional numerical models based on continuum mechanics. From numerical shear experiments, we show how relatively high values of normal overburden stress result in deep, distributed profiles of deformation and a thick zone of increased porosity. A lower overburden stress results in relatively narrow boundary layers of deformation that are characterized by high porosity. Our DEM experiments demonstrate how stress in a granular material is heterogeneously distributed along force-bearing particle chains. The force chains are transient in nature, but the mean orientation of the load-bearing contacts is clearly governed by the direction of the maximum compressive stress. We suggest that the transient stability of the force chains represents an important aspect of subglacial sediment deformation. Particle rotational axes tend to align with progressive shear, although closer examination shows that particles in contact often rotate in opposite directions in order to avoid slip along the inter-particle contact interfaces.

Acknowledgments

We thank the laboratory staff at the Department of Geoscience, Aarhus University for performing grain size analyses and assisting during the laboratory experiments. We thank Neal Iverson, Jason Thomason and an anonymous reviewer for constructive reviews, which improved the quality of the manuscript. This research was funded by the Danish Council for Independent Research under the Sapere Aude programme. S. Tulaczyk's involvement in this research was supported by NSF-ANT-0839142, and K. Tylmann was funded by NSC grant no. 2011/01/N/ST/10/05880.

Chapter 5

Paper 2: *A new methodology to simulate subglacial deformation of water saturated granular material*

Anders Damsgaard[1], David L. Egholm[1], Jan A. Piotrowski[1], Slawek Tulaczyk[2], Nicolaj K. Larsen[1], and Christian F. Brædstrup[1]

1. Department of Geoscience, Aarhus University, Aarhus C, Denmark.
2. Department of Earth and Planetary Sciences, University of California, Santa Cruz, California, USA.

Submitted to *The Cryosphere*.

Abstract

The dynamics of glaciers are to a large degree governed by processes operating at the ice-bed interface (IBI), and one of the primary mechanisms of glacier flow over soft unconsolidated sediments is subglacial deformation. However, it has proven difficult to constrain the mechanical response of subglacial sediment to the shear stress of an overriding glacier. In this study, we present a new methodology designed to simulate subglacial deformation using a coupled numerical model for computational experiments on grain-fluid mixtures. The granular phase is simulated on a per-grain basis by the discrete element method. The pore water is modeled as a compressible Newtonian fluid without inertia. The numerical approach allows close monitoring of the internal behavior under a range of conditions.

The rheology of a water-saturated granular bed may include both plastic and rate-dependent dilatant hardening or weakening components, depending on the rate of deformation, the material state, clay mineral content, and the hydrological properties of the material. The influence of the fluid phase is negligible when relatively permeable sediment is deformed. However, by reducing the local permeability, fast deformation can cause variations in the pore-fluid pressure. The pressure variations weaken or strengthen the granular phase, and in turn influence the distribution of shear strain with depth. In permeable sediments the strain distribution is governed by the grain-size distribution and effective normal stress and is typically on the order of tens of centimeters. Significant dilatant strengthening in impermeable sediments causes deformation to focus at the hydrologically more stable ice-bed interface, and results in a very shallow cm-to-mm deformational depth. The amount of strengthening felt by the glacier depends on the hydraulic conductivity at the ice-bed interface. Grain-fluid feedbacks can cause complex material properties that vary over time, and which may be of importance for glacier stick-slip behavior.

5.1 Introduction

The coupled mechanical response of ice, water and sediment can control the flow of glaciers residing on deformable sediment (e.g. Alley et al., 1987b; Bindschadler et al., 2001; Clarke, 2005; Bougamont et al., 2011; Turrin et al., 2014). This is clearly expressed by ice streams in Greenland and Antarctica, where low levels of basal friction enable high flow rates. These ice streams are of particular interest, since they are large constituents of the polar ice sheet mass balance (e.g. Rignot and Thomas, 2002).

Although the majority of flow-limiting friction of ice streams terminating into ice shelves is likely provided by ice shelf buttressing (De Angelis and Skvarca, 2003; Rignot et al., 2004; Dupont and Alley, 2005), the disintegration of these ice shelves leaves lateral (Whillans and Veen, 1997; Tulaczyk et al., 2000b; Price et al., 2002) and basal friction (Alley, 1993; MacAyeal et al., 1995; Stokes et al., 2007; Sergienko and Hindmarsh, 2013) as the main mechanical components resisting the flow. A fundamental understanding of subglacial dynamics is a requirement for our ability to predict future response of the ice sheets to climate change.

The pressure and flow of pore water in the subglacial bed can influence subglacial deformation in a number of ways. Assuming a Mohr-Coulomb constitutive relation of the basal till strength, an increase in pore water pressure weakens the bed by reducing the effective stress, and this may facilitate basal movement if the driving shear stresses become sufficient to overcome the sediment yield strength

(Kamb, 1991; Iverson et al., 1998; Tulaczyk et al., 2000a; Fischer and Clarke, 2001; Kavanaugh and Clarke, 2006).

If the hydraulic diffusivity of the bed is sufficiently low relative to the deformational velocity, a modulation of the pore-water pressure at the ice-bed interface is over time carried into the subglacial bed, resulting in variable internal yield strength and ultimately variable shear strain rates with depth (Tulaczyk, 1999; Tulaczyk et al., 2000a; Kavanaugh and Clarke, 2006). Owing to local volumetric changes, variations from the hydrostatic fluid pressure distribution can be created inside the sediment by the onset and halt of granular deformation. This influences the local effective pressure and, in turn, the sediment yield strength (e.g. Iverson et al., 1998).

In the case of non-planar ice-bed geometry excess pore-water pressures can develop on the stoss side of objects ploughing through a subglacial bed (Iverson et al., 1994; Iverson, 1999; Thomason and Iverson, 2008). The elevated pore-water pressure weakens the sediment by lowering the effective stress, resulting in a net strain-rate weakening rheology (e.g. Iverson et al., 1998; Fischer et al., 2001; Clark et al., 2003; Iverson, 2010), which has been associated with the stick-slip behavior of Whillans Ice Stream (Winberry et al., 2009).

Early field studies suggested a strain-rate strengthening Bingham or slightly non-linear viscous rheology of till (Boulton and Hindmarsh, 1987), which has been used to simplify analytical and numerical modeling of till mechanics (e.g. Alley et al., 1987b; Hindmarsh, 1998; Fowler, 2000). Laboratory studies have, however, favored the notion of till having a plastic, Mohr-Coulomb rheology, with a very small rate-dependence in the case of a critical state deformation (Kamb, 1991; Iverson et al., 1998; Tulaczyk et al., 2000a; Rathbun et al., 2008). This Mohr-Coulomb rheology is also supported by field investigations (Truffer et al., 2000; Kavanaugh and Clarke, 2006). On the other hand, a rate-weakening rheology is expected in the case where obstacles plough through a soft and deformable bed (Iverson et al., 1994; Iverson, 1999).

Both viscous and plastic rheologies are expected end-members of particle-fluid mixtures, dependent on the deformational rate, fluid viscosity, fluid-solid volumetric fraction and confining stresses. The low viscosity of water does, however, make it easy to deform even under high strain rates and can only be expected to influence the overall rheology of subglacial materials in a few select scenarios (e.g. Iverson, 2010). The mechanics of coupled granular–fluid mixtures have previously been numerically investigated for studies of fluidized beds (e.g. Anderson and Jackson, 1967; Gidaspow et al., 1992; Hoomans et al., 1996; Xu and Yu, 1997; McNamara et al., 2000; Feng and Yu, 2004; Jajcevic et al., 2013), the stability of inclined, fluid-immersed granular materials (e.g. Topin et al., 2011; Mutabaruka et al., 2014), mechanics during confined deformation (e.g. Goren et al., 2011; Catalano et al., 2014), debris flow (e.g. Hutter et al., 1994; Mangeney et al., 2007; Goren et al., 2011) and for the design of industrial components, e.g. hydrocyclones (e.g. Wang et al., 2007; Zhou et al., 2010), or silos and hoppers (Kloss et al., 2012).

This study explores the interaction between the fluid and granular phases in water-saturated consolidated particle assemblages undergoing slow shear deformation. A dry granular assemblage deforms rate-independently in a pseudo-static manner when deformational rates are sufficiently low (GDR-MiDi, 2004; Damsgaard et al., 2013). The particle-fluid mixture is in this study sheared with velocities and stresses comparable to those found in subglacial settings. The computational approach allows for investigating the internal granular mechanics and

feedbacks during progressive shear deformation.

In the following section, we present the details of the numerical implementation of particle-fluid flow, and describe the experimental setup. We then present and discuss the modeled deformational properties of the particle-fluid mixture. Finally, we analyze how the fluid influences formation of shear zones and under which conditions deformation is rate dependent.

5.2 Methods

The granular model

We use the discrete element method (DEM) (Cundall and Strack, 1979) to simulate the granular deformation. With the DEM, particles are treated as separate, cohesion-less entities, which interact by soft-body deformation defined by a prescribed contact law. The contact mechanics are micro-mechanically parameterized. The temporal evolution is handled by integration of the momentum equations of translation,

$$m^i \frac{\partial^2 \boldsymbol{x}^i}{\partial t^2} = \underbrace{m^i \boldsymbol{g}}_{\text{Gravity}} + \overbrace{\sum_j \left(\boldsymbol{f}_{\mathrm{n}}{}^{ij} + \boldsymbol{f}_{\mathrm{t}}{}^{ij} \right)}^{\text{Contact forces}} + \boldsymbol{f}_{\mathrm{i}}{}^{i} \tag{5.1}$$

and rotation:

$$I^i \frac{\partial^2 \boldsymbol{\Omega}^i}{\partial t^2} = \underbrace{\sum_j \left(-\left(r^i + \frac{\delta_{\mathrm{n}}{}^{ij}}{2} \right) \boldsymbol{n}^{ij} \times \boldsymbol{f}_{\mathrm{t}}^{ij} \right)}_{\text{Contact torques}} \tag{5.2}$$

i and j are particle indexes, m is the particle mass, I is the particle rotational inertia, $\boldsymbol{x}$ and $\boldsymbol{\Omega}$ are linear and rotational particle positions, respectively. $\boldsymbol{f}_{\mathrm{n}}$ and $\boldsymbol{f}_{\mathrm{t}}$ are the interparticle contact force vectors in the normal and tangential direction relative to the contact interface, and $\boldsymbol{f}_{\mathrm{i}}$ is the fluid-particle interaction force (Fig. 5.1). $\boldsymbol{n}$ is the inter-particle normal vector, and δ_{n} is the inter-particle overlap distance at the contact.

The inter-particle contact forces are determined by a linear-elastic contact model. The magnitude of the tangential force $\boldsymbol{f}_{\mathrm{t}}$ is limited by the Coulomb frictional coefficient μ (Cundall and Strack, 1979; Luding, 2008; Radjaï and Dubois, 2011; Damsgaard et al., 2013):

$$\boldsymbol{f}_{\mathrm{n}}^{ij} = -k_{\mathrm{n}} \delta_{\mathrm{n}}^{ij} \boldsymbol{n}^{ij} \quad \text{and} \quad \boldsymbol{f}_{\mathrm{t}}^{ij} = -\max\left\{ k_{\mathrm{t}} ||\boldsymbol{\delta}_{\mathrm{t}}^{ij}||, \mu ||\boldsymbol{f}_{\mathrm{n}}^{ij}|| \right\} \frac{\boldsymbol{\delta}_{\mathrm{t}}^{ij}}{||\boldsymbol{\delta}_{\mathrm{t}}^{ij}||} \tag{5.3}$$

The vector $\boldsymbol{\delta}_{\mathrm{t}}$ is the tangential displacement on the inter-particle interface when corrected for contact rotation. In the case of slip, the length of $\boldsymbol{\delta}_{\mathrm{t}}$ is adjusted to a length consistent with Coulomb's condition ($||\boldsymbol{\delta}_{\mathrm{t}}|| = \mu ||\boldsymbol{f}_{\mathrm{n}}|| / k_{\mathrm{t}}$) (Luding, 2008; Radjaï and Dubois, 2011). The linear elasticity allows temporal integration with a constant time step length Δt.

The fluid model

The inter-particle fluid is handled by conventional continuum computational fluid dynamics (CFD). The implementation follows the compressible Darcian flow model

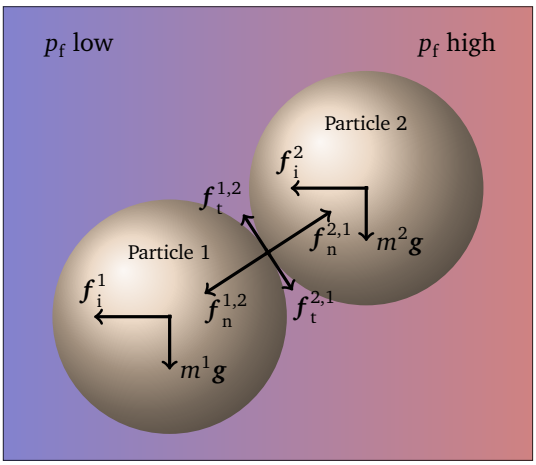

Figure 5.1. Schematic representation of body and surface forces of two non-rotating and interacting particles submerged in a fluid with a pressure gradient.

presented by Goren et al. (2011). This approach was favored over a full Navier-Stokes solution of fluid flow (Gidaspow, 1994; Zhu et al., 2007; Zhou et al., 2010; Kloss et al., 2012) since it allows for convenient parameterization of the hydrological permeabilities. The model assumes insignificant fluid inertia, which is appropriate for the subglacial setting.

The volumetric fraction of the fluid phase (the porosity, ϕ) is incorporated in the Eulerian formulations of the compressible continuity equation and momentum equation using the local average method (Anderson and Jackson, 1967; Xu and Yu, 1997). The Darcy constitutive equation is used for conserving momentum (Eq. 5.5) (McNamara et al., 2000; Goren et al., 2011):

$$\frac{\partial p_f}{\partial t} = \underbrace{\frac{1}{\beta_f \phi \mu_f}\left(k\nabla^2 p_f + \nabla p_f \cdot \nabla k\right)}_{\text{Spatial diffusion}} + \underbrace{\frac{1}{\beta_f \phi (1-\phi)}\left(\frac{\partial \phi}{\partial t} + \bar{\boldsymbol{v}}_p \cdot \nabla \phi\right)}_{\text{Particle forcing}} \tag{5.4}$$

$$(\boldsymbol{v}_f - \boldsymbol{v}_p)\phi = -\frac{k}{\mu_f}\nabla p_f \tag{5.5}$$

where $\boldsymbol{v}_f$ is the fluid velocity, $\boldsymbol{v}_p$ is the particle velocity, k is the hydraulic permeability, β_f is the adiabatic fluid compressibility and μ_f is the dynamic fluid viscosity. The continuity equation (Eq. 5.4) is in the form of a transient diffusion equation with the forcing term acting as a source/sink for the fluid pressure. The pressure, p_f, is the pressure deviation from the hydrostatic pressure distribution. This pressure deviation is sometimes referred to as the *excess pressure*. We refrain from using this term, as it may be misleading for pressures that are smaller than the hydrostatic value.

The simulation domain is discretized in a regular rectilinear orthogonal grid. The pressure is found using the Crank-Nicolson method of mixed explicit and implicit temporal integration, which is unconditionally stable and second-order accurate in time and space (e.g. Patankar, 1980; Ferziger and Perić, 2002; Press et

al., 2007). The implicit solution is obtained using the iterative Jacobi relaxation method (e.g. Ferziger and Perić, 2002; Press et al., 2007; Gerya, 2010), which is light on memory requirements and ideal in terms of parallelism for our graphics processing unit (GPU) implementation, although not optimal in terms of convergence. The numerical solution is continuously checked for stability by the Courant-Friedrichs-Lewy (CFL) condition (Courant et al., 1967). The partial derivatives are approximated by finite differences.

The granular-fluid coupling

The particle and fluid algorithms interact by direct forcings (Eqs. 5.1, 5.4, and 5.5) and through measures of porosity and permeability (Tsuji et al., 1992; Tsuji et al., 1993; Xu et al., 2001; Zhu et al., 2007; Goren et al., 2011).

Porosity

The local porosity is determined at the fluid cell center. For a cell with a set of N grains in its vicinity, it is determined by inverse-distance weighting the grains using a bilinear interpolation scheme (McNamara et al., 2000; Goren et al., 2011). The weight function s has the value 1 at the cell center and linearly decreases to 0 at a distance equal to the cell width (Δx, Fig. 5.2):

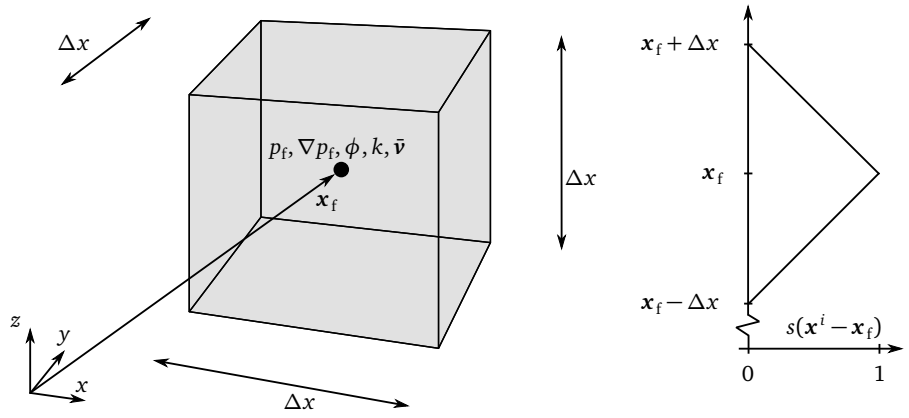

Figure 5.2. Left: A cell in the fluid grid. The node for pressure (p_f), the gradient of fluid pressure (∇p_f), porosity (ϕ), permeability (k), and average grain velocity ($\bar{\boldsymbol{v}}$) are calculated at the cell center. Right: The weight function (Eq. 5.7) at various distances.

$$\phi(\boldsymbol{x}_\mathrm{f}) = 1 - \frac{\sum_{i \in N} s^i V_\mathrm{g}^i}{\Delta x^3} \tag{5.6}$$

$$s^i = \begin{cases} \Pi_{d=1}^3 \left[1 - \frac{|\boldsymbol{x}_d^i - \boldsymbol{x}_{\mathrm{f},d}|}{\Delta x} \right] & \text{if } |\boldsymbol{x}_1^i - \boldsymbol{x}_{\mathrm{f},1}|, |\boldsymbol{x}_2^i - \boldsymbol{x}_{\mathrm{f},2}|, |\boldsymbol{x}_3^i - \boldsymbol{x}_{\mathrm{f},3}| < \Delta x \\ 0 & \text{otherwise} \end{cases} \tag{5.7}$$

Δx^3 is the fluid cell volume, and $\boldsymbol{x}_\mathrm{f}$ is the cell center position. Π is the product operator. The average grain velocity at the cell center is found using the same weighting function described above (Eq. 5.7). Additionally, large grains contribute to the velocity with a greater magnitude:

$$\bar{\boldsymbol{v}}(\boldsymbol{x}_\mathrm{f}) = \frac{\sum_{i \in N} s^i {V_g}^i \boldsymbol{v}^i}{\sum_{i \in N} s^i} \tag{5.8}$$

The change in porosity is the main forcing the particles excert onto the fluid (Eq. 5.5). At time step n it is estimated by central differences for second-order accuracy:

$$\left[\frac{\partial \phi}{\partial t}\right]^n \approx \frac{\phi^{n+1} - \phi^{n-1}}{2\Delta t} \tag{5.9}$$

The porosity at n+1 is found by estimating the upcoming particle positions from temporal integration of their current positions and velocities.

Permeability

Significant empirical evidence has been gathered about the proportionality between grain size and hydraulic properties of sediments (e.g. Hazen, 1911; Kozeny, 1927; Carman, 1937; Krumbein and Monk, 1943; Harleman et al., 1963; Schwartz and Zhang, 2003). The Kozeny-Carman estimation of permeability k is commonly used and of the form,

$$k = \frac{d^2}{180} \frac{\phi^3}{(1-\phi)^2} \tag{5.10}$$

where d is the representative grain diameter. Due to constrains on the computational time step we are unable to simulate fine grain sizes with realistic elastic properties within a reasonable time frame. In order to give a first-order estimate of the deformational behavior of fine-grained sediments, we therefore use a modified version of the above relationship, where the permeability varies as a function of the porosity and a predefined permeability pre-factor k_c:

$$k = k_\mathrm{c} \frac{\phi^3}{(1-\phi)^2} \tag{5.11}$$

Using this approach we can simulate large particles with the hydrological properties of fine-grained materials, while retaining the effect of local porosity variations on the intrinsic permeability. We do note, however, that the dilative magnitude during deformation is likely different for clay materials due to their plate-like shape. Sediments with a considerable amount of arbitrarily oriented clay minerals are likely to compact during deformation as the clay particles align to accommodate shear strain.

Particle-fluid interaction

The dynamic coupling from the pore fluid to the solid particles acts through the particle-fluid force ($\boldsymbol{f}_\mathrm{i}$) in Eq. (5.1). Our implementation of this coupling follows the procedure outlined by Xu and Yu (1997), Feng and Yu (2004) and Zhou et al. (2010) (scheme 3).

In a complete formulation, the interaction force on particles is composed of the drag force, determined by semi-empirical relationships (Ergun, 1952; Wen and Yu,

1966; Gidaspow et al., 1992; Di Felice, 1994), the pressure gradient force, the viscous force, as well as weaker interaction forces caused by particle rotation (Magnus force), lift forces on the particles caused by fluid velocity gradients (Saffman force), and interaction forces caused by particle acceleration (virtual mass force) (Zhou et al., 2010).

However, initial tests using a full Navier-Stokes solution for the fluid phase showed us that the pressure gradient force was by far the dominant interaction force in our pseudo-static shear experiments. The drag force was the second-most important force, but two orders of magnitude weaker than the pressure gradient force. Since we neglect fluid inertia, we included only the pressure gradient force. This force pulls particles towards relatively low fluid pressures and pushes them away from relatively high pressures. The fluid pressure in our model records the pressure difference from the hydrostatic pressure. For this reason we add a term to the pressure gradient force, which describes the buoyancy of a fully submerged particle as the weight of the displaced fluid:

$$\boldsymbol{f}_{\mathrm{i}} = -V_{\mathrm{g}} \nabla p_{\mathrm{f}} - \rho_{\mathrm{f}} V_{\mathrm{g}} \boldsymbol{g} \tag{5.12}$$

V_g is the volume of the particle, ρ_{f} is the fluid density and $\boldsymbol{g}$ is the vector of gravitational acceleration. The particle-fluid interaction force is added to the sum of linear forces per particle (Eq. 5.1). The particle force is not added to the fluid momentum equation (Eq. 5.4) since fluid inertia is ignored. The fluid is instead forced by variations in porosity.

Computational experiments

The computational fluid dynamics (CFD) algorithm is implemented in compute unified device architecture (CUDA) C (NVIDIA, 2013b) in order to allow a direct integration with the GPU-based particle solver. The coupled particle-fluid code is free software (source code available at `https://github.com/anders-dc/sphere`), licensed under the GNU Public License v.3. The simulations were performed on a GNU/Linux system with a pair of NVIDIA Tesla K20c GPUs. The experimental results are visualized using ParaView (Henderson et al., 2007) and Matplotlib (Hunter, 2007).

The experimental setup is a rectangular volume (Fig. 5.3) where a fluid-saturated particle assemblage deforms due to forcings imposed at the outer boundaries. We deform the consolidated material by a constant-rate shearing motion in order to explore the macro-mechanical shear strength under different conditions.

To determine the effects of the pore water, we perform experiments with and without fluids, and for the experiments with fluids present, the permeability prefactor k_{c} is varied to constrain the effect of the hydraulic conductivity and diffusivity on the overall deformation style. The low value used for k_{c} (3.5×10^{-15} m^2) results in an intrinsic permeability of $k = 1.9 \times 10^{-16}$ m^2 for a porosity of 0.3 (Eq. 5.11). The highest value ($k_c = 3.5 \times 10^{-13}$ m^2) matches a permeability of 1.9×10^{-14} m^2. These two end-member permeabilities roughly correspond to what Iverson et al. (1997a) and Iverson et al. (1998) estimated for the clay-rich Two Rivers till and the clay-poor Storgläciaren till, respectively.

The lower boundary is impermeable, and a fixed fluid pressure is specified for the top boundary. These boundary conditions imply that the simulated ice-bed interface is a relatively permeable zone with rapid diffusion of hydrological pressure, which is likely for subglacial beds with low permeability (e.g. Alley, 1989a;

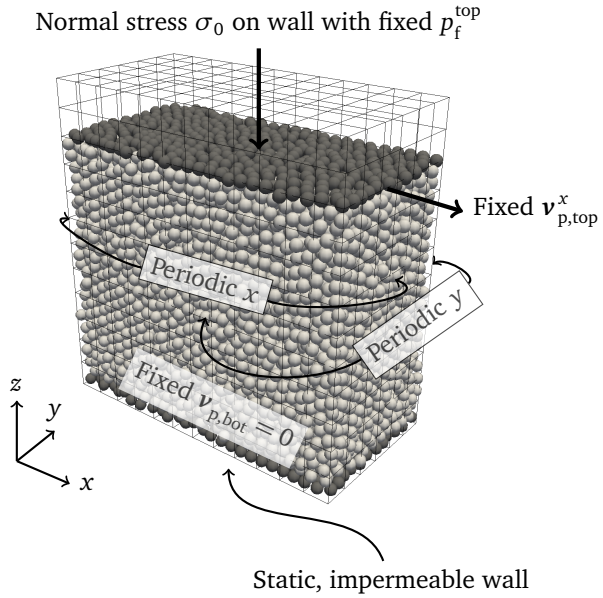

Figure 5.3. Experimental setup for the shear experiments. The fluid cells containing the mobile top wall are given a prescribed fixed-pressure boundary condition (p_f^{top}, Dirichlet). The bottom boundary is impermeable (no flow, free slip Neumann). The fluid grid is extended upwards to allow for dilation and movement of the upper wall. The granular phase is compressed between a fixed wall at the bottom, and a dynamic top wall, which exerts a normal stress (σ_0) downwards. The material is sheared by moving the topmost particles parallel to the x-axis.

Creyts and Schoof, 2009; Kyrke-Smith et al., 2014). In coarse-grained tills it is likely that the subglacial till diffusivity exceeds the hydraulic diffusivity at the ice bed interface. The lateral boundaries are periodic (wrap-around). If a particle moves outside the grid on the right side it immediately reappears on the left side. Likewise, particle pairs can be in mechanical contact although placed on opposite sides of the grid at the periodic boundaries.

The particle size distribution is narrow compared to that of subglacial tills, which often display a fractal size distribution (e.g. Hooke and Iverson, 1995). Fractal size distributions minimize internal stress heterogeneities (Hooke and Iverson, 1995; Iverson et al., 1996), but, in the absence of grain crushing, an assemblage with a wide particle size distribution dilates from a consolidated state with the same magnitude as assemblages with a narrow particle size distribution (Morgan, 1999) and displays the same frictional strength (Morgan, 1999; Mair et al., 2002; Mair and Hazzard, 2007). The comparable dilation magnitude justifies the computationally efficient narrow particle size distribution used here. As previously noted, shear zones in clay-rich materials can compact during shear due to preferential parallel alignment, which is not possible to capture with the methodology presented here.

The simulated particle size falls in the gravel category of grain size. The large size allows us to perform the temporal integration with larger time steps (Radjaï and Dubois, 2011; Damsgaard et al., 2013). The frictional force between two bodies is independent of their size (Amontons' second law) but is proportional to the normal force on the contact interface (Mitchell and Soga, 2005), as reflected in the contact law in the discrete element method (Eq. 5.3). We prescribe the normal forcing at the boundary as a normal stress, which implies that the normal force exerted onto a particle assemblage at the boundaries scales with domain size. For a number of total particles in a given packing configuration the ratio between particle size and inter-particle force is constant, which causes the shear strength to be independent of simulated particle size. This scale-independence is verified in laboratory experiments, where the granular shear strength of non-clay materials is known to be mainly governed by grain shape and surface roughness instead of grain size (Schellart, 2000; Mitchell and Soga, 2005).

Experiment preparation and procedure

The particles are initially placed in a dry, tall volume, from where gravity allows them to settle into a dense state. The particle assemblage is then consolidated by moving the fluid-permeable top wall downwards until the desired level of consolidation stress is reached for an extended amount of time. The same top wall is thereafter used to shear the material in a fluid-saturated state (Fig. 5.3).

For the shear experiments, the uppermost particles are forced to move with the top wall at a prescribed horizontal velocity (Fig. 5.3). The particles just above the bottom wall are prescribed to be neither moving or rotating. The micro-mechanical properties and geometrical values used are listed in Table 5.1.

Table 5.1. Parameter values used for the shear experiments.

Parameter	Symbol	Value
Particle count	N_p	9,600
Particle radius	r	0.01 m
Particle normal stiffness	k_n	1.16×10^9 N m^{-1}
Particle tangential stiffness	k_t	1.16×10^9 N m^{-1}
Particle friction coefficient	μ	0.5
Particle density	ρ	2600 kg m^{-3}
Fluid density	ρ_f	1000 kg m^{-3}
Fluid dynamic viscosity	μ_f	1.797×10^{-8} to 1.797×10^{-6} Pa s
Fluid adiabatic compressibility	β_f	1.426×10^{-8} Pa^{-1}
Hydraulic permeability prefactor	k_c	3.5×10^{-15} to 3.5×10^{-13} m^2
Normal stress	σ_0	20 kPa
Top wall mass	m_w	280 kg
Gravitational acceleration	$\boldsymbol{g}$	9.81 m s^{-2}
Spatial domain dimensions	$\boldsymbol{L}$	[0.52, 0.26, 0.55] m
Fluid grid size	$\boldsymbol{n}$	[12, 6, 12]
Shear velocity	$\boldsymbol{v}^x_\mathrm{p,top}$	2.32×10^{-2} m s^{-1}
Inertia parameter value	I	1.7×10^{-4}
Time step length	Δt	2.14×10^{-7} s
Simulation length	t_total	20 s

Scaling of the shear velocity

The heavy computational requirements of the discrete element method necessitates upscaling of the shearing velocity in order to reach a considerable shear strain within a manageable length of time. Temporal upscaling does not influence the mechanical behavior of dry granular materials, as long as the velocity is below a certain limiting velocity (GDR-MiDi, 2004; Damsgaard et al., 2013; Gu et al., 2014). The shearing velocity used here (2.32×10^{-2} m s^{-1}), although roughly three orders of magnitude greater than the velocities observed in subglacial environments (e.g. 316 m a^{-1} = 10^{-5} m s^{-1}), guarantees quasi-static, rate-independent deformation in the granular phase, identical to the behavior at lower strain rates. The particle inertia parameter, I, quantifies the influence of grain inertia in dry granular materials (GDR-MiDi, 2004). Values of I below 10^{-3} correspond to pseudo-static and rate-independent shear deformation in dry granular materials. I has a value of 1.7×10^{-4} in the shear experiments of this present study.

The fluid phase needs separate treatment in order to correctly resolve slow shear behavior at faster shearing velocities. This behavior is achieved by linearly scaling the fluid dynamic viscosity with the relationship between actual shearing velocity and the reference glacial sliding velocity. By decreasing the viscosity the fluid is allowed to more quickly adjust to external and internal forcings. The velocity scaling adjusts the time-dependent parameters of hydraulic conductivity and diffusivity correctly. The intrinsic permeability k is time-independent, and the values produced here are directly comparable with real geological materials. The fluid viscosity is scaled to a lower value of 1.797×10^{-6} Pa s, consistent with the scaling factor used for the shearing velocity. We test the influence of shearing rate by varying this parameter.

5.3 Results

First we investigate the strain-rate dependence of the sediment strength and dilation by shearing a relatively impermeable sediment ($k_c = 3.5 \times 10^{-15}$ m^2) at different shear velocities. The shear velocity directly influences the magnitude of the peak shear strength, dilation and internal fluid pressure (Fig. 5.4 and 5.5). At relatively large shearing velocities the dilation rate exceeds the pore-pressure diffusion rate, and the internal pressure reduction strengthens the material. At lower shearing velocities the material is substantially weaker due to a decreased dilation rate, where the pore pressure diffusion has more time to adjust to the volumetric changes in the shear zone.

At the reference shearing velocity the peak shear frictional strength is 0.71, which corresponds to 14 kPa at an effective stress of 20 kPa (Fig. 5.4, top left, Fig. 5.6). When sheared a hundred times slower, the peak shear friction has decreased to 0.62, corresponding to 12 kPa (Fig. 5.4, top right, Fig. 5.6). The peak values are measured during the transition from the dense and consolidated pre-failure state to the critical state where a shear zone is fully established. This transition is characterized by rapid dilation due to porosity increases in the shear zone (Fig. 5.4, middle). During fast shearing velocities the volumetric change outpaces the diffusion of fluid pressure, causing the internal pore-water pressure in the shear zone to decline (Fig. 5.4, bottom and Fig. 5.5). Dilatant hardening causes the peak shear strength to increase at large shear velocities (Fig. 5.6), while the strength reduces to the pure granular strength for lower velocities.

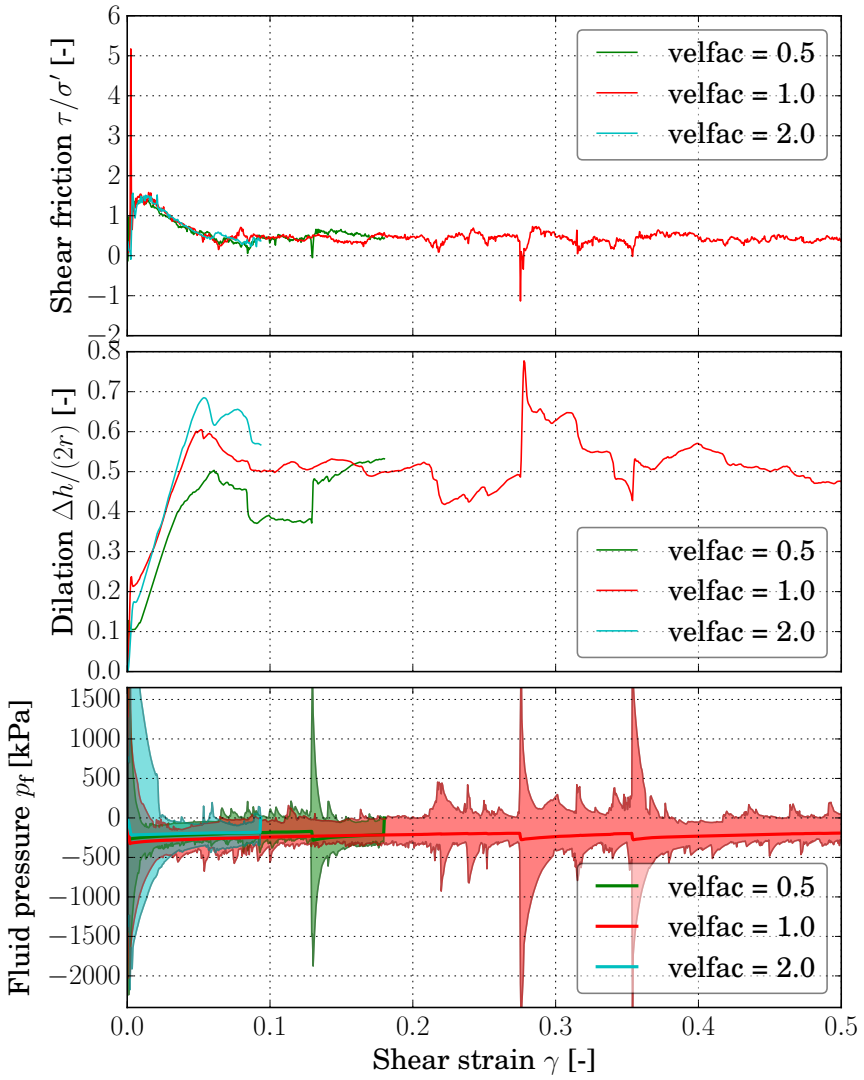

Figure 5.4. Shear experiments with different shearing rates. (Top) unsmoothed and smoothed shear friction values, (center) dilation in number of grain diameters and (bottom) minimum, mean, and maximum fluid pressures. The permeability prefactor value is $k_c = 3.5 \times 10^{-15}$ m^2. The shear friction values (top) are smoothed with a moving Hanning window function to approximate the strength of larger particle assemblages. The material peak strength increases with strain rate due to reductions of internal fluid pressure. This strengthening is taking place when the dilation rate exceeds the dissipation rate of the fluid.

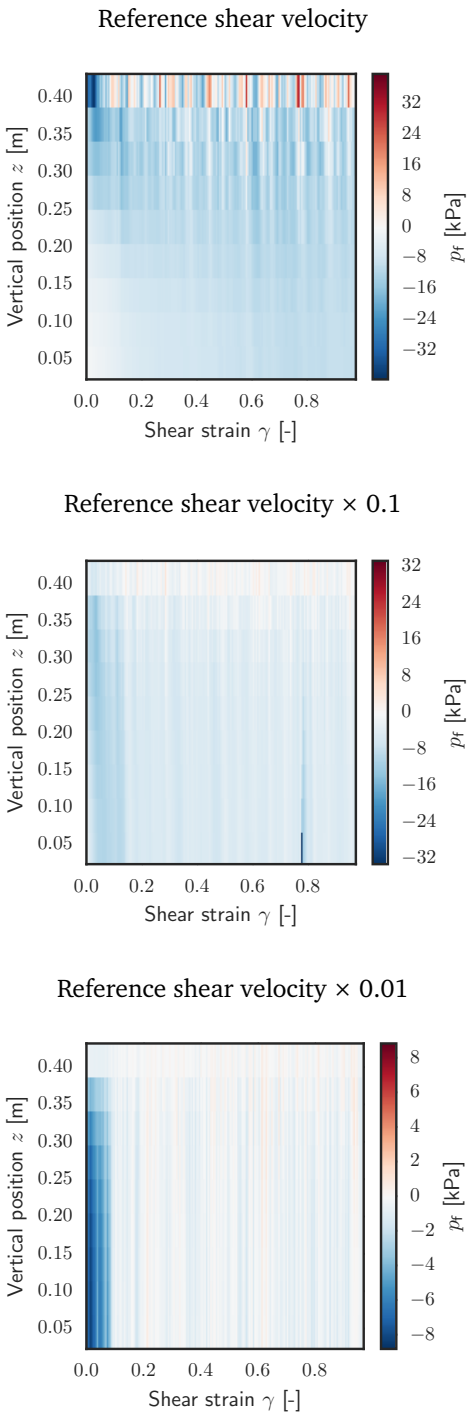

Figure 5.5. Temporal evolution (x-axis) of horizontally averaged fluid pressures (y-axis). At fast shear rates (top) there are large internal pressure decreases and slow recovery due to a large dilation rate and an insufficient pressure dissipation. When the shearing velocity is decreased (middle) and (bottom) the dissipation rate becomes increasingly capable of keeping internal pressures close to the hydrostatic pressure (0 kPa).

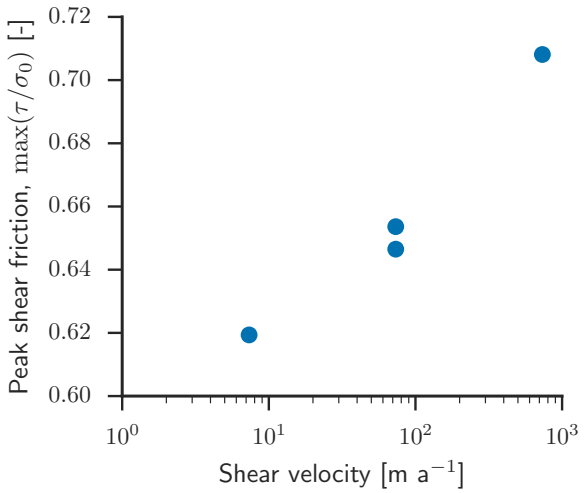

Figure 5.6. Peak frictional strength before the critical state of the low-permeability granular bed ($k_c = 3.5 \times 10^{-15}$ m^2) at different shear velocities. The frictional strength is constant and rate-independent at velocities lower than 10^1 m a^{-1} as pore-pressure diffusion rates far exceed rates in volumetric change.

In this model framework, adjusting the hydraulic permeability of the same coarse sediment leads to similar conditional strengthening as shearing the sediment at different rates (Fig. 5.7). Without fluids (the dry experiment), the peak shear friction (Fig. 5.7, left) is relatively low and the shear stress is dominated by high-frequency fluctuations. The fluid-saturated experiment with the relatively high permeability ($k_c = 3.5 \times 10^{-13}$ m^2) has similar shear strength, but the high-frequency oscillations in shear friction are reduced by the fluid presence. The dilation is similar to the dry experiment, but with slightly decreased magnitude. The mean fluid pressure deviation from hydrostatic values (Fig. 5.7, bottom left) is close to zero. The low-permeable experiment (Fig. 5.7, right) is characterized by the largest initial peak strength, and lowest magnitude of dilation. Compared to the other experiments, the dilation reaches its maximum values at lower shear strain. The fluid pressure decreases almost instantaneously at first, whereafter it equilibrates towards the hydrostatic value (0 Pa).

At constant shearing rate with different permeabilities (Fig. 5.8, top) or at variable shearing rates with constant permeability (Fig. 5.8, bottom), we observe that pore water dynamics have a significant effect on the distribution of strain. The presence of pore water causes a more shallow deformational profile. Progressively lowering the permeability or increasing the shear velocity decreases the deformational depth.

The effects of the fluid are visible at different depths within the deforming material (Fig. 5.9 and 5.10). The deformation is pervasive with depth for the relatively permeable experiment (Fig. 5.9 top), and the fluid pressures deviate only slightly from the hydrostatic values (red). The relatively small pressure gradients cause only weak fluid forces on the particles in this experiments. Contrasting these

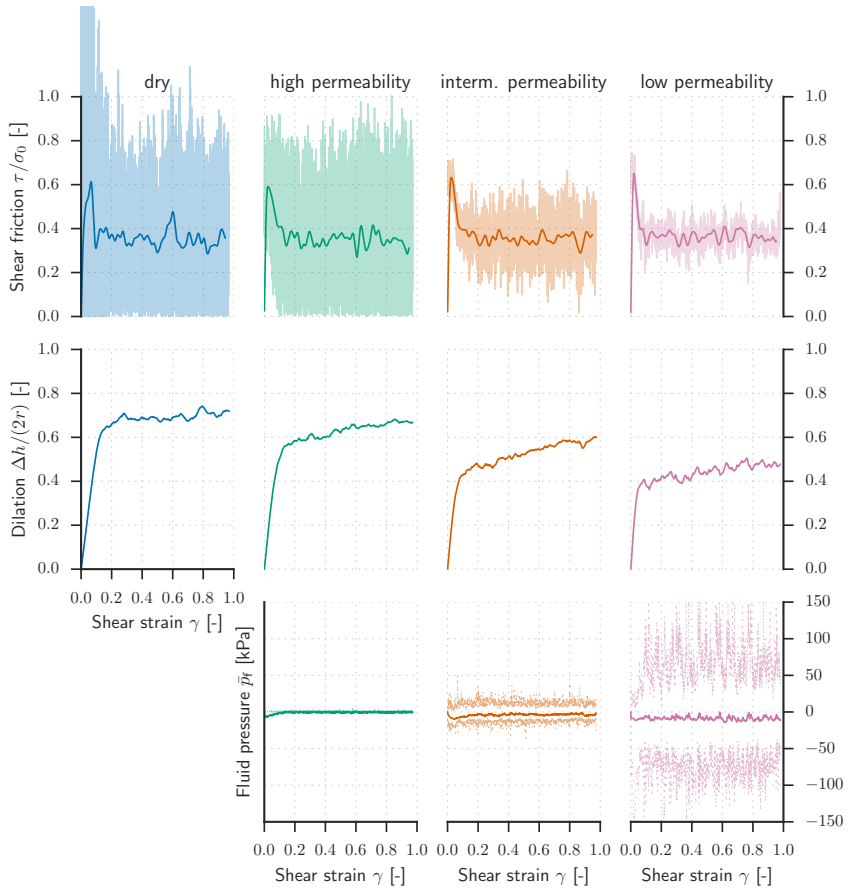

Figure 5.7. (Top) shear strength, (center) dilation in number of grain diameters and (bottom) minimum, mean and maximum fluid pressures in shear experiments with different permeability properties.

results, deformation is in the impermeable experiment primarily governed by decoupling of the top wall and the particles in the bed below (Fig. 5.9 and 5.10, bottom).

Differences in hydraulic permeability influence the dynamics of the fluid over time, as illustrated in Fig. 5.11. The fluid pressures in the permeable material (top) are initially predominantly negative, reflecting the increasing dilation (Fig. 5.7, middle). In the critical state (after a shear strain value of 0.1), the fluid pressures fluctuate around the hydrostatic value (0 Pa).

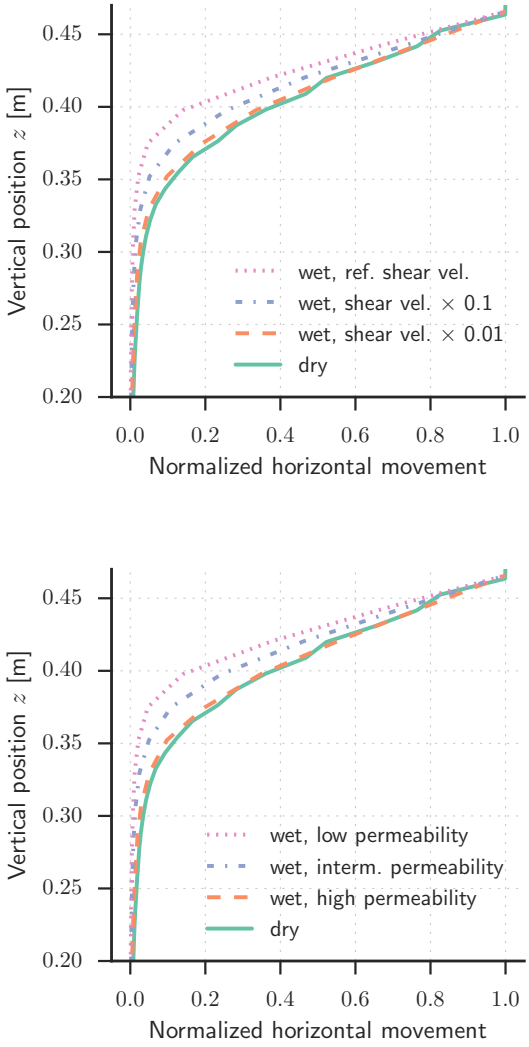

Figure 5.8. Horizontal particle displacement with depth (shear strain profiles) for the dry and fluid saturated shear experiments. Top: Displacement profiles from experiments with different shear velocities. Bottom: Displacement profiles from experiments with different permeabilities.

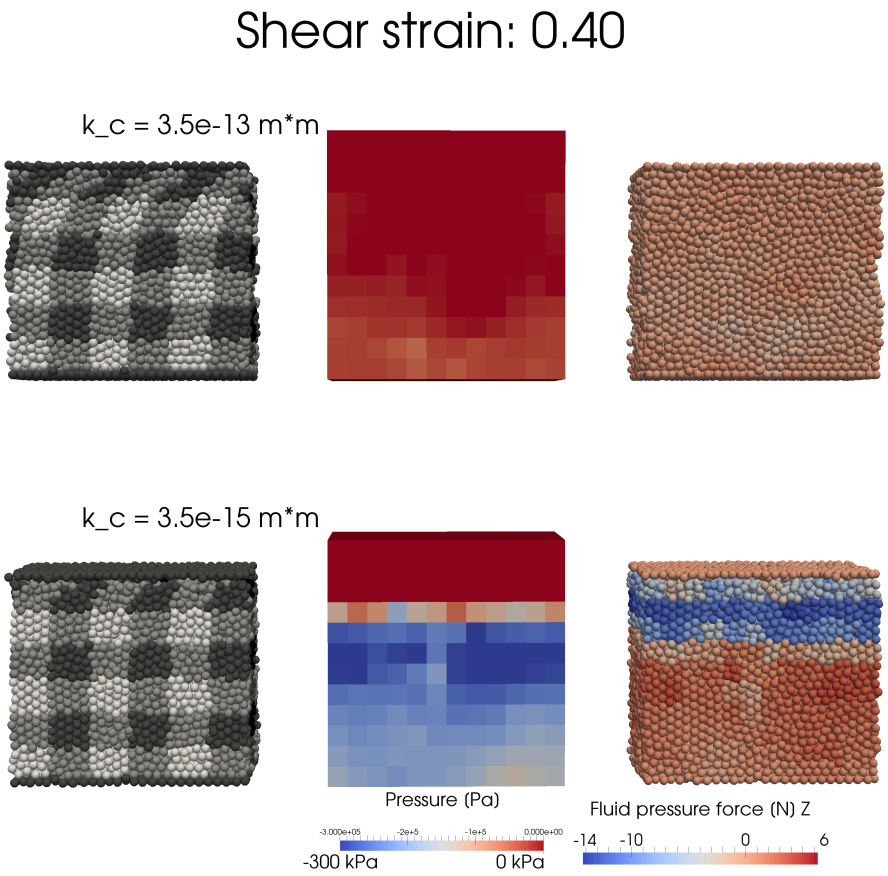

Figure 5.9. Particle displacement and fluid forces for different permeabilities at a shear strain of 0.25. (Left) particles colored by their original position, (center) particles colored by their displacement along the x-axis, (right) vertical (z) forces from the fluid onto the particles. In the permeable material and/or at low shearing velocities (top), the internal volumetric changes are accommodated by porous flow. This keeps the fluid pressures close to hydrostatic values and causes deep deformation (top center). In materials which are impermeable and/or are sheared at fast rates (bottom), the volumetric changes cause drastic pore-pressure reductions, effectively strengthening the material (bottom right) and focusing deformation at the top (bottom left and center).

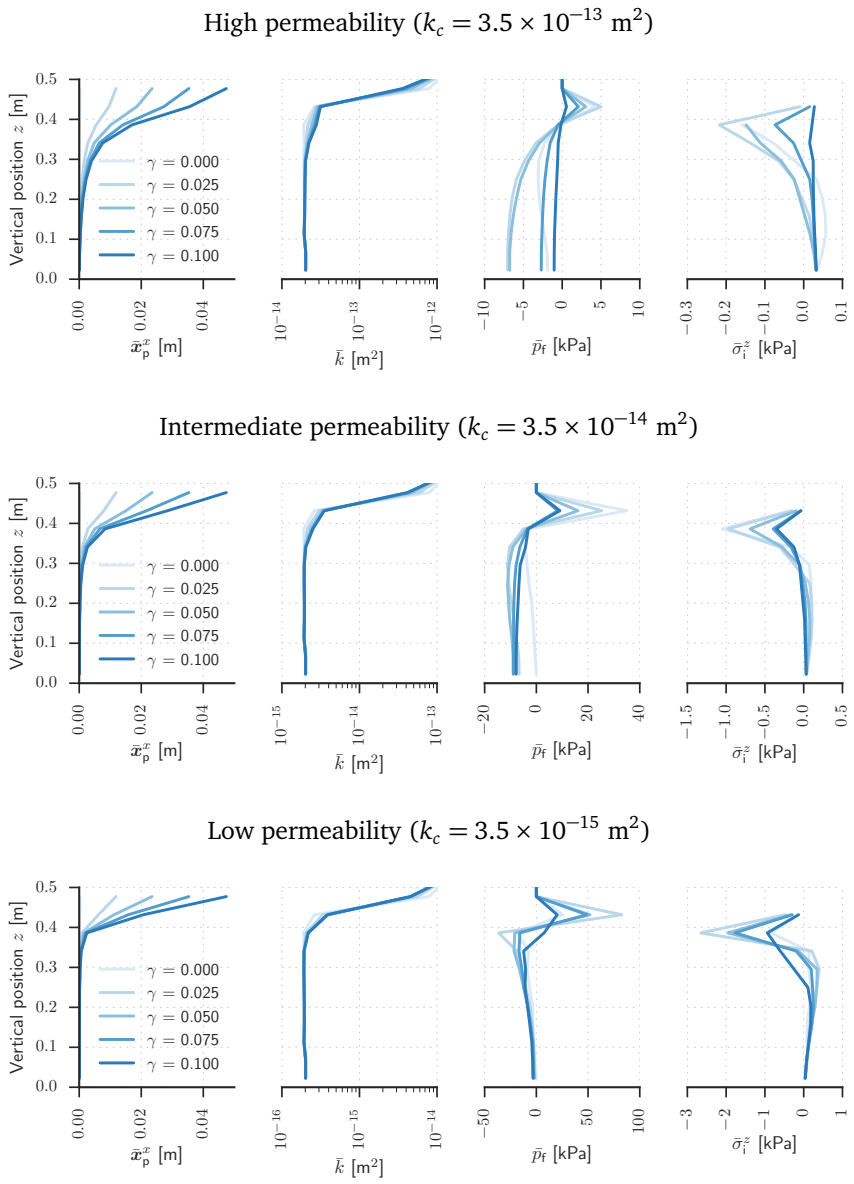

Figure 5.10. Horizontally averaged fluid and particle behavior with progressive shear strain. (left) Vertical particle displacement, (center left) mean permeability, (center right) mean fluid pressure, and (right) vertical component of the mean fluid stress, calculated as $\boldsymbol{f}_\mathrm{i}^i/A^i$, where $\boldsymbol{f}_\mathrm{i}^i$ is the fluid pressure force on particle i from Eq. 5.12 and A^i is its surface area.

Relatively permeable ($k_c = 3.5 \times 10^{-13}$ m^2)

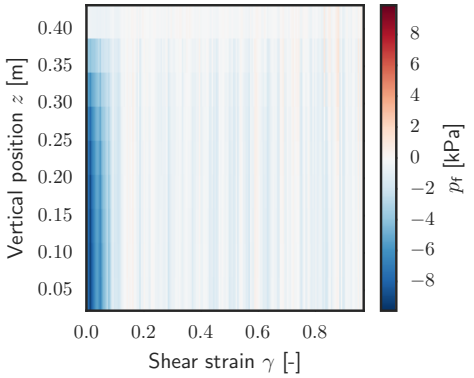

Relatively impermeable ($k_c = 3.5 \times 10^{-15}$ m^2)

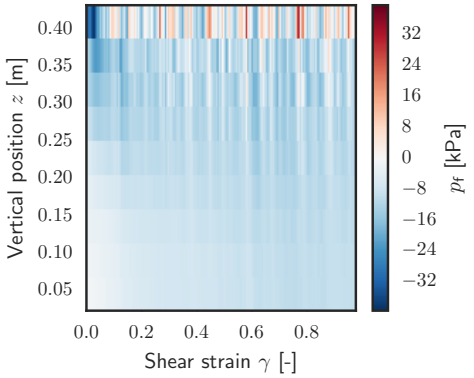

Figure 5.11. Temporal evolution (x-axis) of horizontally averaged fluid pressures (y-axis). The permeable material (top) is able to quickly respond to internal volumetric changes, which are short-lived and of small magnitude. The low-permeable material (bottom) is dominated by large pressure reductions and relatively slow relaxation.

5.4 Discussion

Strain-rate dependency

Several studies have highlighted the importance of feedbacks between the solid and fluid phases during granular deformation (e.g. Iverson et al., 1994; Iverson et al., 1997b; Iverson et al., 1998; Pailha et al., 2008; Iverson, 2010; Rondon et al., 2011; Mutabaruka et al., 2014). A shear-rate dependency in a grain-fluid mixture can only originate from the fluid phase, since dry granular materials deform rate-independently under pseudo-static shear deformation (GDR-MiDi, 2004; Damsgaard et al., 2013). Rate dependency emerges, however, as soon as the flow of viscous pore fluids starts to influence the solid phase.

Water has a relatively low viscosity, which implies that the shear stress required to deform the fluid phase alone is extremely low. The fluid phase does however influence the bulk rheology if diffusion of fluid pressures is limited relative to volumetric forcing rates, as in a rapidly deforming but relatively impermeable porous material. The coupled particle-fluid interactions cause the material to respond as a low-pass filter when forced with changes in volume and porosity. The reequilibration of pressure anomalies depends on the volumetric strain rate, water viscosity and material permeability. Any forcing that affects local porosity causes the material to respond in part like a viscous dashpot due to internal fluid flow.

Dilatant hardening: Effects on sediment strength and deformation depth

When deformed, granular materials often undergo volumetric changes in order to attain the optimal packing for continuous deformation (e.g. Schofield and Wroth, 1968). Shear zones within dense granular materials (normally consolidated) typically expand (Fig. 5.7, middle) in a process known as Reynolds dilation (Reynolds, 1885; Mead, 1925). The pore-volume increase internally in the shear zone causes a local reduction in pore-water pressure, and a deviation from the hydrostatic pressure distribution. The appearance of hydraulic gradients drives fluid flow into the shear zone. Considering the Mohr-Coulomb constitutive relation for till rheology, the reduction of pore-water pressure reduction increases the effective stress, which in turn strengthens the material in the shear zone (Fig. 5.12). In our results, the particles are pushed towards the shear zone by the pressure gradient force (Fig. 5.13). The tangential strength of inter-particle contacts is in the DEM determined by Coulomb friction (Eq. 5.3), which implies a linear correlation between contact normal force and tangential contact strength. Heavily loaded particle contacts are thus less likely to slip, and chains of particles with strong contacts cause increased resistance to deformation (Damsgaard et al., 2013). The convergence of particles strengthens the inter-particle contacts and increases the shear friction until hydrostatic pressure conditions are reestablished.

The dilative strengthening requires sufficiently low hydraulic diffusivities relative to the shear zone dilation rate (e.g. Iverson et al., 1997b; Moore and Iverson, 2002; Iverson, 2010). Dilation ceases when a sediment reaches the critical state. Owing to the granularity of the material, the vertical strain rate displays small fluctuations around levels corresponding to the critical state value. The small volumetric oscillations create new fluid-pressure deviations from the hydrostatic value, which slightly weaken or strengthen the sediment (Fig. 5.7, top, and Goren et al.

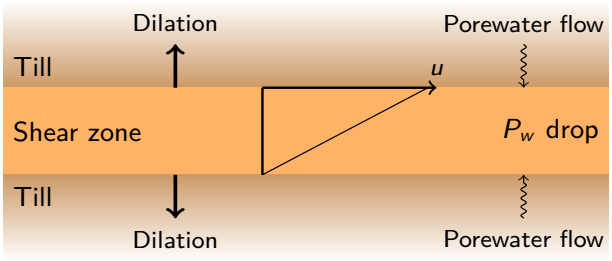

Figure 5.12. Particle-fluid interaction during deformation of a consolidated sediment. After Iverson et al. (1998).

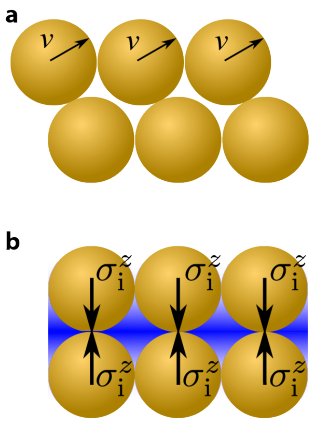

Figure 5.13. Micro-mechanical cause of dilatant hardening. A consolidated sediment (top) is deformed with a vertical gradient in velocity. The grains are forced past each other in order to accommodate the shear strain. The deformation causes dilation, which increases porosity localy and decreases fluid pressure (bottom). The established gradient in fluid pressure pulls particles together (Eq. 5.12), which increases the load on inter-particle contacts. The larger inter-particle normal stress increases the shear strength of the contact (Eq. 5.3) resulting in a stronger sediment.

(2011)). In cases where the shear stress is close to the sediment shear strength, the hardening may be sufficient to stabilize patches of the bed (Piotrowski, 1987).

The granular model applied here is not able to reproduce the shear-induced compaction that clay-rich materials can display during early shear (e.g. Dewhurst et al., 1996), but we can speculate about the rheological consequences. The compaction causes increased pore-water pressure in the shear zone, in cases where the volumetric change exceeds the time scale of pore-water pressure diffusion. Some of the compressive stress normal to the shear zone orientation is consequentially reduced, which decreases the material strength. The reduction of strength due to compaction is rate-dependent like the dilative hardening.

The shear zone thickness is in our experiments heavily influenced by the dilatant hardening where a low permeability causes extremely localized failure at the upper moving interface (Fig. 5.8 and 5.9, left). This is consistent with the laboratory results by Iverson et al. (1997a), where the shear zone in the coarse-grained Storgläciaren till in all cases was wider than the shear zone of the fine-grained Two Rivers till. The velocity profile of the shear zone determines the material flux. A shallower deformation depth and a lower subglacial sediment transport rate is thus to be expected from subglacial shearing of compacted, low-permeable sediments, relative to permeable counterparts. These results are consistent with observations of very shallow deformation of subglacial tills with a relatively low permeability (Engelhardt and Kamb, 1998; Piotrowski et al., 2004).

Our results demonstrate how the interplay between the solid and fluid phases can influence the sediment strength. Pore-water pressures decrease during deformation, and shear strength increases until deformation ceases or the critical state is reached. Once the local and regional hydraulic system recovers from the pore-pressure reduction, the sediment strength is once again reduced and a new deformation phase may be initiated (Fig. 5.14). The magnitude of strengthening is dictated by the ability of the subglacial hydrological system to accommodate reductions in pressure at the ice-bed interface (Fig. 5.15).

A variable shear strength of the till influences ice flow if the basal shear stress is in the range of the strength values. Since surface slopes of ice streams are low, driving stresses tend to be low as well. Inferred values of driving stresses at the Northeast Greenland ice stream (Joughin et al., 2001), Whillans Ice Stream and ice plain (Engelhardt and Kamb, 1998), and Pine Island Glacier (Thomas et al., 2004) lie within the range of 2 to 23 kPa (Alley and Whillans, 1991; Cuffey and Paterson, 2010), and are thus potentially sensitive to the variability in till strength. If the glacier moves with variable velocities in a stick-slip or surging manner, periods of stagnant ice flow may consolidate and strengthen the sediment, in effect delaying the following slip event (Iverson, 2010).

5.5 Conclusions

We numerically simulate a two-way coupled particle-fluid mixture under pseudo-static shear deformation. The grains are simulated individually by the discrete element method, while the fluid phase is treated as a compressible and slowly flowing fluid adhering to Darcy's law. The fluid influences the particles through local deviations from the hydrostatic pressure distribution. Due to the extremely low viscosity of water, the deformational behavior of dense granular material is governed by inter-grain contact mechanics. The porosity of a granular packing evolves asymp-

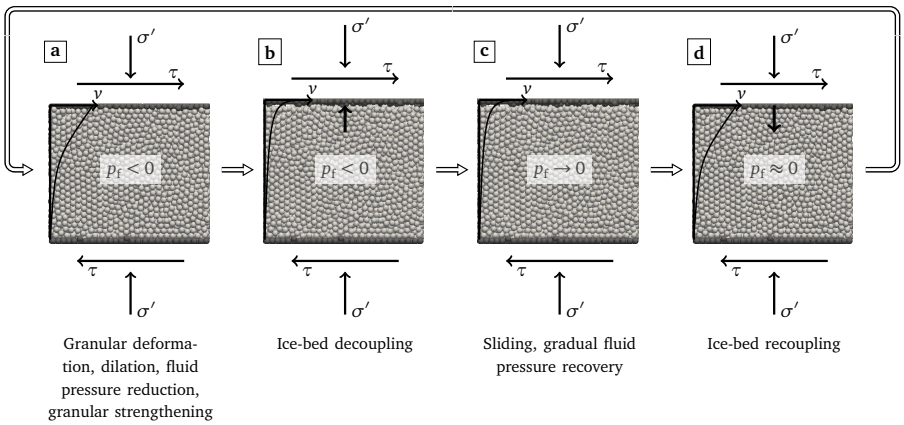

Figure 5.14. Conceptual model of cyclic strengthening. Feedbacks between sediment and pore-water during shear of a consolidated sediment with low permeability cause strengthening of the sediment during the onset of deformation. The strengthening may cause interfacial decoupling between the glacier and its bed until pore-water pressures in the sediment have recovered. The recoupling causes a new event of deep deformation which yet again causes sediment strengthening.

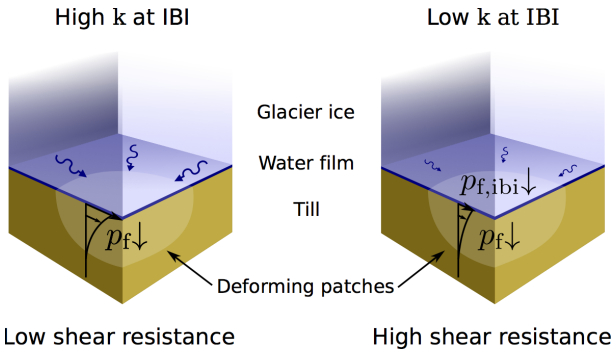

Figure 5.15. The magnitude of strengthening felt by the glacier due to dilatant hardenining depends on the permeability and water availability at the IBI. If the subglacial hydrological system has a high permeability and a thick water film at the IBI (left), the till directly beneath the glacier sole is kept weak because the pore-water pressure is unchanged in the upper-most parts. If the IBI on the other hand has a low permeability and a thin water film (right), the bed strengthens as the volumetric expansion of the till reduces pore-water pressure at all depths.

totically towards a constant value when deformed. Changes in porosity cause deviations from the hydrostatic pressure if the rate of porosity change exceeds the rate of pressure diffusion. The rate of pressure diffusion is governed by the fluid viscosity, the local porosity and the hydraulic permeability. Low fluid pressures developing due to sediment dilation cause a volumetric contraction in the granular phase which increases the stress between particles, in turn increasing the strength of individual grain contacts. The magnitude of the strengthening effect is rate-dependent, and increases with shear velocity and decreases with increasing hydraulic permeability. The resulting rheology is perfect-plastic for permeable or slowly deforming tills while rate-dependent dilative strengthening contributes to the material strength during early stages of fast deformation of impermeable and dilating tills. If the till is clay-rich, compaction due to microfabric development in the shear zone is expected to weaken the sediment, causing a rate-weakening with increased shear rate until the excess pressures are reduced by hydraulic diffusion.

We furthermore show that for a fast shear velocity (732 m a^{-1}) permeable sediments are only weakly influenced by the fluid phase, resulting in little shear strengthening and a deep decimeter-scale deformation dictated by the normal stress and grain sizes. Impermeable and consolidated sediments display slight dilatant strengthening at high shear velocity. The strengthening causes deformation to focus at the ice-bed interface where pore-water pressures are higher and relatively constant. The depth of deformation is then on the centimeter-to-millimeter scale. Actively deforming patches in the subglacial mosaic of deforming and stable spots act as sinks for meltwater and can cause substantial thinning of a water-film at the ice-bed interface. If the subglacial shearing movement halts, the sediment gradually weakens as the fluid pressure readjusts to the hydrostatic value. The temporal changes in sediment strength may explain observed variability in glacier movement.

Acknowledgments

Anders Damsgaard benefited from discussions with Jean-Yves Delenne, Hans Petter Langtangen, Kenni Dinesen Petersen, Keld Rømer Rasmussen, Liran Goren, and Jenny Suckale during model development and application. This research was funded by the Danish Council for Independent Research under the Sapere Aude programme.

Chapter 6

Paper 3: *Creep, stick and slip in subglacial granular beds forced by variations in melt-water pressure*

Anders Damsgaard[1], David L. Egholm[1], Lucas H. Beem[2], Nicolaj K. Larsen[1], Slawek Tulaczyk[2], and Jan A. Piotrowski[1]

1. Department of Geoscience, Aarhus University, Aarhus C, Denmark.
2. Seismological Laboratory, Division of Geological and Planetary Sciences, California Institute of Technology, Pasadena, California, USA.
3. Department of Earth and Planetary Sciences, University of California, Santa Cruz, California, USA.

In preparation.

Abstract

Glaciers often move by deformation of underlying melt-water saturated deformable sediments whose mechanical behavior remains poorly understood. Here we use new computational experiments on water-saturated granular materials to show that a granular bed can change mechanical behavior, when for example variations in melt-water pressure disturb the dynamic balance of the grain packing. We find that the bed switches between modes of stick, rate-dependent creep, and rate-independent failure, depending on changes in the external forcing. Our results show that these transitions in mechanical mode can explain velocity variations in granular materials, and uncovering their underlying fundamental physics improves our understanding glacier sensitivity to climate change.

One Sentence Summary:
Failure of grain contacts due to variations in pore-water pressure explains slow creeping movement of granular materials under glaciers.

6.1 Main text

Glaciers and ice sheets flow over a substratum largely by three mechanisms (Cuffey and Paterson, 2010): 1) internal deformation of the ice by viscous creep, 2) sliding at the ice-bed interface, or 3) deformation of unconsolidated subglacial sediments (Iverson et al., 1995; Hooke et al., 1997; Kavanaugh and Clarke, 2006). Fast flowing glaciers and ice streams are typically at the pressure melting point due to the weight of the overlying ice, frictional heating during movement, and heat from the underlying bedrock crust. Such thermal conditions allow liquid water in the subglacial environment. Hence, sedimentary subglacial beds often host melt-water saturated and actively deforming granular materials (till), consisting of either reworked older sedimentary deposits or mobilized products from erosion (Evans et al., 2006; Cuffey and Paterson, 2010). The till may be weaker than the glacier ice itself, causing till deformation in many cases to constitute a significant fraction of the total movement measured at the glacier surface (Blake et al., 1994; Hooke et al., 1997; Engelhardt and Kamb, 1998; Cuffey and Paterson, 2010), and fast ice flow is hence often collocated with sedimentary beds (Anandakrishnan et al., 1998).

The mechanical behavior of subglacial till is thus of primary importance to understand ice flow. However, the mechanical controls on till strength and deformation style are poorly known. The subglacial environment is difficult to access and experimentally analyze, and the physics of subglacial till deformation has consequently been a topic of long-lasting and intense discussion (Alley et al., 1986; Boulton, 1986; Boulton and Hindmarsh, 1987; Kamb, 1991; Iverson et al., 1995; Hooke et al., 1997; Hindmarsh, 1997; Iverson et al., 1998; Tulaczyk et al., 2000a; Fowler, 2003; Clarke, 2005; Kavanaugh and Clarke, 2006; Rathbun et al., 2008; Iverson and Zoet, 2015). The constitutive relations proposed for till range from shear-velocity strengthening (Boulton and Hindmarsh, 1987; Alley et al., 1987b), velocity weakening (Iverson et al., 1994; Iverson et al., 1999; Thomason and Iverson, 2008), to a strength essentially independent of shear velocity (Kamb,

1991; Iverson et al., 1998; Tulaczyk et al., 2000a). Mechanics based on velocity-strengthening actively dampens variations in ice-flow velocity by increasing frictional resistance when deformation accelerates and vice versa. Models based on velocity-weakening or velocity-independent till strength may, on the other hand, explain rapid flow oscillations and unstable feedbacks in glacier flow, which may ultimately lead to ice sheet collapse (Alley, 1990; Kamb, 1991; Zwally et al., 2002; De Angelis and Skvarca, 2003; Rignot et al., 2004; Thomason and Iverson, 2008; Zoet and Iverson, 2015). Models based on velocity-strengthening (or viscous relations) are practical for theoretical studies of glacier evolution, since they offer a one-to-one relationship between stress and deformation rate (Alley et al., 1987b; Hindmarsh, 1998; Fowler, 2000). Yet, evidence from *in-situ* measurements and laboratory experiments strongly supports the notion of a plastically deforming till with little correlation between glacier sliding velocity and subglacial till strength. The strength seems instead to be controlled by effective pressure, the fraction of ice overburden that is not carried by subglacial water pressure (Kamb, 1991; Fischer and Clarke, 1997; Hooke et al., 1997; Iverson et al., 1998; Tulaczyk et al., 2000a; Damsgaard et al., 2013).

The influence of effective pressure is supported by several studies of positive correlation between surface melt production, subglacial water pressure, and glacier flow (Fischer and Clarke, 1997; Hooke et al., 1997; Zwally et al., 2002; Bartholomaus et al., 2008; Bartholomew et al., 2010). Glaciers can accelerate in this case because the melt-water produced at the surface is routed to the glacier bed, where water pressure increases and lowers the effective pressure. Likewise, many West Antarctic ice streams that drain ice to the ocean flow at highly variable speeds, because tidal movements in the floating part of the glacier modulate the upstream distribution of pore-water pressure and stress from the ice (Bindschadler et al., 2003; Winberry et al., 2011; Walker et al., 2013; Thompson et al., 2014). Although surface-melting glaciers and Antarctic tidal ice streams are dissimilar in many ways, the basic reason for their variable velocity may be the same: reduction of effective pressure weakens the frictional strength of the glacier bed.

In order to study the mechanical response of a granular bed to transient stress perturbations, we designed computational experiments where the force-balance of a fluid-saturated granular material is disturbed by variations in effective pressure. This approach is new for a subglacial setting, but highly rewarding compared to standard continuum methods because it obviates a priori assumptions regarding the macroscopic rate-dependency of the material strength. Generally speaking, the mechanical behavior of a granular material results from the properties of the individual grains and their collective self-organizing arrangement. Because of the way stress is transmitted along force-bearing chains of grains (Fig. 6.1B), granular materials have an inherent ability to change mechanical phase, for example between solid and fluidized states, and the transitions are known to drastically influence the load-bearing capacity (Jaeger and Nagel, 1992; GDR-MiDi, 2004). We used a coupled numerical method where the dynamics of the solid is resolved per grain (Cundall and Strack, 1979; Damsgaard et al., 2013), while pore-water flow is controlled by Darcian diffusion (Goren et al., 2011). The computational experiment involves a small three-dimensional sample (0.52 x 0.26 x 0.55 m) of sediment represented by 9,600 grains. The comparability between experiment and true subglacial setting thus depends on the scale-independency of granular geotechnical properties (Fowler, 2003; Tulaczyk, 2006; Feng et al., 2009; Iverson and Zoet, 2015), and the fundamental consistency of the Mohr-Coulomb failure

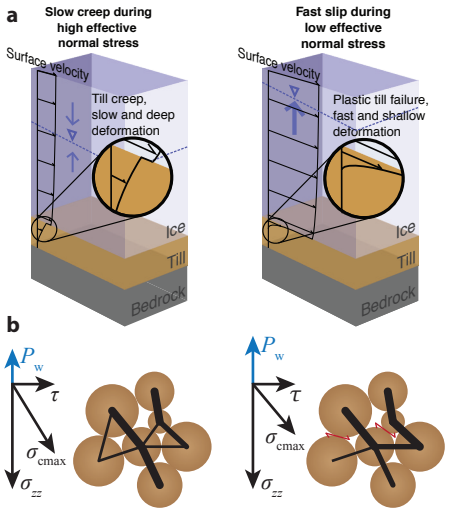

Figure 6.1. **A**, Schematic representation of two flow mechanisms caused by granular deformation in the glacier bed. The granular till-bed slowly creeps due to variations in pore-water pressure (left) or slips rapidly due to yield failure. Figure is not to scale. **B**, During creep variations in pore-water pressure (P_w) modify the direction and magnitude of the maximum compressive strength (σ_{cmax}), leading to small-scale reorganization and deformation in the granular force network.

envelope across materials and grain sizes (Damsgaard et al., 2013).

The external forcing, i.e. shear stress and pore-water variation, was calibrated to mimic realistic subglacial conditions where water pressure may vary at considerably shorter time-scales than shear stress. The shear stress was thus held constant at 10 kPa, while pore-water pressure at the top of the bed was forced to swing at an amplitude of 70 kPa. The pore-pressure modulation caused the effective normal stress to vary around a mean value of 80 kPa (Fig. 6.2A). All parts of the granular assemblage were free to move and accelerate at any rate dictated by the net force on each grain.

In our experiments, the granular bed showed highly non-linear velocity variations in response to the fluctuating effective pressure. Periods without any motion – stick events, when large and static force-chains stabilized the gain packing, were possible during times of maximum effective pressure and slow variation in pore-water pressure. In contrast, periods of complete slip, with rapid deformation of a thin boundary layer of grains, occurred when effective pressure was lowered enough to push the macroscopic yield stress below the externally imposed shear stress. Moreover, a key finding of our experiments was that the granular material showed significant creep in the periods between the stick-slip phases (Fig. 6.2B). The rate of creep decayed rapidly under constant-stress forcing, but continuous variations in effective pressure caused the orientation and magnitude of the maximum compressive stress to change correspondingly, which, in turn, required the grains to keep reorganizing in order to obtain a packing capable of supporting the new orientation of the principal stress (Fig. 6.1B). The grains thus responded

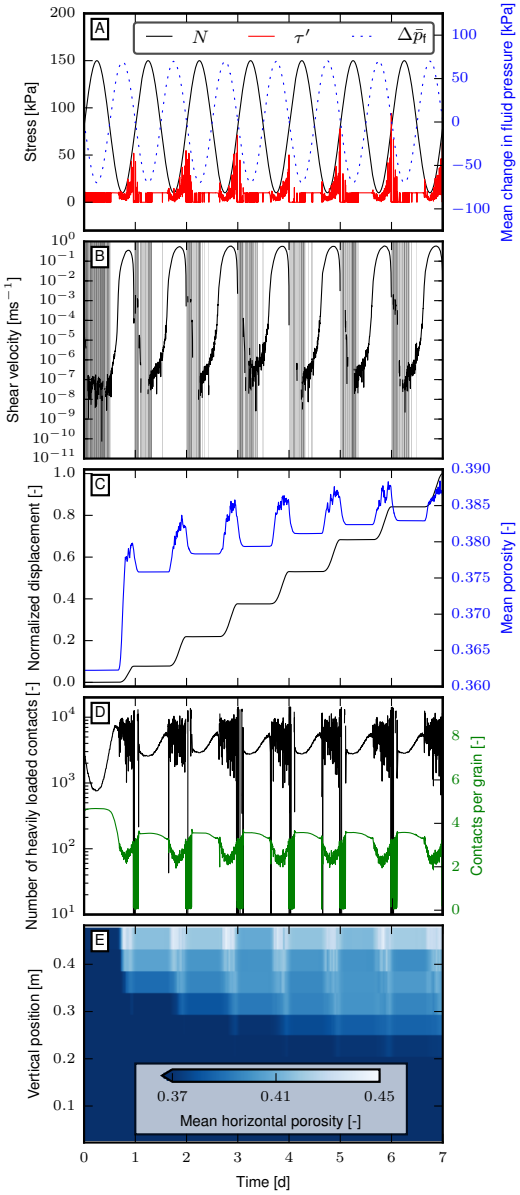

Figure 6.2. Granular dynamics in computational experiments forced by cyclic water pressure. **A**, Cyclic modulation in pore-water pressure (Δp_f) at the upper boundary alters the effective normal stress (N) in anti-phase by relieving the bed of a fraction of the ice overburden stress. The variation in normal stress causes regular fluctuations in the ratio between applied shear stress (τ) and effective normal stress. The stability of the granular assemblage is determined by this ratio (**B**), and it responds by 1) stick (gray vertical bars), 2) slow creep for low τ/N ratios, or 3) slip during high τ/N ratios. The irregular velocity pattern results in a step-wise displacement (**C**), where mean porosities are constant during creep and elevated during fast slip. The number of heavily loaded grain pairs increases as the effective normal stress decreases, while the mean number of contacts per particle decreases (**D**). The internal porosity is increased in areas of active deformation (**E**) and deepens over the course of several cycles.

to changes in stress forcing by inter-grain contact reorientation, grain rolling, or inter-grain sliding, when the contacts were unfavorably oriented relative to the principal stress. The contact reorganization sustained large creep velocities and a high level of porosity in the sediment, and the material did not consolidate to pre-failure packing under maximum effective pressure (Fig. 6.2C,E).

The finding of pre-failure creep in idealized granular materials contrasts the perfect plastic material rheology, where no deformation occurs at stress levels smaller than the yield strength. The combination of stick, creep and slip resulted in a stepped displacement history (Fig. 6.2C). Although creep rates in geotechnical materials are commonly assumed to decay with time (Kirkby, 1967; Terzaghi et al., 1996; Mitchell and Soga, 2005), our experiments suggest that continuous melt-water perturbations cause sustained internal grain rearrangement (Fig. 6.3), analogous to how hillslopes beneath the angle of repose experience downslope sediment movement due to moisture variations (Carson and Kirkby, 1972; Roering et al., 2001). The flow of slow-moving landslides is sensitive to transient stress perturbations such as variations in pore-water pressure by discrete precipitation events (Iverson and Major, 1987; Malet et al., 2002), or diurnal variations in pressure (Schulz et al., 2009).

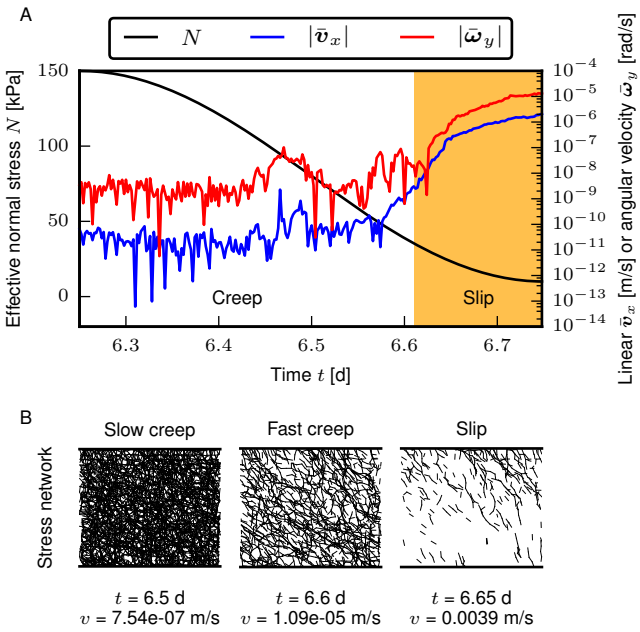

Figure 6.3. Granular dynamics in response to decreasing effective pressure. **A**, effective normal stress and grain movement. Grain rearrangement accelerates non-linearly as effective pressure drops. **B**, internal distribution of stress in different states of the granular material. The granular contact stress is mainly in the direction of the applied principal stress.

We have compared our model results with observations from a mountain glacier, an ice stream, and a landslide. The landslide does not involve glacier ice, but we

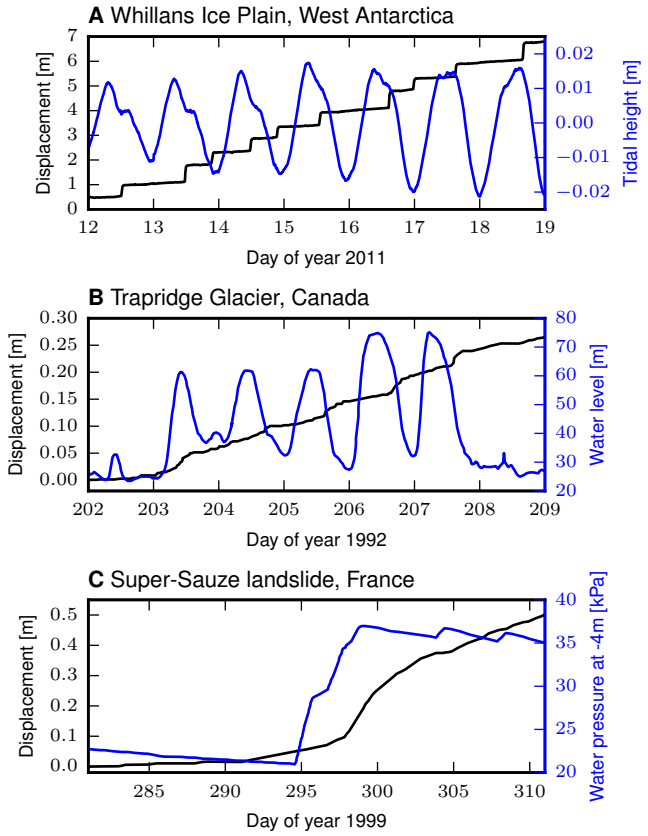

Figure 6.4. Creep and slip due to granular deformation induced by pore-pressure variation in two glacial systems (**A**, **B**) and an active landslide (**C**). All systems display slow but finite displacement during periods of low but variable water pressure, corresponding to the creep observed in our numerical simulations (Fig. 6.2B). Trapridge Glacier data from Fischer and Clarke (1997), Super-Sauze landslide data from Malet et al. (2002).

propose that aspects of landslide motion is caused by the same physical mechanisms as creep in the subglacial bed. Detailed information of the flow and hydraulic state is available for all three cases (Fig. 6.4). At Whillans Ice Plain, West Antarctica, tidewater variations induce flow oscillation (Fig. 6.4A, Bindschadler et al. (2003) and Winberry et al. (2011)). Similar displacement is observed at Trapridge Glacier, Yukon Territory, Canada (Fig. 6.4B, (Fischer and Clarke, 1997)), where surface melt drains through crevasses to the granular bed. The flow of the Super-Sauze landslide, Alpes-de-Haute-Provence, France (Fig. 6.4C, Malet et al. (2002)) is strongly linked to discrete precipitation events, which alter the internal water level. In all three settings non-linear granular strength causes flow to switch between fast slip and slow "stick". The slip phases correspond to plastic failure of the granular bed when hydraulic pressure exceeds a threshold value. Slow flow between slip events is likely caused by elastic loading and the granular creep mechanism presented here. While short-scale variations in pore-water pressure drive the granular creep, long-term changes in mean hydraulic pressure cause changes to average creep rates and influence the duration of the temporal window for slip (Beem et al., 2014). The extreme sensitivity of granular flows to the physical conditions highlights the importance of understanding the sediment mechanics during both slip and creep.

6.2 Supplementary Information

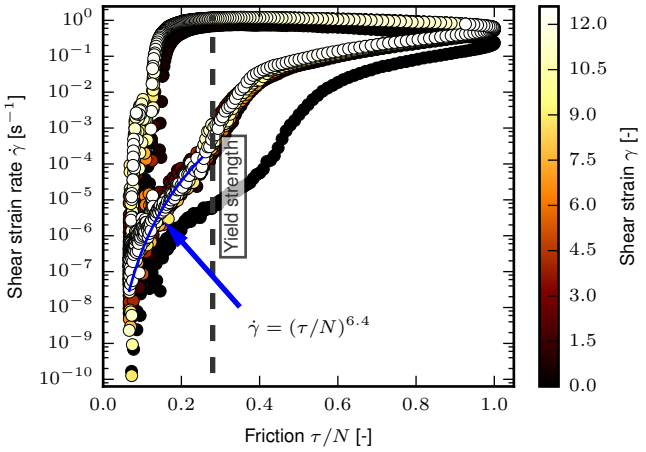

Figure 6.5. Relationship between applied shear stress, effective normal stress and shear strain rate. Below the plastic yield strength (dashed line) the granular material creeps with a non-linear viscous rheology, see fitted relationship in plot. Stressed above the plastic yield limit the material fails to increase its strength and the upper boundary accelerates, only limited by the inertia of its components.

Supplementary Methods

The grain and water mixture is simulated using two separate but coupled numerical models. The grains in the granular phase are simulated individually, and are interacting with each other and the pore-water fluid, as well as with the model boundaries. The fluid phase is treated as a visco-elastic continuum and flows according to Darcy's law.

The experimental setup is a cuboidal volume where the lateral boundaries are periodic, in effect giving a one-dimensional or horizontally pseudo-infinite geometry (Fig. 6.6). The granular assemblage is originally pre-consolidated and in a pre-failure state. The uppermost particles are moving uniformly and are imposing a modulating value of normal stress downwards and a constant shear stress along the positive direction of the x-axis. The fluid pressure is at the top boundary modulated according to the change in normal stress. The horizontal shear velocity at the top boundary is monitored as the stresses and fluid pressures evolve.

The novel computational approach allows for a precise movement of shear velocities far exceeding the resolution of sensors in laboratory devices. Additionally, the use of periodic lateral boundaries removes the effects of wall friction in most laboratory shear devices and strain thinning in direct-shear boxes. The numerical model produces true granular mechanics since no assumptions of macroscopic constitutive behavior is included. The purpose-built open-source modeling frame-

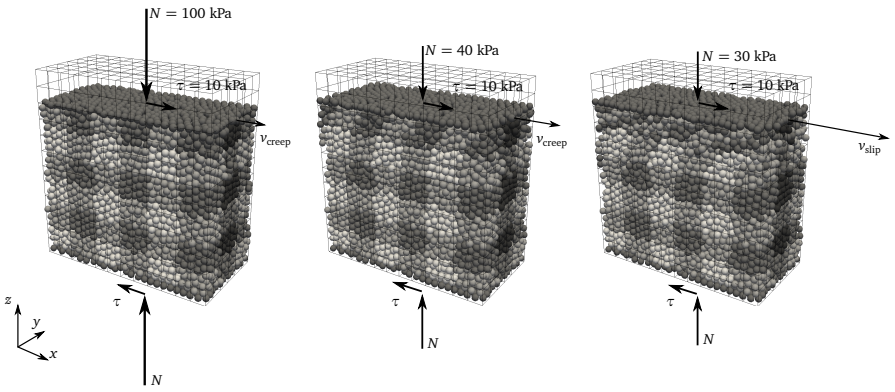

Figure 6.6. Experimental setup and deformation in the shear experiments.

work allows for experiment reproducibility and all model input files are available online.

The granular model imposes strict requirements to the time step length, however. In order to simulate a significant number of particles of realistic size with a quartz-like stiffness, we have implemented the granular and fluid algorithms in CUDA C (NVIDIA, 2013b) in order to accelerate the computations using NVIDIA GPUs[1]. The massive computational requirements force us to use mono-sized particles, since wider grain-size distributions increase contact search distances.

The stress variations caused larger creep rates at lower confining stress, because the average grain contact frictional strength was lower. Our experiments showed a distinctive and simple relationship between the applied shear stress, effective pressure, and creep rate (Fig. 6.6), depending on the amplitude and frequency of the pressure variation, resulting in stress exponent values between 6 and 11. The creep rates of our transient experiments are likely smaller than those of clay-rich materials in the same setting, since the presence of clay minerals is known to accelerate creep under steady forcings (Mitchell and Soga, 2005). Pore pressure variations are damped over distance in materials with low permeability, which leads to largest creep rates near subglacial channels.

Granular model

The grains are handled individually using the discrete element method(Cundall and Strack, 1979; Luding, 2008; Radjaï and Dubois, 2011; Damsgaard et al., 2013) (DEM). The grain shapes are idealized as spheres interacting using a linear elastic-frictional contact rheology. The surface forces resulting from the interaction between a pair of grains with indexes i and j are found as:

$$\boldsymbol{f}_{\mathrm{n}}^{\,i,j} = -k_{\mathrm{n}}\delta_{\mathrm{n}}^{\,i,j} \tag{6.1}$$

$$\boldsymbol{f}_{\mathrm{t}}^{\,i,j} = -\max\{k_{\mathrm{t}}||\boldsymbol{\delta}_{\mathrm{t}}^{\,i,j}||, \mu||\boldsymbol{f}_{\mathrm{n}}^{\,i,j}||\}\frac{\boldsymbol{\delta}_{\mathrm{t}}^{\,i,j}}{||\boldsymbol{\delta}_{\mathrm{t}}^{\,i,j}||} \tag{6.2}$$

[1] https://github.com/anders-dc/sphere

k is the elastic stiffness of the grain material. The magnitude of the tangential force is limited by the Coulomb criterion, where the coefficient μ describes the frictional limit. $\boldsymbol{\delta}_{\mathrm{n}}$ is the inter-grain overlap vector and $\boldsymbol{\delta}_{\mathrm{t}}$ is the cumulative movement on the contact plane. The overlap vector is found as (Luding, 2008; Hinrichsen and Wolf, 2004):

$$\delta_{\mathrm{n}}{}^{i,j} = \boldsymbol{x}^j - \boldsymbol{x}^i - (r^i + r^j) \tag{6.3}$$

$\boldsymbol{x}$ is the position of the grain center and r is the grain radius. The uncorrected total displacement on the contact plane ($\boldsymbol{\delta}_{\mathrm{t}^*}^{i,j}$) is found by integrating the displacements from each time step for the duration of the contact t_c (Luding, 2008; Hinrichsen and Wolf, 2004):

$$\boldsymbol{\delta}_{\mathrm{t}^*}^{i,j} = \int_{t_c} \left[\dot{\boldsymbol{x}}^i - \dot{\boldsymbol{x}}^j + \left(r^i + \frac{||\delta_{\mathrm{n}}{}^{i,j}||}{2} \right) \boldsymbol{n}^{i,j} \times \dot{\boldsymbol{\Omega}}^i + \left(r^j + \frac{||\delta_{\mathrm{n}}{}^{i,j}||}{2} \right) \boldsymbol{n}^{i,j} \times \dot{\boldsymbol{\Omega}}^j \right] \tag{6.4}$$

$\dot{\boldsymbol{x}}$ is the linear grain velocity, and $\dot{\boldsymbol{\Omega}}$ is the angular grain velocity. $\boldsymbol{n}$ is the contact plane normal vector. The vector of displacement on the tangential plane ($\boldsymbol{\delta}_{\mathrm{t}}$) is corrected for contact rotation (Hinrichsen and Wolf, 2004):

$$\boldsymbol{\delta}_{\mathrm{t}}^{i,j} = \boldsymbol{\delta}_{\mathrm{t}^*}^{i,j} - \boldsymbol{n}^{i,j} \left(\boldsymbol{n}^{i,j} \cdot \boldsymbol{\delta}_{\mathrm{t}^*}^{i,j} \right) \tag{6.5}$$

If the frictional limit on the contact is exceeded ($k_{\mathrm{t}} \boldsymbol{\delta}_{\mathrm{t}} > \mu \boldsymbol{f}_{\mathrm{n}}$, Eq. 6.2), the displacement vector on the contact plane ($\boldsymbol{\delta}_{\mathrm{t}}$) is adjusted to a length consistent with Coulomb's condition (Luding, 2008; Radjaï and Dubois, 2011):

$$\boldsymbol{\delta}_{\mathrm{t}}^{i,j} \equiv \frac{\mu ||\boldsymbol{f}_{\mathrm{n}}^{i,j}||}{k_{\mathrm{t}}} \frac{\boldsymbol{\delta}_{\mathrm{t}}^{i,j}}{||\boldsymbol{\delta}_{\mathrm{t}}^{i,j}||} \tag{6.6}$$

The grains are forced by the pore water through fluid-pressure gradients. Grains are attracted to volumes of low fluid pressures and repelled from high pressures:

$$\boldsymbol{f}_{\mathrm{f}} = -V_{\mathrm{g}} \nabla p_{\mathrm{f}} - \rho_{\mathrm{f}} V_{\mathrm{g}} \boldsymbol{g} \tag{6.7}$$

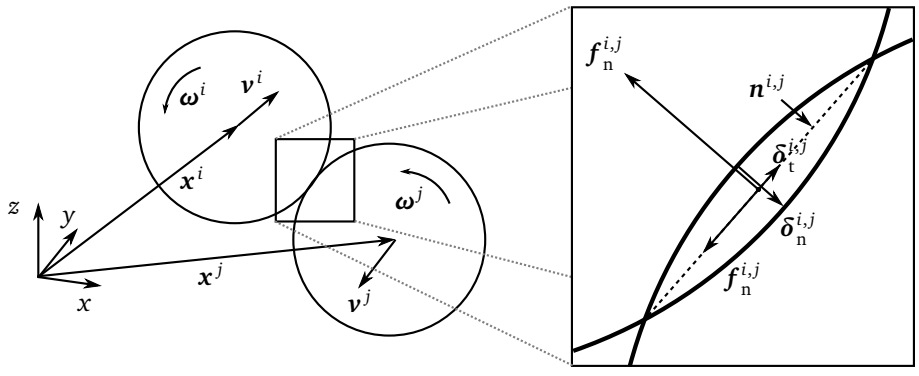

Figure 6.7. Two-dimensional schematic of an inter-grain contact. The size of the grain overlap on the right is exaggerated. The grain contact forces ($\boldsymbol{f}_{\mathrm{n}}$ and $\boldsymbol{f}_{\mathrm{t}}$) are surface forces while the gravitational pull ($\boldsymbol{f}_{\mathrm{g}}$) and fluid forces ($\boldsymbol{f}_{\mathrm{f}}$) are body forces.

V_g is the grain volume, ρ_f is the fluid density and $\boldsymbol{g}$ is the gravitational acceleration vector. The latter term is the uplift caused by buoyancy. Other known interaction forces between fluids and submerged grains include drag force, lift forces caused by fluid velocity gradients (Saffman force), torques due to grain rotation (Magnus force), and interaction forces due to grain acceleration (virtual mass force) (Zhou et al., 2010). These forces are negligible in our experiments of low fluid velocities, and are therefore not included.

Once all surface and body force components for all grains are found, they are summed to give the total linear force and torque. For a grain i which has a set of contacts (N) the resulting force ($\boldsymbol{F}$) and torque ($\boldsymbol{T}$) is:

$$\boldsymbol{F}^i = \boldsymbol{f}_g^i + \sum_{j \in N} \left(\boldsymbol{f}_t^{i,j} + \boldsymbol{f}_n^{i,j} \right) + \boldsymbol{f}_f^i \tag{6.8}$$

$$\boldsymbol{T}^i = \sum_{j \in N} \left(- \left(r^i + \frac{||\boldsymbol{\delta}_n^{i,j}||}{2} \right) \boldsymbol{n}^{i,j} \times \boldsymbol{f}_t^{i,j} \right) \tag{6.9}$$

$\boldsymbol{f}_g$ is the gravitational force, r is the grain radius and $\boldsymbol{n}$ is the contact normal vector. Finally the new linear accelerations ($\boldsymbol{a}$), velocities ($\boldsymbol{v}$), and positions ($\boldsymbol{x}$) and angular accelerations ($\boldsymbol{\alpha}$), velocities ($\boldsymbol{\omega}$) and positions ($\boldsymbol{\Omega}$) for each grain are found by explicitly integrating Newton's second law ($\boldsymbol{F} = m\ddot{\boldsymbol{x}}$) in time. This is done with higher-order Taylor expansions which ensure a precise solution (Kruggel-Emden et al., 2008):

$$\ddot{\boldsymbol{x}}_t^i = \frac{\boldsymbol{F}_t^i}{m^i} \tag{6.10}$$

$$\dot{\boldsymbol{x}}_{t+\Delta t}^i = \dot{\boldsymbol{x}}_t^i + \ddot{\boldsymbol{x}}_t^i \Delta t + \frac{1}{2} \frac{\ddot{\boldsymbol{x}}_t^i - \ddot{\boldsymbol{x}}_{t-\Delta t}^i}{\Delta t} \Delta t^2 \tag{6.11}$$

$$\boldsymbol{x}_{t+\Delta t}^i = \boldsymbol{x}_t^i + \dot{\boldsymbol{x}}_t^i \Delta t + \frac{1}{2} \ddot{\boldsymbol{x}}_t^i \Delta t^2 + \frac{1}{6} \frac{\ddot{\boldsymbol{x}}_t^i - \ddot{\boldsymbol{x}}_{t-\Delta t}^i}{\Delta t} \Delta t^3 \tag{6.12}$$

$$\ddot{\boldsymbol{\Omega}}_t^i = \frac{\boldsymbol{T}_t^i}{m^i} \tag{6.13}$$

$$\dot{\boldsymbol{\Omega}}_{t+\Delta t}^i = \dot{\boldsymbol{\Omega}}_t^i + \ddot{\boldsymbol{\Omega}}_t^i \Delta t + \frac{1}{2} \frac{\ddot{\boldsymbol{\Omega}}_t^i - \ddot{\boldsymbol{\Omega}}_{t-\Delta t}^i}{\Delta t} \Delta t^2 \tag{6.14}$$

$$\boldsymbol{\Omega}_{t+\Delta t}^i = \boldsymbol{\Omega}_t^i + \dot{\boldsymbol{\Omega}}_t^i \Delta t + \frac{1}{2} \ddot{\boldsymbol{\Omega}}_t^i \Delta t^2 + \frac{1}{6} \frac{\ddot{\boldsymbol{\Omega}}_t^i - \ddot{\boldsymbol{\Omega}}_{t-\Delta t}^i}{\Delta t} \Delta t^3 \tag{6.15}$$

The granular model imposes strict requirements to the time step length. The time step length is selected in order to resolve seismic propagation of elastic waves through the smallest grains in the granular phase (Radjaï and Dubois, 2011):

$$\Delta t = \frac{\epsilon}{\sqrt{\frac{\max(k_n, k_t)}{\min(m)}}} \tag{6.16}$$

ϵ is a safety factor, here we use a value of 0.07. The constant elasticity in the inter-grain contact model allow us to use a constant time step length. The time step for the presented experiments has a value in the order of 10^{-7} s. Computational

requirements increase with the number of particles, their stiffness, and decreases with grain mass and, in turn, grain size. Additionally, the computationally intensive inter-grain contact search favors narrow grain-size distributions in terms of computational time.

Pore-water model

The pore water is treated as a compressible Newtonian fluid without inertia (Goren et al., 2010; Goren et al., 2011). The temporal evolution of pore-fluid pressure ($\partial p_\mathrm{f}/\partial t$) is governed by spatial diffusion of pore-fluid pressure (p_f), which takes place according to Darcy's law, and by being forced through local changes in porosity (ϕ) through time ($\partial\phi/\partial t$):

$$\frac{\partial p_\mathrm{f}}{\partial t} = \underbrace{\frac{1}{\phi\beta_\mathrm{f}\mu_\mathrm{f}}\left(k\nabla^2 p_\mathrm{f} + \nabla p_\mathrm{f}\cdot\nabla k\right)}_{\text{Spatial diffusion}} \overbrace{-\frac{1}{\beta_\mathrm{f}\phi(1-\phi)}\left(\frac{\partial\phi}{\partial t} + \bar{\boldsymbol{v}}\cdot\nabla\phi\right)}^{\text{Grain forcing}} \tag{6.17}$$

The fluid rheology is determined by the adiabatic compressibility (β_f) and dynamic viscosity (μ_f). The granular forcing term corrects for spatial diffusion of porosity. $\bar{\boldsymbol{v}}$ is the average local grain velocity. Note that the above equation describes the pressure deviation from the hydrostatic value. The local intrinsic permeability (k) is prescribed by a Kozeny-Carman type relationship which scales permeability with porosity (Hazen, 1911; Kozeny, 1927; Carman, 1937; Harleman et al., 1963; McNamara et al., 2000; Goren et al., 2011):

$$k = k_\mathrm{c}\frac{\phi^3}{(1-\phi)^2} \tag{6.18}$$

The local porosity is determined at the fluid cell center. We use a homogeneous cubic spatial discretization with cell side length Δx. For a cell with a set of N grains in its vicinity, it is determined by inverse-distance weighing the grains (Fig. 6.8) (McNamara et al., 2000; Goren et al., 2011): The weight function s is 1 at the cell center and linearly decreases to 0 at a distance of Δx (Fig. 6.8):

$$\phi(\boldsymbol{x}_\mathrm{f}) = 1 - \frac{\sum_{i\in N} s(\boldsymbol{x}^i - \boldsymbol{x}_\mathrm{f})V_\mathrm{g}^i}{\Delta x^3} \tag{6.19}$$

$$s(\boldsymbol{x}^i - \boldsymbol{x}_\mathrm{f}) = \begin{cases} \Pi_{d=1}^3\left[1 - \frac{|\boldsymbol{x}_d^i - \boldsymbol{x}_{\mathrm{f},d}|}{\Delta x}\right] & \text{if } |\boldsymbol{x}_1^i - \boldsymbol{x}_{\mathrm{f},1}|, |\boldsymbol{x}_2^i - \boldsymbol{x}_{\mathrm{f},2}|, |\boldsymbol{x}_3^i - \boldsymbol{x}_{\mathrm{f},3}| < \Delta x \\ 0 & \text{otherwise} \end{cases} \tag{6.20}$$

Δx^3 is the fluid cell volume, and $\boldsymbol{x}_\mathrm{f}$ is the cell center position. The average grain velocity at the cell center is found using the same weighting function described above (eq. 6.20). Additionally, large grains contribute to the velocity with a greater magnitude:

$$\bar{\boldsymbol{v}}(\boldsymbol{x}_\mathrm{f}) = \frac{\sum_{i\in N} s(\boldsymbol{x}^i - \boldsymbol{x}_\mathrm{f})V_\mathrm{g}^i\boldsymbol{v}^i}{\sum_{i\in N} s(\boldsymbol{x}^i - \boldsymbol{x}_\mathrm{f})} \tag{6.21}$$

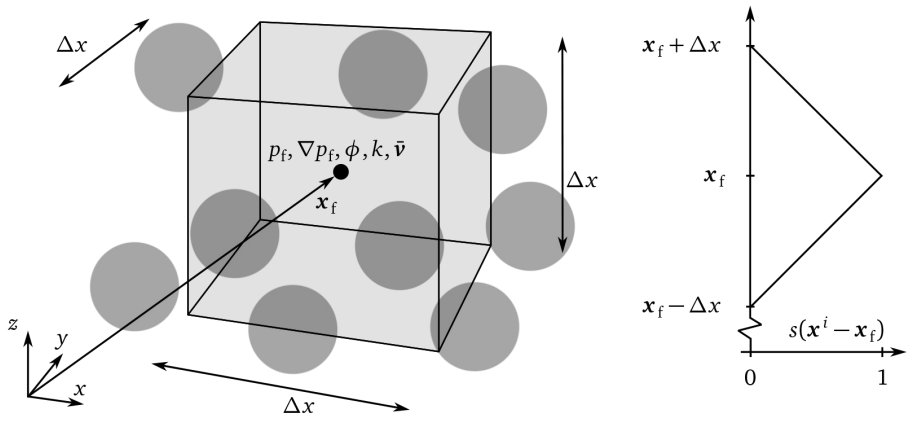

Figure 6.8. Left: A cell in the fluid grid. The node for pressure (p_f), the gradient of fluid pressure (∇p_f), porosity (ϕ), permeability (k), and average grain velocity ($\bar{v}$) is located at the cell center. Right: The weighing function (eq. 6.20) at various distances.

The temporal gradient in porosity is approximated with a central-difference scheme, where the future porosity is found by predicting grain positions at $t + \Delta t$.

$$\frac{\partial \phi}{\partial t} \approx \frac{\phi_{t+\Delta t} - \phi_{t-\Delta t}}{2\Delta t} \tag{6.22}$$

The fluid pressures (eq. 6.17) are integrated using the Crank-Nicolson method of mixed explicit and implicit temporal integration (Patankar, 1980; Ferziger and Perić, 2002; Press et al., 2007). The implicit solution is found with the iterative Jacobi relaxation method (Ferziger and Perić, 2002; Press et al., 2007). The solution is unconditionally stable and second-order accurate in time and space. We use the same time step length that is used for the granular computations (eq. 6.16) in order to fully resolve the fluid-grain interaction.

Simulation Parameter Values

The applied geometric and physical parameter values are listed in supplementary table (tab. 6.1). Noteworthy parameter choices are elaborated in the following.

Boundary conditions

The lower boundary is impermeable, and a fixed fluid pressure is prescribed at the top boundary. The grains at the lower boundary are fixed in space while the upper grains apply a constant shear stress. The upper grains are loaded downwards by a wall which exerts a prescribed normal stress. The wall and upper grains are free to move up and down as long as the normal stress condition is satisfied, allowing for granular volumetric changes. The lateral boundaries are for both the grains and fluid periodic (wrap-around). If a grain moves outside the grid it reappears at the opposite boundary. Likewise, grains can be in mechanical contact although placed on opposite sides of the grid at the periodic boundaries.

Table 6.1. Parameters used for the computational experiments.

Parameter	Symbol	Value
Particle count	N_p	9600
Particle radius	r	0.01 m
Particle normal stiffness	k_n	1.16×10^9 N m^{-1}
Particle tangential stiffness	k_t	1.16×10^9 N m^{-1}
Particle friction coefficient	μ	0.5
Particle density	ρ	2600 kg m^{-3}
Fluid density	ρ_f	1000 kg m^{-3}
Fluid dynamic viscosity	μ_f	1.040×10^{-6} Pa s
Fluid adiabatic compressibility	β_f	1.426×10^{-8} Pa^{-1}
Hydraulic permeability prefactor	k_c	3.5×10^{-13} m^3
Mean prescribed normal stress	$\bar{N}$	80 kPa
Normal stress modulation amplitude	A_N	70 kPa
Normal stress modulation frequency	f_N	0.2 Hz
Prescribed shear stress	τ	10 kPa
Top wall mass	m_w	280 kg
Gravitational acceleration	$\boldsymbol{g}$	[0, 0, −9.81] m s^{-2}
Spatial domain dimensions	$\boldsymbol{L}$	[0.52, 0.26, 0.55] m
Fluid grid size	$\boldsymbol{n}$	[12, 6, 12]
Time step length	Δt	2.14×10^{-7} s
Simulation length (scaled time)	t_end	35 s

Scaling of model time: 1. Granular model

Granular materials have the intrinsic ability to change phase (e.g. Jaeger et al., 1996; Herrmann, 2002). Depending on the average kinetic energy and the packing density (or porosity) of the grains, they can behave solid-like, fluid-like or gaseous. The material rheology undergoes drastic changes along the phase thresholds, where the overall strength, rate dependence, and packing density changes (e.g. GDR-MiDi, 2004; Krimer et al., 2012).

Under slow shear velocities and a confining normal stress, the rheology of dry and dense granular materials is generally strain-rate independent. The mechanical behavior of granular materials is a consequence of the inter-grain contact rheology and the self-organizing complexity of the arrangement of grains. If the granular material deforms under higher shearing velocities, grain inertia becomes important and deformation becomes rate dependent (*Bagnold flow*) (Zhang and Campbell, 1992; Aharonov and Sparks, 1999; Aharonov and Sparks, 2002; Campbell, 2006; Krimer et al., 2012). GDR-MiDi (2004) is a review of experimental and numerical results of the solid-fluid transition, where a dimensionless inertia parameter I in confined two-dimensional planar shear experiments is constituted of:

$$I = \dot{\gamma}\bar{r}\sqrt{\frac{\rho}{N}} \tag{6.23}$$

$\dot{\gamma}$ is the shear strain rate, $\bar{r}$ is the mean grain radius, ρ is the material density, and N is the magnitude of the normal stress. Experiments show that the dry granular materials deform in a pseudo-static and rate-independent manner when $I < 10^{-3}$ (GDR-MiDi, 2004; Krimer et al., 2012).

As the average kinetic energy of the grains increases, the average duration of inter-grain contacts decreases. In the dense state under constant stress forcing,

grains spend the majority of time in a force-balanced configuration in contact with each other or other rigid objects. The other end-member state, known from sand storms and abrasive blasting, is the gaseous domain where inter-grain contacts are few and short-lived. The fluid state lies between the end-member gas and solid states, where packing density still is relatively large but grain inertia significantly influences the dynamics and duration of grain contacts.

The inertia equation above (Eq. 6.23) implies that the ratio between grain kinetic energy and packing density controls the transition from the pseudo-static state, where grains are close to force equilibrium, to fluid behavior, where grain inertia significantly influences contact duration. The average kinetic energy or inertia of the actively deforming parts can be altered by varying the applied shear velocity or the grain mass. The confining stress, N, on the other hand condenses the granular assemblage, where the contact network loading at high values overpowers relative grain movement due to inertia.

Grain contact model

The grains in our numerical model are interacting using a linear elastic-frictional contact rheology, commonly used in discrete element models (e.g. Cundall and Strack, 1979; Aharonov and Sparks, 1999; Aharonov and Sparks, 2002; Goren et al., 2011; Damsgaard et al., 2013). We have chosen not to include viscous dashpots in the inter-grain contact model. The damping effect of quartz viscosity is negligible at the considered temperatures (Gleason and Tullis, 1995) and is often only introduced to dampen numerical oscillations. A loaded contact (Fig. 6.9) has in our formulation no rate-dependent viscous components, which act to strengthen or weaken the contact over time. This implies no relative movement of a pair of grains at force balance under steady conditions.

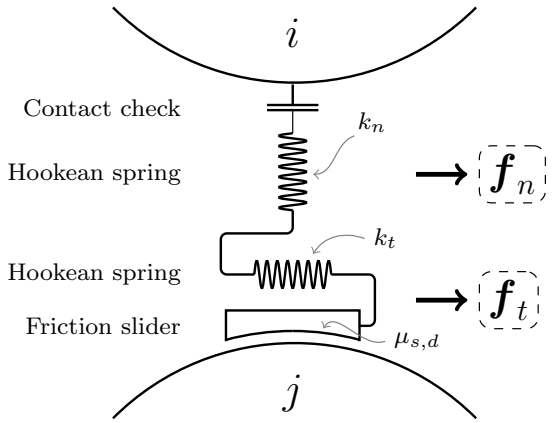

Figure 6.9. Schematic of the mechanical components of an inter-grain contact, normal and tangential to the contact interface plane. From Damsgaard et al. (2013).

Computational requirements

The explicit integration scheme (eq. 6.10 to 6.15) is typical for soft-body discrete element methods, and poses strict requirements to the time step length in order to ensure numerical stability. The time step needs to allow sufficient resolution of seismic propagation of elastic waves through the smallest grains in the granular phase (Radjaï and Dubois (2011), Eq. 6.16). The mass of the smallest particle ($\min(m)$) scales with particle size and density. ϵ is a safety factor, here with a value of 0.07. The used grain size (grain radius $r = 1\,\mathrm{cm}$), grain material density ($\rho = 2600\,\mathrm{kg\,m^{-3}}$) and contact stiffness ($k_\mathrm{n} = k_\mathrm{t} = 1.16 \times 10^9\,\mathrm{N\,m^{-1}}$) results in a time step of $\Delta t = 2.14 \times 10^{-7}\,\mathrm{s}$. For a simulation length of 35 s this results in approximately 10^8 time steps and a computation time of 70 days. We have chosen a large grain size but a quartz-like stiffness since this results in correct porosity evolution during deformation. Lowering the density is also a popular way to increase the computational time step. In our experience this can lead to volatile behavior since particles are more easily accelerated.

Velocity scaling

Glacier sliding velocities are highly variable, ranging from zero up to ten meters per day (Cuffey and Paterson, 2010). Ice streams generally accelerate down flow, and the West Antarctic Whillans ice stream on a temporal average flows at velocities of $400\,\mathrm{m\,a^{-1}}$ to $800\,\mathrm{m\,a^{-1}}$ (Alley and Whillans, 1991), equivalent to $1.3 \times 10^{-5}\,\mathrm{m\,s^{-1}}$ to $2.5 \times 10^{-5}\,\mathrm{m\,s^{-1}}$.

The strict time step requirements for the soft-body discrete element method (eq. 6.16) require we scale model time. The granular behavior is rate-independent as long as $I < 10^3$ (eq. 6.23), which is satisfied in the creep phases. This value, together with the rate-independent contact model (fig. 6.9), ensures rate-independence of shear stress and dilation in the granular phase and allows for temporal scaling.

Scaling of model time: 2. Fluid model

The model time is in the granular model upscaled as described in the previous section. The time scaling necessitates considerations of the model time in the fluid algorithm. There are two possibilities:

1. Use scaled model time for the granular phase and real time for the fluid model. The grain forcing terms in the fluid equation 6.17 ($\partial\phi/\partial t$ and $\bar{\boldsymbol{v}}$) are scaled by the time scaling factor used in the DEM.

2. Use scaled model time for the granular phase and scaled time for the fluid model. This requires that the spatial diffusion term in the fluid equation 6.17 is scaled by the time scaling factor used in the DEM.

Option 1 works by forcing the fluid with much slower rates, but simulating fluid behavior over a realistic time span. Option 2 works by enhancing the fluid ability to compensate against forcings from the granular phase or from the boundaries. We chose option 2 since the implementation is more straight-forward.

The spatial diffusion can be scaled by either adjusting the permeability k or the dynamic fluid viscosity μ_f. The hydraulic diffusivity has the units $\mathrm{m^2\,s^{-1}}$ and is first order dependent on time. We chose to adjust the fluid viscosity since it is a time-dependent parameter (Pa s) and we could use realistic permeability values. Since

fluid viscosity has a first order influence on hydraulic diffusivity, we can use the same scaling factor value used in the DEM. Water at 0 °C has a dynamic viscosity of 1.797×10^{-3} Pa s. Consistent with the time scaling factor from the granular model, we use a dynamic viscosity of 1.797×10^{-6} Pa s. The decreased viscosity makes it faster to adapt to internal and external changes.

Chapter 7

Research note 1: *Discrete element modeling: Methodology and example*

This chapter is intended to expand on the fundamental design choices and implementation details for the granular phase numerical model used for this thesis. Finally, a simplified pseudo-code example demonstrates the basics of the discrete element method.

The full source code used for the simulations in this thesis is available at `https://github.com/anders-dc/sphere`.

7.1 Introduction

DEM modeling is a Lagrangian-type numerical implementation of multibody classical mechanics. The soft-body DEM formulation was derived from molecular dynamics (MD) by Cundall and Strack (1979), who drew parallels between simulation of geomaterials and already established algorithms used to simulate molecule behavior.

Newton's laws of motion are applied to individual interacting bodies. Newton's second law states that the acceleration of a body ($\ddot{\boldsymbol{x}}$) with constant mass (m) is proportional to the total body force ($\boldsymbol{F}$):

$$\boldsymbol{F} = m\ddot{\boldsymbol{x}} \quad \Rightarrow \quad \ddot{\boldsymbol{x}} = \frac{\boldsymbol{F}}{m} \tag{7.1}$$

This proportionality implies that if the sum of forces on a grain is known, the resultant acceleration in space can be found. The acceleration causes a change in velocity and position, which are found through temporal integration. The same principles can be applied to the rotational degrees of freedom, where the rotational acceleration ($\ddot{\boldsymbol{\Omega}}$) is proportional to the sum of torques ($\boldsymbol{T}$),

$$\boldsymbol{T} = I\ddot{\boldsymbol{\Omega}} \quad \Rightarrow \quad \ddot{\boldsymbol{\Omega}} = \frac{\boldsymbol{T}}{I} \tag{7.2}$$

here I is the moment of inertia. The kinematic behavior of solid-mass bodies is found by determining the sum of body and surface forces acting on each entity. Body forces contribute to the total force $\boldsymbol{F}$, while surface forces can contribute both to the total body force and the sum of torques $\boldsymbol{T}$. An example body force is the gravity force, which can be expressed as a force pulling an object from its center of mass. Granular contact forces can cause both linear and rotational movement, dependent on the relative movement of the grains. The total force $\boldsymbol{F}$ and total torque $\boldsymbol{T}$ for grain i is found by:

$$\boldsymbol{F}^i = \underbrace{\sum_{j \in n_c} \left(\boldsymbol{f}_{\mathrm{n}}{}^{i,j} + \boldsymbol{f}_{\mathrm{t}}{}^{i,j} \right)}_{\text{contact forces}} + \boldsymbol{f}_{\mathrm{g}} + \dots \tag{7.3}$$

$$\boldsymbol{T}^i = \underbrace{\sum_{j \in n_c} \left(-r^i \boldsymbol{n}^{i,j} \times \boldsymbol{f}_{\mathrm{t}}{}^{i,j} \right)}_{\text{contact torques}} \tag{7.4}$$

where $\boldsymbol{f}_{\mathrm{g}} = m\boldsymbol{g}$ is the gravitational force, and $\boldsymbol{n}$ is the contact normal unit vector.

Soft-body DEM solve Eq. 7.1 through time, determining continuous velocity and position evolution of the multibody system. The rigid-body (or non-smooth) DEM formulations such as *contact dynamics* ignore the small time scales associated with grain elasticity. Velocities are discontinuous through time (hence the non-smooth name), and the solution procedure is an iterative process mapping the network of contacts. For a comprehensive review of the solution procedure, the reader is referred to Radjaï and Dubois (2009) and Radjaï and Dubois (2011). In this study we chose to use the soft-body formulation, in part due to its inclusion of elastic deformation and in part due to its inclusion of processes relevant on all time scales (Hinrichsen and Wolf, 2004).

7.2 Contact model components

Normal force

The normal force denotes the repulsive response when a set of grains are compressed together. It is acting in a *normal* direction relative to the contact plane between two particles. These forces may be attractive as surface tension of water droplets in unsaturated materials pulls grains together. In saturated granular materials, normal forces short of the repulsive elastic deformation force are negligible, however.

In the soft-body formulation, a pair of grains are in contact when their separation distance δ_n is less or equal to 0. The overlap of grain volumes causes a repulsive force, which for spherical particles points from the center of the contact point towards the grain center, making it a body force.

A simple formulation for the contact-normal force is the linear-elastic formulation, where overlap causes a linear-elastic reaction force, scaled by the Hookean contact stiffness k_n (Cundall and Strack, 1979; Kruggel-Emden et al., 2007; Radjaï and Dubois, 2009; Damsgaard et al., 2013):

$$\boldsymbol{f}_\mathrm{n} = -k_\mathrm{n}\delta_\mathrm{n}\boldsymbol{n} \tag{7.5}$$

Instead of a linear spring, the normal force is sometimes considered a non-linear Hertz force (Hertz, 1882; Johnson, 1985; Kruggel-Emden et al., 2007; Radjaï and Dubois, 2009):

$$\boldsymbol{f}_\mathrm{n} = -\frac{E\sqrt{2r}}{3(1-\nu^2)}{\delta_\mathrm{n}}^{3/2}\boldsymbol{n} \tag{7.6}$$

E is Young's modulus and ν is Poisson's ratio of the grain. The contact stiffness increases with contact loading, and the time step length Δt must be adjusted accordingly for the explicit integration scheme to retain stability.

The examples of normal force laws above describe the contact as perfectly elastic, implying that total kinetic energy is conserved after a collision. Grains tend to clustering in granular gases because a fraction of their kinetic energy is lost during collisions (e.g. Jaeger and Nagel, 1992; Jaeger et al., 1996). The energy dissipation can be implemented in a number of ways, by e.g. adding a dash-pot with viscosity γ_n to the grain contact rheology:

$$\boldsymbol{f}_\mathrm{n} = {\boldsymbol{f}_\mathrm{n}}^{\mathrm{elastic}} + \gamma_\mathrm{n}\dot{\delta}_\mathrm{n} \tag{7.7}$$

The dash-pot viscosity causes a clear rate-dependence on the contact, however. Infinitely long grain collisions are perfectly elastic while fast collisions contain significant damping. Consequently, the property of this parameter is difficult to justify physically and experimentally deduce. It is however often used in DEM models since it dampens numerical oscillations. Alternatively, the model can lose kinetic energy through a hysteric contact model (Walton and Braun, 1986; Kruggel-Emden et al., 2007), where the elastic stiffness coefficient is lower when the grains are separating than when they are moving closer:

$$\boldsymbol{f}_\mathrm{n} = \begin{cases} -k_\mathrm{n}\delta_\mathrm{n}\boldsymbol{n}, & \text{if } \dot{\delta}_\mathrm{n} \leq 0 \\ -ck_\mathrm{n}\delta_\mathrm{n}\boldsymbol{n}, & \text{if } \dot{\delta}_\mathrm{n} > 0 \end{cases} \tag{7.8}$$

where $c \in]0;1[$. The loss of kinetic energy through the hysteric contact model is mainly applicable to high-energy kinetic granular assemblies with short-lived inter-grain contacts. In dense and loaded granular assemblies it can amplify oscillatory behavior because the force is non-smooth around $\dot{\delta}_{\mathrm{n}} = 0$.

Tangential force

The interaction between two grains can result in forces parallel to the inter-grain contact interface, known as *tangential forces*. These forces can result in torques leading to rotation. The tangential forces also increase the strength of the contact, and are often limited by the Coulomb criterion of friction.

The tangential force origins from relative movement of the surfaces of the grains in contact. If a non-rotating particle collides with a flat surface, the tangential forces accelerate rotational movement for the duration of the collision. The tangential forces also constitute one of the main controls on the macroscopic shear strength of granular assemblies.

The simplest way to include tangential forces is to scale it with relative grain surface velocity $\dot{\boldsymbol{\delta}}_{\mathrm{t}}$, which for two grains i and j with rotational velocities $\dot{\boldsymbol{\Omega}}$ can be expressed as:

$$\dot{\boldsymbol{\delta}}_{\mathrm{t}} = \dot{\boldsymbol{x}}^{i} - \dot{\boldsymbol{x}}^{j} + r_{i}\boldsymbol{n}_{i,j} \times \dot{\boldsymbol{\Omega}}_{i} + r_{j}\boldsymbol{n}_{i,j} \times \dot{\boldsymbol{\Omega}}_{j} \tag{7.9}$$

The above formulation ignores the minor change in grain radius caused by elastic grain deformation. The velocity parallel to the contact plane can scale the resultant force through grain viscosity:

$$\boldsymbol{f}_{\mathrm{t}} = \gamma_{\mathrm{t}}\dot{\boldsymbol{\delta}}_{\mathrm{t}} \tag{7.10}$$

The viscous formulation of tangential strength has the implication that the shear strength of a grain-contact is dependent on rate. A better approach is to use an elastic tangential force, which scales force with displacement:

$$\boldsymbol{f}_{\mathrm{t}} = k_{\mathrm{t}}\boldsymbol{\delta}_{\mathrm{t}} \tag{7.11}$$

The value of tangential contact velocity $\dot{\boldsymbol{\delta}}_{\mathrm{t}}$ used in the viscous tangential contact law is trivial to find, as it solely depends on current grain velocities (Eq. 7.9). In order to determine the tangential displacement $\boldsymbol{\delta}_{\mathrm{t}}$, the velocities are integrated to displacements over the duration of the contact t_{c}, which involves many time steps:

$$\boldsymbol{\delta}_{\mathrm{t}} = \int_{t_{\mathrm{c}}} \dot{\boldsymbol{\delta}}_{\mathrm{t}} \tag{7.12}$$

In order to achieve the tangential displacement, the DEM algorithm needs to contain bookkeeping able to identify and save contacts for arbitrary lengths of time.

The tangential force is usually limited by the Coulomb criterion, stating that the tangential force magnitude cannot exceed some fraction (μ_{s}) of the normal force magnitude:

$$||\boldsymbol{f}_{\mathrm{t}}|| \leq \mu_{\mathrm{s}}||\boldsymbol{f}_{\mathrm{n}}|| \tag{7.13}$$

7.3 Contact detection

A common requirement for particle-based numerical methods with interaction laws dependent on inter-particle spacing is the mapping of neighboring entities.

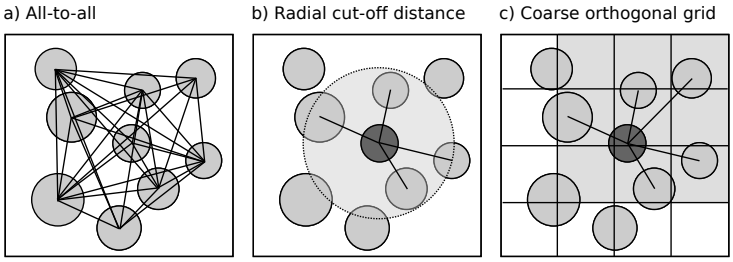

Figure 7.1. Commonly used neighbor search methods in particle-based methods. Lines denote contact checks between particles (circles) inside the model domain (box).

Classical DEM formulations only include repulsive interactions on physical contacts between grains. The simplest method for finding inter-grain contacts is to use an all-to-all algorithm (Fig. 7.1a) where all grains check all other grains for contact. This brute-force methodology is simple to implement, but causes large computational requirements as the number of grains increases ($\mathcal{O}(n^2)$). This implies that the simulation run time is proportional to the square of the number of grains. This contact search method is easily improved by considering the grain indexes and only checking for contacts from a grain i to grains with indexes $j < i$. The computational requirements still scale unfavorably as the grain numbers increase, however.

A more efficient approach is to perform spatial discretization, which allows grains to search for contacts only within their vicinity. This can be done by defining a radial cut-off distance from each grain center (Fig. 7.1b), where the search radius (r_s) is equal to the diameter of the largest grain ($\max(r)$) in addition to an extra length (s), i.e. $r_s = s + \max(r)$. Each grain initially saves a list of grains with center coordinates within this radius. This list can be reused in the following time step, until the fastest moving grain in the entire domain has traversed a spatial distance of s. Once this happens, the neighbor lists are rebuilt. This approach is unfavorable for implementation on GPUs, since determining the single largest value from many numbers is a slow reduction-type operation.

An alternative approach is to subdivide the simulation domain into a coarse grid of orthogonal cells (Fig. 7.1c). Each grain belongs to a single cell containing its center, and checks for contacts with grains in the adjacent cells. This methodology reduces the contact search complexity to the order of $\mathcal{O}(n \log n)$ and is used in my implementation.

7.4 Temporal integration

All soft-body DEMs require explicit temporal integration of the kinematic degrees of freedom. Applied integration schemes fall in three categories: One-step methods, multi-step methods, and predictor-corrector methods (Kruggel-Emden et al., 2008). The simplest integration scheme is the one-step Euler method, which is equivalent to the first-order Taylor expansion:

$$\dot{\boldsymbol{x}}_{t+\Delta t} = \dot{\boldsymbol{x}}_t + \ddot{\boldsymbol{x}}_t \Delta t \tag{7.14}$$

$$\boldsymbol{x}_{t+\Delta t} = \boldsymbol{x}_t + \dot{\boldsymbol{x}}_t \Delta t \tag{7.15}$$

where $\dot{\boldsymbol{x}}$ and $\boldsymbol{x}$ are the velocity and position of the grain, respectively. The solution precision is vastly improved by using the second-order Taylor expansion,

$$\dot{\boldsymbol{x}}_{t+\Delta t} = \dot{\boldsymbol{x}}_t + \ddot{\boldsymbol{x}}_t \Delta t \tag{7.16}$$

$$\boldsymbol{x}_{t+\Delta t} = \boldsymbol{x}_t + \dot{\boldsymbol{x}}_t \Delta t + \frac{1}{2}\ddot{\boldsymbol{x}}_t \Delta t^2 \tag{7.17}$$

or the three-term Taylor expansion:

$$\dot{\boldsymbol{x}}_{t+\Delta t} = \dot{\boldsymbol{x}}_t + \ddot{\boldsymbol{x}}_t \Delta t + \frac{1}{2}\dddot{\boldsymbol{x}}_t \Delta t^2 \tag{7.18}$$

$$\boldsymbol{x}_{t+\Delta t} = \boldsymbol{x}_t + \dot{\boldsymbol{x}}_t \Delta t + \frac{1}{2}\ddot{\boldsymbol{x}}_t \Delta t^2 + \frac{1}{6}\dddot{\boldsymbol{x}}_t \Delta t^3 \tag{7.19}$$

$\dddot{\boldsymbol{x}}$ is the temporal gradient of acceleration. The three-term Taylor expansion offers an optimal trade-off between solution precision and complexity, and is used in the experiments presented in this thesis. For a review of DEM temporal integration schemes the reader is referred to (Kruggel-Emden et al., 2008).

7.5 Practical example

The soft-body DEM is relatively straight forward to implement, due to it's explicit temporal integration scheme. The following code snippets demonstrate a simple program where round and non-rotating 3d grains are interacting and are pulled downwards due to gravity.

The grains are interacting with a simple contact law which doesn't depend on history of the contact. The normal force from grain contacts is linear elastic (Eq. 7.5), while the tangential force is viscous (Eq. 7.10).

The code examples are written resembling an object-oriented Python-style syntax. The kinematic and geometric properties of a single grain are saved in an class called `Grain` (lst. 7.1). Two objects of the `Grain` class interact in the class `Grain-GrainInteraction` (lst. 7.2), which resolves the forces the resulting forces on the `Grain` objects.

An example simulation is setup in code snippet lst. 7.3. First off the geometrical and physical simulation parameters are defined. Afterwards, `Grain` objects are created at various positions, and a suitable time step is chosen. Finally the script enters a time loop, where inter-grain contacts are found and resolved and temporal integration updates the position, velocity, and acceleration of all grains.

The example uses an all-to-all contact search algorithm with $\mathcal{O}(n^2)$ complexity, where all grains check for contacts with all other grains. This implies that the computational requirements (i.e. run time) scales with the square of the number of grains, making it rather unfavorable for many-body simulations.

```
class Grain:
    # A per-grain class containing individual parameters and
    # functions for each grain.

    def __init__(self,
                 pos=[0., 0., 0.,],
                 vel=[0., 0., 0.,],
                 acc=[0., 0., 0.,],
                 force=[0., 0., 0.,],
                 radius=1.,
                 density=2600.):
        # Initializing function with modifyable default values
        # :param pos: Grain linear position [m]
        # :param vel: Grain linear velocity [m/s]
        # :param acc: Grain linear acceleration [m/s^2]
        # :param force: Sum of forces [N]
        # :param radius: Grain radius [m]
        # :param density: Grain density [kg/m^3]
        self.pos = pos
        self.vel = vel
        self.acc = acc
        self.force = force
        self.radius = radius
        self.density = density

    def mass(self):
        # Returns the grain mass
        return self.density*4./3.*pi*self.radius**3

    def updateKinematics(self, dt):
        # Use temporal integration to project the grain
        # kinematics a length of time into the future.
        # Uses a two-term Taylor expansion.
        # :param dt: Time step length [s]
        self.acc = self.F/self.mass()
        vel_new = self.vel + self.acc*dt
        pos_new = self.pos + self.vel*dt + \
                  1./2.*self.acc*dt**2
        self.pos = pos_new
        self.vel = vel_new
```

Listing 7.1. `grain.py`: A simple example grain class for non-rotating grains.

```
class GrainGrainInteraction:
    # A class for resolving the interaction between two grains.
    # The contact is elastic in the normal direction and viscous
    # in the tangential direction of the contact.

    def __init__(self, p_i, p_j, k_n=1.e9, gamma_t=1.e6, mu=0.5):
        # Initialization function
        # :param p_i: First grain object
        # :param p_j: Second grain object
        # :param k_n: Contact stiffness [N/m]
        # :param gamma_t: Contact viscosity [N/(m/s)]
        # :param mu: Contact friction coefficient [-]
        self.p_i = p_i
        self.p_j = p_j
        self.k_n = k_n
        self.gamma_t = gamma_t
        self.mu = mu

    def interGrainVector(self):
        # Returns the inter-grain position vector
        # :returns: x_ij [m]
        return p_j.pos - p_i.pos

    def overlap(self):
        # Determine the grain overlap (overlap when negative)
        # :returns: delta_n [m]
        return abs(self.interGrainVector())\
            - (p_i.radius + p_j.radius)

    def contactParallelVelocity(self):
        # Determines the shear velocity on the contact surface due
        # to relative grain movement
        return p_i.vel - p_j.vel

    def normalVector(self):
        # Contact-normal vector
        # :returns: n [m]
        x_ij = self.interGrainVector()
        return x_ij/magn(x_ij)

    def normalForce(self):
        # Contact-normal force on grain i (opposite on grain j)
        return -self.k_n*self.overlap()*self.normalVector()

    def tangentialForce(self):
        # Contact-parallel force on grain i (opposite on grain j)
        return self.gamma_t*self.contactParallelVelocity()

    def interact(self):
        # Resolve contact interaction and forces on both grains
        f_n = self.normalForce()
        f_t = self.tangentialForce()

        # limit tangential force to Coulomb criterion
        if (magn(f_n)*mu < magn(f_t)):
            f_t = magn(f_n)*mu*f_t/magn(f_t)

        # Save resulting forces to the grains
        p_i.force += f_n + f_t
        p_j.force -= f_n + f_t
```

Listing 7.2. `interaction.py`: A grain interaction class with a simple contact model.

```
#!/usr/bin/env python
from grain import *         # grain.py
from interaction import *   # interaction.py

## Simulation parameters
t = 0.          # time at start
t_total = 5.    # simulation duration
grains = []     # Array of grains
g = 9.81        # Gravitational acceleration [m/s^2]

## Initialization
# Create and initialize grains (abbreviated)
for i in range(100):
    grains.append(Grain(pos, vel, acc, radius, density))

# Select suitable time step length
dt = 0.07/sqrt(1.e9/min(grains.m))

## Simulation main loop
while t < t_total:

    # Find grain-grain contacts
    contacts = []   # Empty array of grain contacts
    for i in range(len(grains)):
        for j in range(len(grains)):
            if i < j:
                contact = GrainGrainInteraction(i, j)
                if contact.overlap() < 0.:
                    contacts.append(contact)

    # Resolve forces from grain-grain contacts
    for contact in contacts:
        contact.interact()

    # Add gravitational acceleration
    for grain in grains:
        grain.acc += [0., 0., -g]

    # Update grain kinematic degrees of freedom
    for grain in grains:
        grain = updateKinematics()

    t += dt
```

Listing 7.3. `simulation.py`: An example simulation where grains in a box interact.

Chapter 8

Research note 2: *Porous flow modeling: Fluid description and solution methodology*

This chapter is intended to expand on the fundamental design choices and implementation details for the fluid phase numerical model used for this thesis.

The full source code used for the simulations in this thesis is available at `https://github.com/anders-dc/sphere`.

8.1 Introduction

The mathematical description of fluid flows relies on principal conservation laws like conservation of mass, momentum and energy, and is often summarized as the Navier-Stokes (NS) equations (e.g. Griebel et al., 1998). Analytical solutions to the NS equations have been used to solve fluid dynamics for simple problems, while various numerical approaches are more applicable for slightly more complex settings. Notable numerical methodologies range from the Lagrangian smoothed-particle hydrodynamics (SPH) method, where fluid behavior is considered the product of the collective behavior of water "particles". This method is particular popular for free-surface simulations such as dam breaches or wave action. The Lattice Boltzmann method (LBM) is a mixed Eulerian-Lagrangian approach where a finite number of fluid particles is transported between a static grid, especially powerful for resolving single or multiphase flow in complex geometries. Eulerian methods, such as the finite difference method (FDM), finite volume method (FVM), and the finite element method (FEM), are the most commonly used methods of CFD.

For the solution of pore-fluid flow in granular materials, a fast method for solving locally averaged fluid behavior is preferable over solutions of flow in the exact geometry of the pores. The reasoning is two-fold: (i) Adequately accurate geometries of three-dimensional pores require on the order of 100s to 1000s of fluid cells per particle, which far exceed the computational resources at hand, and (ii) the grain shapes used with the DEM are highly simplified where real materials are more angular. Perfectly resolving pore geometry is not yielding a more realistic behavior relative to deformation of real saturated granular media.

The following strategies rely on locally averaged material and flow properties, such as porosity and flow velocity (Anderson and Jackson, 1967). I describe the governing equations, the implementation, and applicability of two kinds of description of porous flow in granular media that have been developed and used for the studies in this PhD project.

8.2 Inertial pore-fluid flow

The following formulation treats the inter-particle fluid as an inertial fluid, involving both diffusion and advection. Mass is conserved in a control volume located inside the fluid if

$$\frac{\partial \rho_\mathrm{f}}{\partial t} + \nabla \cdot \boldsymbol{v}_\mathrm{f} = 0 \tag{8.1}$$

ρ_f is the fluid density and $\boldsymbol{v}_\mathrm{f}$ is the fluid velocity. Fluids like water are often considered incompressible in numerical implementations, which implies that the fluid density is constant. This assumption reduces the continuity equation to:

$$\nabla \cdot \boldsymbol{v}_\mathrm{f} = 0 \tag{8.2}$$

The momentum equation in the NS equations is derived from the Cauchy momentum equation:

$$\rho_\mathrm{f} \frac{\partial \boldsymbol{v}_\mathrm{f}}{\partial t} + \rho_\mathrm{f}(\boldsymbol{v}_\mathrm{f} \cdot \nabla \boldsymbol{v}_\mathrm{f}) = \nabla \cdot \boldsymbol{\sigma} + \rho_\mathrm{f} \boldsymbol{g} \tag{8.3}$$

Here, $\boldsymbol{\sigma}$ is the Cauchy stress tensor and $\boldsymbol{g}$ is the gravitational acceleration. For incompressible Newtonian fluids the Cauchy stress tensor is given by:

$$\boldsymbol{\sigma} = -p_\mathrm{f}\boldsymbol{I} + \boldsymbol{\tau} \tag{8.4}$$

p_f is the fluid pressure, $\boldsymbol{I}$ is the identity tensor, and $\boldsymbol{\tau}$ is the deviatoric stress tensor, for Newtonian fluids given by:

$$\boldsymbol{\tau} = \mu_\mathrm{f}\nabla\boldsymbol{v}_\mathrm{f} + \mu_\mathrm{f}(\nabla\boldsymbol{v}_\mathrm{f})^T \tag{8.5}$$

By using the following vector identities for a vector ($\boldsymbol{v}_\mathrm{f}$) and a scalar field ($p_\mathrm{f}$) (Spiegel et al., 1968):

$$\nabla\cdot(p\boldsymbol{I}) = \nabla p_\mathrm{f} \tag{8.6}$$

$$\nabla\cdot(\nabla\boldsymbol{v}_\mathrm{f}) = \nabla^2\boldsymbol{v}_\mathrm{f} \tag{8.7}$$

$$\nabla\cdot(\nabla\boldsymbol{v}_\mathrm{f})^T = \nabla(\nabla\cdot\boldsymbol{v}_\mathrm{f}) = \nabla(0) = 0 \tag{8.8}$$

the Cauchy stress tensor simplifies the following, assuming that spatial variations in viscosity can be neglected:

$$\nabla\cdot\boldsymbol{\sigma} = -\nabla p_\mathrm{f} + \mu_\mathrm{f}\nabla^2\boldsymbol{v}_\mathrm{f} \tag{8.9}$$

The transpose term in Eq. 8.8 equals zero due to the incompressible continuity equation (Eq. 8.2).

For the coupled particle-fluid simulations in this thesis, the fluid behavior is spatially averaged over two-phase volumes that can contain both the solid and fluid phase (Zhou et al., 2010). The incompressible mass conservation equation is modified to contain porosity ϕ:

$$\frac{\partial\phi}{\partial t} + \nabla\cdot(\phi\boldsymbol{v}_\mathrm{f}) = 0 \tag{8.10}$$

There are different ways of including porosity and grain-fluid interaction forces ($\boldsymbol{F}_\mathrm{i}$) in the momentum equation. The most favorable form (set 2 in Zhou et al. (2010), model A in Zhu et al. (2007)) is:

$$\frac{\partial(\phi\boldsymbol{v}_\mathrm{f})}{\partial t} + \nabla\cdot(\phi\boldsymbol{v}_\mathrm{f}\otimes\boldsymbol{v}_\mathrm{f}) = -\frac{\phi}{\rho_\mathrm{f}}\nabla p_\mathrm{f} - \frac{1}{\rho_\mathrm{f}}\boldsymbol{F}_\mathrm{i} + \frac{\phi}{\rho_\mathrm{f}}\nabla\cdot\boldsymbol{\tau} + \phi\boldsymbol{g} \tag{8.11}$$

where $\boldsymbol{\tau}$ is the deviatoric part of the fluid stress tensor from before. The $\otimes$ operator denotes dyadic multiplication of vectors yielding a tensor product.

Numerical solution procedure

The solution procedure uses the operator splitting methodology presented in Langtangen et al. (2002), which is modified for the two-phase NS formulation. First, velocities at $t+\Delta t$ are predicted ($\boldsymbol{v}_\mathrm{f}^*$) by explicit temporal integration of the momentum equation (Eq. 8.11), based on the fluid state at time t:

$$\boldsymbol{v}_\mathrm{f}^* = \boldsymbol{v}_\mathrm{f}{}^t - \frac{\beta\phi^t\Delta t}{\rho_\mathrm{f}}\nabla p_\mathrm{f}{}^t - \frac{\Delta t}{\rho_\mathrm{f}\phi^t}\boldsymbol{F}_\mathrm{i}{}^t + \frac{\Delta t}{\rho_\mathrm{f}}\nabla\cdot\boldsymbol{\tau}^t + \Delta t\boldsymbol{g} - \frac{\Delta\phi^t\boldsymbol{v}_\mathrm{f}{}^t}{\phi^t} - \frac{\Delta t}{\phi^t}\nabla\cdot(\phi^t\boldsymbol{v}_\mathrm{f}{}^t\otimes\boldsymbol{v}_\mathrm{f}{}^t) \tag{8.12}$$

$\beta \in [0;1]$ is a dimensionless fluid solver parameter. The true velocity at time $t+\Delta t$ is dependent on the unknown fluid pressure at $t+\Delta t$. The predicted velocity is not guaranteed to satisfy the continuity equation (Eq. 8.10). The true fluid velocity can be found by adding an unknown correction term $\boldsymbol{v}_{\mathrm{f}}{}^{c}$ to the predicted value:

$$\boldsymbol{v}_{\mathrm{f}}{}^{t+\Delta t} = \boldsymbol{v}_{\mathrm{f}}{}^{*} + \boldsymbol{v}_{\mathrm{f}}{}^{c} \quad \Rightarrow \quad \boldsymbol{v}_{\mathrm{f}}{}^{c} = \boldsymbol{v}_{\mathrm{f}}{}^{t+\Delta t} - \boldsymbol{v}_{\mathrm{f}}{}^{*} \tag{8.13}$$

$$\boldsymbol{v}_{\mathrm{f}}{}^{c} = -\frac{\Delta t}{\rho_{\mathrm{f}}} \nabla p_{\mathrm{f}}{}^{t+\Delta t} + \frac{\beta \Delta t}{\rho_{\mathrm{f}}} \nabla p_{\mathrm{f}}{}^{t} = -\frac{\Delta t}{\rho_{\mathrm{f}}} \nabla (p_{\mathrm{f}}{}^{t+\Delta t} - \beta p_{\mathrm{f}}{}^{t+\Delta t}) \tag{8.14}$$

By defining a corrective term ($\epsilon \equiv p_{\mathrm{f}}{}^{t+\Delta t} - \beta p_{\mathrm{f}}{}^{t+\Delta t}$) a simpler expression of the velocity prediction correction emerges:

$$\boldsymbol{v}_{\mathrm{f}}{}^{t+\Delta t} = \boldsymbol{v}_{\mathrm{f}}{}^{*} - \frac{\Delta t}{\rho_{\mathrm{f}}} \nabla \epsilon \tag{8.15}$$

The above expression for the fluid velocity at $t+\Delta t$ is inserted in the continuity equation (Eq. 8.10):

$$\frac{\partial \phi}{\partial t} + \nabla \cdot (\phi \boldsymbol{v}_{\mathrm{f}}{}^{t+\Delta t}) = \frac{\partial \phi}{\partial t} + \nabla \phi \cdot \boldsymbol{v}_{\mathrm{f}}{}^{t+\Delta t} + \phi \nabla \cdot \boldsymbol{v}_{\mathrm{f}}{}^{t+\Delta t} = 0 \tag{8.16}$$

Afterwards, Eq. 8.15 is inserted as the velocity at $t+\Delta t$:

$$\frac{\Delta \phi}{\Delta t} + \nabla \phi \cdot \left(\boldsymbol{v}_{\mathrm{f}}{}^{*} - \frac{\Delta t}{\rho_{\mathrm{f}}} \nabla \epsilon \right) + \phi \nabla \cdot \left(\boldsymbol{v}_{\mathrm{f}}{}^{*} - \frac{\Delta t}{\rho_{\mathrm{f}}} \nabla \epsilon \right) = 0 \tag{8.17}$$

$$\frac{\Delta \phi}{\Delta t} + \nabla \phi \cdot \boldsymbol{v}_{\mathrm{f}}{}^{*} - \frac{\Delta t}{\rho_{\mathrm{f}}} \nabla \phi \cdot \nabla \epsilon + \phi \nabla \cdot \boldsymbol{v}_{\mathrm{f}}{}^{*} - \frac{\Delta t}{\rho_{\mathrm{f}}} \phi \nabla^2 \epsilon = 0 \tag{8.18}$$

The above equation is rearranged into the form of a Poisson equation ($\nabla^2 \Phi = f$), with a composite forcing function f (right-hand side):

$$\nabla^2 \epsilon = \frac{\Delta \phi \rho_{\mathrm{f}}}{\Delta t^2 \phi} + \frac{\rho_{\mathrm{f}} \nabla \phi \cdot \boldsymbol{v}_{\mathrm{f}}{}^{*}}{\Delta t \phi} - \frac{\nabla \phi \cdot \nabla \epsilon}{\phi} + \frac{\rho_{\mathrm{f}} \nabla \cdot \boldsymbol{v}_{\mathrm{f}}{}^{*}}{\Delta t} \tag{8.19}$$

Using second-order FDM approximations of the second-order partial derivatives in the Laplace operator (∇^2), the solution to the Poisson equation can be solved iteratively using Jacobi updates. The total number of unknowns is $(n_x - 1)(n_y - 1)(n_z - 1)$, where n_d denotes the number of grid cells along dimension d.

The discrete Laplacian[1] can be obtained by a finite-difference seven-point stencil in a three-dimensional cubic grid with cell spacing Δx, Δy, Δz by considering the six neighboring cells adjacent to the cell faces. i_d denotes the cell index along dimension d:

$$\begin{aligned} \nabla^2 \epsilon_{i_x,i_y,i_z} \approx & \frac{\epsilon_{i_x-1,i_y,i_z} - 2\epsilon_{i_x,i_y,i_z} + \epsilon_{i_x+1,i_y,i_z}}{\Delta x^2} \\ & + \frac{\epsilon_{i_x,i_y-1,i_z} - 2\epsilon_{i_x,i_y,i_z} + \epsilon_{i_x,i_y+1,i_z}}{\Delta y^2} \\ & + \frac{\epsilon_{i_x,i_y,i_z-1} - 2\epsilon_{i_x,i_y,i_z} + \epsilon_{i_x,i_y,i_z+1}}{\Delta z^2} \approx f_{i_x,i_y,i_z} \end{aligned} \tag{8.20}$$

[1] Approximation of the Laplace operator

Within a Jacobi iteration, the value of the unknowns (ϵ^n) is used to find an updated solution estimate (ϵ^{n+1}). The solution for the updated value takes the form:

$$\begin{aligned}\epsilon^{n+1}_{i_x,i_y,i_z} =& \frac{-\Delta x^2\Delta y^2\Delta z^2 f_{i_x,i_y,i_z}}{2(\Delta x^2\Delta y^2+\Delta x^2\Delta z^2+\Delta y^2\Delta z^2)} \\ &+\frac{\Delta y^2\Delta z^2(\epsilon^n_{i_x-1,i_y,i_z}+\epsilon^n_{i_x+1,i_y,i_z})}{2(\Delta x^2\Delta y^2+\Delta x^2\Delta z^2+\Delta y^2\Delta z^2)} \\ &+\frac{\Delta x^2\Delta z^2(\epsilon^n_{i_x,i_y-1,i_z}+\epsilon^n_{i_x,i_y+1,i_z})}{2(\Delta x^2\Delta y^2+\Delta x^2\Delta z^2+\Delta y^2\Delta z^2)} \\ &+\frac{\Delta x^2\Delta y^2(\epsilon^n_{i_x,i_y,i_z-1}+\epsilon^n_{i_x,i_y,i_z+1})}{2(\Delta x^2\Delta y^2+\Delta x^2\Delta z^2+\Delta y^2\Delta z^2)}\end{aligned} \tag{8.21}$$

The difference between the current and updated value is termed the *normalized residual*:

$$r_{i_x,i_y,i_z} = \frac{(\epsilon^{n+1}_{i_x,i_y,i_z}-\epsilon^n_{i_x,i_y,i_z})^2}{(\epsilon^{n+1}_{i_x,i_y,i_z})^2} \tag{8.22}$$

The updated values are at the end of the iteration stored as the current values, and the maximal value of the normalized residual is found. If this value is larger than a specified tolerance criteria, the update procedure is repeated. The iterative procedure is ended if the number of iterations exceeds a defined limit, should the solution not converge. After the values of ϵ are found, they are used to find the new velocities (Eq. 8.15) and pressures:

$${p_\mathrm{f}}^{t+\Delta t} = \beta {p_\mathrm{f}}^t + \epsilon \tag{8.23}$$

Solid-fluid interaction

The particle-fluid momentum exchange follows the procedure outlined by Xu and Yu (1997), Feng and Yu (2004) and Zhou et al. (2010) (scheme 3). At each time step, the particle–fluid interaction forces on individual particles in each fluid cell are determined ($\boldsymbol{f}_\mathrm{i}$)), and the values are summed to produce the particle–fluid interaction force per fluid volume on the fluid ($\boldsymbol{F}_\mathrm{i}$).

The interaction force imposed onto the particles is composed of the drag force ($\boldsymbol{f}_\mathrm{d}$), the pressure gradient force ($\boldsymbol{f}_{\nabla p}$) and the viscous force ($\boldsymbol{f}_{\nabla\cdot\boldsymbol{\tau}}$). For a particle with index i, the interaction force is:

$$\boldsymbol{f}_\mathrm{i} = \boldsymbol{f}_{\mathrm{d},i} + \boldsymbol{f}_{\nabla p_\mathrm{f},i} + \boldsymbol{f}_{\nabla\cdot\boldsymbol{\tau},i} \tag{8.24}$$

The particle-fluid interaction force $\boldsymbol{f}_\mathrm{i}$ is added to the sum of linear forces per particle (Eq. 3 in Damsgaard et al. (2013)). The drag force acts with opposite signs on the fluid. The interaction force for a fluid cell with volume ΔV containing n particles is found as:

$$\boldsymbol{F}_\mathrm{i} = \frac{1}{\Delta V}\sum_{i=1}^{n}\boldsymbol{f}_{\mathrm{d},i} \tag{8.25}$$

The pressure gradient force and viscous force is applied to the fluid through the other terms in the momentum equation (Eq. 8.11) (Zhou et al., 2010).

The drag force is determined by semi-empirical relationships (Ergun, 1952; Wen and Yu, 1966; Gidaspow et al., 1992; Di Felice, 1994). The force magnitude scales linearly with the relative velocity difference between particle and fluid:

$$\boldsymbol{f}_{\mathrm{d}} = 0.125 C_{\mathrm{d0},i} \rho_f \pi 2 r_i^2 \phi^2 ||\boldsymbol{v}_{\mathrm{f}} - \boldsymbol{v}_{\mathrm{p}}|| (\boldsymbol{v}_{\mathrm{f}} - \boldsymbol{v}_{\mathrm{p}}) \phi^{-\chi} \tag{8.26}$$

where r_i is the radius and $\boldsymbol{v}_{\mathrm{p}}$ is the linear velocity of particle i. The drag coefficient for a spherical particle is:

$$C_{\mathrm{d0},i} = \left(0.63 + \frac{4.8}{Re_i^{0.5}}\right)^2 \tag{8.27}$$

The empirical coefficient χ is found as:

$$\chi = 3.7 - 0.65 \exp\left(-\frac{1.5 - (\log_{10} Re_i)^2}{2}\right) \tag{8.28}$$

The particle Reynolds number is defined by:

$$Re_i = \rho_{\mathrm{f}} 2 r_i \phi ||\boldsymbol{v}_{\mathrm{f}} - \boldsymbol{v}_{\mathrm{p}}|| / \mu_{\mathrm{f}} \tag{8.29}$$

The pressure gradient force is calculated as:

$$\boldsymbol{f}_{\nabla p_{\mathrm{f}}} = -\nabla p_{\mathrm{f}} V_{\mathrm{p}} \tag{8.30}$$

where V_p is the volume of the particle. Note that the pressure force includes buoyancy. The viscous force is defined as:

$$\boldsymbol{f}_{\nabla \cdot \boldsymbol{\tau}} = -(\nabla \cdot \boldsymbol{\tau}) V_{\mathrm{p}} \tag{8.31}$$

Implementation and applicability

The soft-body DEM interactions require very short time steps in order to ensure numerical stability. It is common to use CFD time steps which are between one and three magnitudes longer than the DEM time step, which still produces identical results and increases computational performance (Shamy and Zeghal, 2005; Kloss et al., 2012; Zhao and Shan, 2013). I found the optimal ratio between $\Delta t_{\mathrm{CFD}} / \Delta t_{\mathrm{DEM}}$ to be around 10.

The simulation domain is discretized in a regular rectiliniear orthogonal staggered grid (C-type in (Arakawa and Lamb, 1977). The numerical solution is continuously checked for stability by von Neumann analysis and the CFL condition. The Navier-Stokes based CFD algorithm is implemented in CUDA C (NVIDIA, 2013b), which allows direct memory access to the DEM information. I found that the fluid solution procedure works most efficiently when the solver parameter β is 0, which corresponds to the Chorin projection method (Chorin, 1968; Temam, 1969; Griebel et al., 1998; Langtangen et al., 2002).

When I started using the above coupled algorithm between grains and a full Navier-Stokes fluid solution, it became apparent that the formulation was very applicable for relatively fast fluid flows, owing to its completeness and precise solution on the staggered grid, and due to its inclusion of several types of grain-fluid interaction forces. The method proved not optimal, however, for simulating granular materials with lower permeabilities and consequential slow fluid velocities.

The governing equations (Eq. 8.10 and 8.11) provide no simple method of adjusting hydraulic properties such as permeability, and ad-hoc tuning of permeability by scaling fluid velocities proved to decrease solver performance drastically.

I decided to try a different fluid formulation based on Darcian flow, which assumes fluid flow is taking place at negligible velocities (*Stokes flow*), and allows for explicit definition of the magnitude of permeability.

8.3 Inertialess pore-fluid flow

In this formulation the inertial forces in the fluid are assumed to be negligible with respect to viscous resistance (Gerya, 2010), which is true for slowly flowing water in aquifers. Advection is negligible, and diffusion is the sole mechanism for transport. The governing pore-fluid equation is derived from the equations of conservation of mass for a two-phase mixture of compressible solid and fluid phases (McNamara et al., 2000; Goren et al., 2010; Goren et al., 2011):

$$\text{Solid:} \qquad \frac{\partial(1-\phi)\rho}{\Delta t} + \nabla \cdot \left[(1-\phi)\rho\bar{\dot{\boldsymbol{x}}}\right] = 0 \tag{8.32}$$

$$\text{Fluid:} \qquad \frac{\partial \phi \rho_\mathrm{f}}{\Delta t} + \nabla \cdot [\phi \rho_\mathrm{f} \boldsymbol{v}_\mathrm{f}] = 0 \tag{8.33}$$

where $\bar{\dot{\boldsymbol{x}}}$ is the locally averaged solid phase (grain) velocity and ρ is the solid phase density. For conservation of momentum, Darcy's law is derived from Stokes law of slow flow:

$$\phi(\boldsymbol{v}_\mathrm{f} - \dot{\boldsymbol{x}}) = -\frac{k}{\mu_\mathrm{f}} \nabla p_\mathrm{f} \tag{8.34}$$

k is the intrinsic permeability and μ_f is the fluid density. p_f is the fluid pressure. The above relation states that velocity differences between the solid and fluid phase take place proportionally to the negative value of the fluid-pressure gradient, scaled by permeability and fluid viscosity.

The fluid density can be modified by elastic deformation due to pressure, scaled by the fluid adiabatic compressibility β_f:

$$\rho_\mathrm{f} = \rho_0(1 + \beta_\mathrm{f} p_\mathrm{f}) \tag{8.35}$$

Goren et al. (2010) assumes that the solid phase is relatively incompressible relative to the otherwise stiff fluid fluid, which, which is reasonable in the case of e.g. quartz grains submerged in water. Goren et al. (2011) also assumes that the length scale of pore pressure diffusion exceeds the diameter of a single grain. Together with these assumptions, equations 8.32 to 8.35 can be combined to a single equation of pore-pressure diffusion of a compressible fluid, flowing according to Darcy's law:

$$\frac{\partial p_\mathrm{f}}{\partial t} = \frac{1}{\beta_\mathrm{f}\phi\mu_\mathrm{f}} \nabla \cdot (k \nabla p_\mathrm{f}) + \frac{1}{\beta_\mathrm{f}\phi} \nabla \cdot \bar{\dot{\boldsymbol{x}}} \tag{8.36}$$

The above equation describes transient evolution $\partial/(\partial t)$ of pore-water pressure p_f as the sum of spatial diffusion (first term on the right-hand side) and forcing from the solid phase (second term on the right hand side). The divergence of average solid velocity ($\nabla \cdot \bar{\dot{\boldsymbol{x}}}$) is negative when grains move away from each other, while a confluence of solids makes the term positive.

During implementation of the above equation, I found that stability was improved by using a forcing term from the solid phase with information from several time steps. This was achieved by forcing the fluid with porosity change (Goren et al., 2011) instead of the divergence of fluids which only considers current grain velocities. The forcing term is corrected for advection of porosities:

$$\frac{\partial p_\mathrm{f}}{\partial t} = \frac{1}{\beta_\mathrm{f}\phi\mu_\mathrm{f}}\nabla\cdot(k\nabla p_\mathrm{f}) + \frac{1}{\beta_\mathrm{f}(1-\phi)}\left(\frac{\partial\phi}{\partial t} + \bar{\boldsymbol{x}}\cdot\nabla\phi\right) \tag{8.37}$$

The solid-fluid interaction for this fluid formulation is based on pore-pressure gradient forces, and presented in chapter 5.

Numerical solution procedure

The fluid pressure (p_f) are the only unknowns in the system of equations. The spatial discretization is a rectilinear orthogonal non-staggered grid with fluid pressure, the gradient of fluid pressure (∇p_f), porosity (ϕ), permeability (k) and mean particle velocity ($\bar{\boldsymbol{x}}$) located at the cell center.

At the beginning of each time step, a pore-pressure change is found using an explicit solution to the pore-pressure equation (Eq. 8.37):

$$\Delta {p_\mathrm{f}}^{\mathrm{expl}} = \frac{\Delta t}{\beta_\mathrm{f}\phi\mu_\mathrm{f}}\left(k\nabla^2 p_\mathrm{f} + \nabla k\cdot\nabla p_\mathrm{f}\right) - \frac{\Delta t}{\beta_\mathrm{f}\phi(1-\phi)}\left(\frac{\Delta\phi}{\Delta t} + \bar{\boldsymbol{x}}\cdot\nabla\phi\right) \tag{8.38}$$

The fluid pressure gradient is for the cell (i,j,k) approximated by first-order central differences using the adjacent cell fluid pressures:

$$\nabla {p_\mathrm{f}}^{i,j,k} \approx \left(\frac{{p_\mathrm{f}}^{i+1,j,k} - {p_\mathrm{f}}^{i-1,j,k}}{2\Delta x}, \frac{{p_\mathrm{f}}^{i,j+1,k} - {p_\mathrm{f}}^{i,j-1,k}}{2\Delta y}, \frac{{p_\mathrm{f}}^{i,j,k+1} - {p_\mathrm{f}}^{i,j,k-1}}{2\Delta z}\right) \tag{8.39}$$

The porosity and permeability gradients (∇k and $\nabla\phi$) are found in the same manner. The Laplacian of fluid pressure ($\nabla^2 p_\mathrm{f}$) is approximated by second-order central differences:

$$\begin{aligned}\nabla^2 {p_\mathrm{f}}^{i,j,k} \approx & \frac{{p_\mathrm{f}}^{i+1,j,k} - 2{p_\mathrm{f}}^{i,j,k} + {p_\mathrm{f}}^{i-1,j,k}}{\Delta x^2} + \\ & \frac{{p_\mathrm{f}}^{i,j+1,k} - 2{p_\mathrm{f}}^{i,j,k} + {p_\mathrm{f}}^{i,j-1,k}}{\Delta y^2} + \\ & \frac{{p_\mathrm{f}}^{i,j,k+1} - 2{p_\mathrm{f}}^{i,j,k} + {p_\mathrm{f}}^{i,j,k-1}}{\Delta z^2}\end{aligned} \tag{8.40}$$

At Dirchlet (fixed pressure) boundaries, the change in fluid pressure is defined to be 0. At Neumann (fixed pressure gradient) boundaries, the grid is padded with cells with fluid pressures adjusting to satisfying the gradient value. Periodic boundaries are padded with cells that duplicate the field values at the cells at the opposite boundaries.

Once the explicit-solution change in fluid pressure has been determined, the algorithm enters an iterative loop, where the implicit solution to the fluid-pressure equation change ($\Delta {p_\mathrm{f}}^{\mathrm{impl}}$) is found by repeatedly computing the solution to equation 8.38 until the solution converges. The new fluid pressure is found from the explicit and implicit solutions:

$${p_\mathrm{f}}^{t+\Delta t} = {p_\mathrm{f}}^{t} + (1-\epsilon)\Delta {p_\mathrm{f}}^{\mathrm{expl}} + \epsilon\Delta {p_\mathrm{f}}^{\mathrm{impl}} \tag{8.41}$$

where $\epsilon \in [0;1]$ is used to select the integration method. A value of 0 denotes a fully explicit solution, and 1 yields an implicit solution. I used a value of $\frac{1}{2}$ which gives the Crank-Nicolson method, which is unconditionally stable and second-order precise.

The GPU implementation of the solution procedure turned out to be highly efficient, which allowed the simulations to be performed with fluid-pressure updates for each DEM time step, effectively avoiding potential temporal resolution issues.

Bibliography

Aharonov, E. and D. Sparks (1999). “Rigidity phase transition in granular packings”. In: *Physical Review E* 60.6, pp. 6890–6896.

— (2002). “Shear profiles and localization in simulations of granular shear”. In: *Phys. Rev., E* 65, p. 051302.

Alley, R. B. (1989a). “Water-pressure coupling of sliding and bed deformation: I. Water system”. In: *Journal of Glaciology* 35.119, pp. 108–118.

— (1989b). “Water-pressure coupling of sliding and bed deformation: II. Velocity-depth profiles”. In: *Journal of Glaciology* 35.119, pp. 108–118.

— (1990). “Multiple steady states in ice-water-till systems”. In: *Annals of Glaciology* 14, pp. 1–5.

— (1991). “Deforming-bed origin for southern Laurentide till sheets?” In: *Journal of Glaciology* 37.125, pp. 67–76.

— (1993). “In search of ice-stream sticky spots”. In: *Journal of Glaciology* 39.133, pp. 447–454.

— (2000). “Continuity comes first: recent progress in understanding subglacial deformation”. In: *Geological Society, London, Special Publications* 176.1, pp. 171–179.

Alley, R. B. and I. M. Whillans (1991). “Changes in the West Antarctic ice sheet”. In: *Science* 254.5034, pp. 959–963.

Alley, R. B., D. D. Blankenship, C. R. Bentley, and S. T. Rooney (1986). “Deformation of till beneath ice stream B, West Antarctica”. In: *Nature* 322, pp. 57–59.

Alley, R. B., D. D. Blankenship, C. R. Bentley, and S.T. R. (1987a). “Till beneath ice stream B: 3. Till deformation: evidence and implications”. In: *Journal of Geophysical Research: Solid Earth* 92.B9, pp. 8921–8929.

Alley, R. B., D. D. Blankenship, S. T. Rooney, and C. R. Bentley (1987b). “Till beneath ice stream B 4. A coupled ice-till flow model”. In: *Journal of Geophysical Research* 92.B9, pp. 8931–8940.

— (1989a). “Sedimentation beneath ice shelves—the view from ice stream B”. In: *Marine Geology* 85.2, pp. 101–120.

— (1989b). “Water-pressure coupling of sliding and bed deformation: III. Application to ice stream B, Antarctica”. In: *Journal of Glaciology* 35.119, pp. 130–139.

Alley, R. B., K. M. Cuffey, E. B. Evenson, J. C. Strasser, D. E. Lawson, and G. J. Larson (1997). “How glaciers entrain and transport basal sediment: physical constraints”. In: *Quaternary Science Reviews* 16.9, pp. 1017–1038.

Alley, R. B., D. E. Lawson, E. B. Evenson, J. C. Strasser, and G. J. Larson (1998). "Glaciohydraulic supercooling: a freeze-on mechanism to create stratified, debris-rich basal ice: II. Theory". In: *Journal of Glaciology* 44.148, pp. 563–569.

Alley, R. B., D. E. Lawson, G. J. Larson, E. B. Evenson, and G. S. Baker (2003). "Stabilizing feedbacks in glacier-bed erosion". In: *Nature* 424.6950, pp. 758–760.

Alley, R. B., P. U. Clark, P. Huybrechts, and I. Joughin (2005). "Ice-sheet and sea-level changes". In: *Science* 310.5747, pp. 456–460.

Anandakrishnan, S. (2003). "Dilatant till layer near the onset of streaming flow of Ice Stream C, West Antarctica, determined by AVO (amplitude vs offset) analysis". In: *Annals of Glaciology* 36.1, pp. 283–286.

Anandakrishnan, S., D. D. Blankenship, R. B. Alley, and P. L. Stoffa (1998). "Influence of subglacial geology on the position of a West Antarctic ice stream from seismic observations". In: *Nature* 394.6688, pp. 62–65.

Anandakrishnan, S., D. E. Voigt, R. B. Alley, and M. A. King (2003). "Ice stream D flow speed is strongly modulated by the tide beneath the Ross Ice Shelf". In: *Geophysical Research Letters* 30.7.

Anderson, T. B. and R. Jackson (1967). "A fluid mechanical description of fluidized beds". In: *Industrial & Engineering Chemistry Fundamentals* 6.4, pp. 527–539.

Anthony, J. L. and C. Marone (2005). "Influence of particle characteristics on granular friction". In: *Journal of Geophysical Research: Solid Earth* 110.B8.

Arakawa, A. and V. R. Lamb (1977). "Computational design of the basic dynamical processes of the UCLA general circulation model". In: *Methods in computational physics* 17, pp. 173–265.

Azéma, E. and F. Radjaï (2010). "Stress-strain behavior and geometrical properties of packings of elongated particles". In: *Physical Review E* 81.5, p. 051304.

Azéma, E., N. Estrada, and F. Radjaï (2012). "Nonlinear effects of particle shape angularity in sheared granular media". In: *Physical Review E* 86.4, p. 041301.

Bartholomaus, T. C., R. S. Anderson, and S. P. Anderson (2008). "Response of glacier basal motion to transient water storage". In: *Nature Geoscience* 1.1, pp. 33–37.

— (2011). "Growth and collapse of the distributed subglacial hydrologic system of Kennicott Glacier, Alaska, USA, and its effects on basal motion". In: *Journal of Glaciology* 57.206, p. 985.

Bartholomew, I., P. Nienow, D. Mair, A. Hubbard, M. A King, and A. Sole (2010). "Seasonal evolution of subglacial drainage and acceleration in a Greenland outlet glacier". In: *Nature Geoscience* 3.6, pp. 408–411.

Bateman, M. D., D. A. Swift, J. A. Piotrowski, and D. C. W. Sanderson (2012). "Investigating the effects of glacial shearing of sediment on luminescence". In: *Quaternary Geochronology* 10, pp. 230–236.

Beem, L. H., S. M. Tulaczyk, M. A. King, M. Bougamont, H. A. Fricker, and P. Christoffersen (2014). "Variable deceleration of Whillans Ice Stream, West Antarctica". In: *Journal of Geophysical Research: Earth Surface* 119.2, pp. 212–224.

Beget, J. E. (1986). "Modeling the influence of till rheology on the flow and profile of the Lake Michigan lobe, southern Laurentide ice sheet, USA". In: *Journal of Glaciology* 32, pp. 235–241.

— (1987). "Low profile of the Northwest Laurentide Ice Sheet". In: *Journal of Glaciology* 32, pp. 235–241.

Belheine, N., J. P. Plassiard, F. V. Donzé, F. Darve, and A. Seridi (2009). "Numerical simulation of drained triaxial test using 3D discrete element modeling". In: *Computers and Geotechnics* 36.1, pp. 320–331.

Benn, D. and D. J. A. Evans (2014). *Glaciers and Glaciation*. Routledge.

Bennett, M. R. (2003). "Ice streams as the arteries of an ice sheet: their mechanics, stability and significance". In: *Earth-Science Reviews* 61.3-4, pp. 309–339.

Bentley, C. R. (1997). "Rapid sea-level rise soon from West Antarctic ice sheet collapse?" In: *Science* 275.5303, p. 1077.

Bindschadler, R. A., M. A. King, R. B. Alley, S. Anandakrishnan, and L. Padman (2003). "Tidally controlled stick-slip discharge of a West Antarctic ice". In: *Science* 301.5636, pp. 1087–1089.

Bindschadler, R., J. Bamber, and S. Anandakrishnan (2001). "The West Antarctic ice sheet: behavior and environment". In: *The West Antarctic Ice Sheet: Behavior and Environment*. American Geophysical Union. Chap. Onset of Streaming Flow in the Siple Coast Region, West Antarctica, pp. 123–136.

Blake, E. W., U. H. Fischer, and G. K. C. CLarke (1994). "Instruments and methods: direct measurement of sliding at the glacier bed". In: *Journal of Glaciology* 40.136.

Blake, E., G. K. C. Clarke, and M. C. Gérin (1992). "Tools for examining subglacial bed deformation". In: *Journal of Glaciology* 38, pp. 388–396.

Blankenship, D. D., C. R. Bentley, S. T. Rooney, and R. B. Alley (1986). "Seismic measurements reveal a saturated porous layer beneath an active Antarctic ice stream". In: *Nature*.

Borst, R. de (1991). "Numerical modelling of bifurcation and localisation in cohesive-frictional materials". In: *Pure and Applied Geophysics* 137.4, pp. 367–390.

Bougamont, M. and P. Christoffersen (2012). "Hydrologic forcing of ice stream flow promotes rapid transport of sediment in basal ice". In: *Geology* 40.8, pp. 735–738.

Bougamont, M., S. Price, P. Christoffersen, and A. J. Payne (2011). "Dynamic patterns of ice stream flow in a 3-D higher-order ice sheet model with plastic bed and simplified hydrology". In: *Journal of Geophysical Research: Earth Surface* 116, F04018.

Boulton, G. S. (1978). "Boulder shapes and grain-size distributions of debris as indicators of transport paths through a glacier and till genesis". In: *Sedimentology* 25, pp. 773–799.

— (1986). "A paradigm shift in glaciology?" In: *Nature* 322, p. 18.

— (1996). "Theory of glacial erosion, transport and deposition as a consequence of subglacial sediment deformation". In: *Journal of Glaciology* 42.140, pp. 43–62.

Boulton, G. S. and R. C. A. Hindmarsh (1987). "Sediment deformation beneath glaciers: rheology and geological consequences". In: *Journal of Geophysical Research* 92.B9, pp. 9059–9082.

Boulton, G. S. and A. S. Jones (1979). "Stability of temperate ice caps and ice sheets resting on beds of deformable sediment". In: *Journal of Glaciology* 24.90.

Boulton, G. S., D. L. Dent, and E. M. Morris (1974). "Subglacial shearing and crushing, and the role of water pressures in tills from south-east Iceland". In: *Geografiska Annaler. Series A. Physical Geography*, pp. 135–145.

Boulton, G. S., K. E. Dobbie, and S. Zatsepin (2001). "Sediment deformation beneath glaciers and its coupling to the subglacial hydraulic system". In: *Quaternary International* 86.1, pp. 3–28.

Bowles, J. E. (1992). *Engineering properties of soils and their measurement*. Irwin/McGraw-Hill, p. 241.
Boyce, J. I. and N. Eyles (1991). "Drumlins carved by deforming till streams below the Laurentide ice sheet". In: *Geology* 19.8, pp. 787–790.
— (2000). "Architectural element analysis applied to glacial deposits: Internal geometry of a late Pleistocene till sheet, Ontario, Canada". In: *Geological Society of America Bulletin* 112.1, pp. 98–118.
Brown, N. E., B. Hallet, and D. B. Booth (1987). "Rapid soft bed sliding of the Puget glacial lobe". In: *Journal of Geophysical Research: Solid Earth* 92.B9, pp. 8985–8997.
Budd, W. F., P. L. Keage, and N. A. Blundy (1979). "Empirical studies of ice sliding". In: *Journal of Glaciology* 23, pp. 157–170.
Bueler, E. and J. Brown (2009). "Shallow shelf approximation as a "sliding law" in a thermomechanically coupled ice sheet model". In: *Journal of Geophysical Research: Earth Surface* 114.F3.
Campbell, C. S. (2006). "Granular material flows–an overview". In: *Powder Technology* 162.3, pp. 208–229.
Carman, P. C. (1937). "Fluid flow through granular beds". In: *Transactions-Institution of Chemical Engineeres* 15, pp. 150–166.
Carson, M. A. and M. J. Kirkby (1972). *Hillslope form and process*. Vol. 475. Cambridge University Press Cambridge.
Carter, S. P., H. A. Fricker, and M. R. Siegfried (2015). "Active lakes in Antarctica survive on a sedimentary substrate–Part 1: Theory". In: *The Cryosphere Discussions* 9.2, pp. 2053–2099.
Catalano, E., B. Chareyre, and E. Barthélémy (2014). "Pore-scale modeling of fluid-particles interaction and emerging poromechanical effects". In: *International Journal for Numerical and Analytical Methods in Geomechanics* 38.1, pp. 51–71.
Cheng, Y. P., Y. Nakata, and M. D. Bolton (2003). "Discrete element simulation of crushable soil". In: *Geotechnique* 53.7, pp. 633–642.
Chorin, A. J. (1968). "Numerical solution of the Navier-Stokes equations". In: *Mathematics of Computation* 22.104, pp. 745–762.
Christianson, K., L. E. Peters, R. B. Alley, S. Anandakrishnan, R. W. Jacobel, K. L. Riverman, A. Muto, and B. A. Keisling (2014). "Dilatant till facilitates ice-stream flow in northeast Greenland". In: *Earth and Planetary Science Letters* 401, pp. 57–69.
Christoffersen, P. and S. Tulaczyk (2003a). "Response of subglacial sediments to basal freeze-on 1. Theory and comparison to observations from beneath the West Antarctic Ice Sheet". In: *Journal of Geophysical Research: Solid Earth* 108.B4.
— (2003b). "Thermodynamics of basal freeze-on: Predicting basal and subglacial signatures of stopped ice streams and interstream ridges". In: *Annals of Glaciology* 36.1, pp. 233–243.
Clark, C. D. (2010). "Emergent drumlins and their clones: from till dilatancy to flow instabilities". In: *Journal of Glaciology* 56.200, pp. 1011–1025.
Clark, C. D., S. M. Tulaczyk, C. R. Stokes, and M. Canals (2003). "A groove-ploughing theory for the production of mega-scale glacial lineations, and implications for ice-stream mechanics". In: *Journal of Glaciology* 49.165, pp. 240–256.
Clark, P. U. (1994). "Unstable behavior of the Laurentide Ice Sheet over deforming sediment and its implications for climate change". In: *Quaternary Research* 41.1, pp. 19–25.

Clarke, G. K. C. (1987). “Subglacial till: a physical framework for its properties and processes”. In: *Journal of Geophysical Research* 92.B9, pp. 9023–9036.
— (2005). “Subglacial processes”. In: *Annual Review of Earth and Planetary Sciences* 33, pp. 247–276.
Clarke, G. K. C., S. G. Collins, and D. E. Thompson (1984). “Flow, thermal structure, and subglacial conditions of a surge-type glacier”. In: *Canadian Journal of Earth Sciences* 21.2, pp. 232–240.
Clement, E. (1999). “Rheology of granular media”. In: *Current Opinion in Colloid & Interface Science* 4.4, pp. 294–299.
Courant, R., K. Friedrichs, and H. Lewy (1967). “On the partial difference equations of mathematical physics”. In: *IBM Journal of Research and Development* 11.2, pp. 215–234.
Creyts, T. T. and C. G. Schoof (2009). “Drainage through subglacial water sheets”. In: *Journal of Geophysical Research: Earth Surface* 114.F4.
Cuffey, K. M. and R. B. Alley (1996). “Is erosion by deforming subglacial sediments significant? (Toward till continuity)”. In: *Annals of Glaciology* 22, pp. 17–24.
Cuffey, K. M. and W. S. B. Paterson (2010). “The Physics of Glaciers”. In: *Elsevier* 4, p. 693.
Cundall, P. A and O. D. L. Strack (1979). “A discrete numerical model for granular assemblies”. In: *Géotechnique* 29, pp. 47–65.
Damsgaard, A., D. L. Egholm, J. A. Piotrowski, S. Tulaczyk, N. K. Larsen, and K. Tylmann (2013). “Discrete element modeling of subglacial sediment deformation”. In: *Journal of Geophysical Research: Earth Surface* 118, pp. 2230–2242. doi: 10.1002/2013JF002830.
De Angelis, H. and P. Skvarca (2003). “Glacier surge after ice shelf collapse”. In: *Science* 299.5612, pp. 1560–1562.
De Rydt, J., G. H. Gudmundsson, H. Rott, and J. L. Bamber (2015). “Modelling the instantaneous response of glaciers after the collapse of the Larsen B Ice Shelf”. In: *Geophysical Research Letters*. 2015GL064355, n/a–n/a. issn: 1944-8007. doi: 10.1002/2015GL064355. url: http://dx.doi.org/10.1002/2015GL064355.
Denton, G. H. and T.J. Hughes (1981). *The last great ice sheets*. John Wiley & Sons.
Dewhurst, D. N., K. M. Brown, M. B. Clennell, and G. K. Westbrook (1996). “A comparison of the fabric and permeability anisotropy of consolidated and sheared silty clay”. In: *Engineering Geology* 42.4, pp. 253–267.
Di Felice, R. (1994). “The voidage function for fluid-particle interaction systems”. In: *International Journal of Multiphase Flow* 20.1, pp. 153–159.
Drake, T. G. and J. Calantoni (2001). “Discrete particle model for sheet flow sediment transport”. In: *Journal of Geophysical Research* 106, pp. 19–859.
Dunlop, P., C. D. Clark, and R. C. A. Hindmarsh (2008). “Bed ribbing instability explanation: testing a numerical model of ribbed moraine formation arising from coupled flow of ice and subglacial sediment”. In: *Journal of Geophysical Research: Earth Surface* 113.F3.
Dupont, T. K. and R. B. Alley (2005). “Assessment of the importance of ice-shelf buttressing to ice-sheet flow”. In: *Geophysical Research Letters* 32.4.
Egholm, D. L., M. Sandiford, O. R. Clausen, and S. B. Nielsen (2007). “A new strategy for discrete element numerical models. 2. Sandbox applications”. In: *Journal of Geophysical Research* 112.B05204, doi:10.1029/2006JB004558.

Egholm, D. L., O. R. Clausen, M. Sandiford, M. B. Kristensen, and J. A. Korstgård (2008). "The mechanics of clay smearing along faults". In: *Geology* 36.10, pp. 787–790.

Eisenstadt, G. and D. Sims (2005). "Evaluating sand and clay models: do rheological differences matter?" In: *Journal of Structural Geology* 27.8, pp. 1399–1412.

Elias, S. (2006). *Encyclopedia of Quaternary Science*. Elsevier.

Engelhardt, H. and B. Kamb (1997). "Basal hydraulic system of a West Antarctic ice stream: Constraints from borehole observations". In: *Journal of Glaciology* 43.144, pp. 207–230.

— (1998). "Basal sliding of ice stream B, West Antarctica". In: *Journal of Glaciology* 44.147, pp. 223–230.

Engelhardt, H., N. Humphrey, B. Kamb, and M. Fahnestock (1990). "Physical conditions at the base of a fast moving Antarctic ice stream". In: *Science* 248.4951, pp. 57–59.

Ergun, S. (1952). "Fluid flow through packed columns". In: *Chemical Engineering Progress* 43.2, pp. 89–94.

Evans, D. J. A. and B. R. Rea (1999). "Geomorphology and sedimentology of surging glaciers: a land-systems approach". In: *Annals of Glaciology* 28.1, pp. 75–82.

Evans, D. J. A., E. R. Phillips, J. F. Hiemstra, and C. A. Auton (2006). "Subglacial till: formation, sedimentary characteristics and classification". In: *Earth-Science Reviews* 78.1-2, pp. 115–176.

Evans, D., ed. (2005). *Glacial Landsystems*. Hodder Arnold.

Exner, F. M. (1925). "Uber die wechselwirkung zwischen wasser und geschiebe in flüssen". In: *Akad. Wiss. Wien Math. Naturwiss. Klasse* 134.2a, pp. 165–204.

Feng, Y. Q. and A. B. Yu (2004). "Assessment of model formulations in the discrete particle simulation of gas-solid flow". In: *Industrial & engineering chemistry research* 43.26, pp. 8378–8390.

Feng, Y. T., K. Han, D. R. J. Owen, and J. Loughran (2009). "On upscaling of discrete element models: similarity principles". In: *Engineering Computations* 26.6, pp. 599–609.

Ferziger, J. H. and M. Perić (2002). *Computational Methods for Fluid Dynamics*. Vol. 3. Springer Berlin.

Fischer, U. H. and G. K. C. Clarke (1994). "Ploughing of subglacial sediment". In: *Journal of Glaciology* 40, pp. 97–106.

— (1997). "Stick-slip sliding behaviour at the base of a glacier". In: *Annals of Glaciology* 24, pp. 390–396.

— (2001). "Review of subglacial hydro-mechanical coupling: Trapridge glacier, Yukon Territory, Canada". In: *Quaternary International* 86.1, pp. 29–43.

Fischer, U. H., P. R. Porter, T. Schuler, A. J. Evans, and G. H. Gudmundsson (2001). "Hydraulic and mechanical properties of glacial sediments beneath Unteraargletscher, Switzerland: implications for glacier basal motion". In: *Hydrological Processes* 15.18, pp. 3525–3540.

Flowers, G. E. (2015). "Modelling water flow under glaciers and ice sheets". In: *Proceedings of the Royal Society of London A*. Vol. 471. 2176. The Royal Society, p. 20140907.

Fowler, A. C. (1981). "A theoretical treatment of the sliding of glaciers in the absence of cavitation". In: *Philosophical Transactions of the Royal Society of London A* 298.1445, pp. 637–681.

— (1986). “A sliding law for glaciers of constant viscosity in the presence of subglacial cavitation”. In: *Proceedings of the Royal Society of London A*. Vol. 407. 1832. The Royal Society, pp. 147–170.
— (1987). “Sliding with cavity formation”. In: *Journal of Glaciology* 33.115, pp. 255–267.
— (2000). “An instability mechanism for drumlin formation”. In: *Geological Society, London, Special Publications* 176.1, pp. 307–319.
— (2003). “On the rheology of till”. In: *Annals of Glaciology* 37.1, pp. 55–59.
— (2010). “The formation of subglacial streams and mega-scale glacial lineations”. In: *Proceedings of the Royal Society of London A*. Vol. 466. 2123. The Royal Society, pp. 3181–3201.
Fowler, A. and J. Walder (1993). “Creep closure of channels in deforming subglacial till”. In: *Proceedings of the Royal Society of London A*. Vol. 441. 1911. The Royal Society, pp. 17–31.
Fraige, F. Y. and P. A. Langston (2004). “Integration schemes and damping algorithms in distinct element models”. In: *Advanced Powder Technology* 15.2, pp. 227–245.
GDR-MiDi (2004). “On dense granular flows”. In: *European Physics Journal E* 14, pp. 341–365.
Galindo-Torres, S. A., A. Lizcano, and J. D. Muñoz (2012). “Effect of frictional heat dissipation on the loss of soil strength”. In: *Physical Review E* 86.6, p. 061302.
Gennes, P. G. de (1999). “Granular matter: a tentative view”. In: *Reviews of modern physics* 71.2, pp. 374–382.
Gerya, T. (2010). *Introduction to Numerical Geodynamic Modelling*. Cambridge University Press, Cambridge.
Gidaspow, D. (1994). *Multiphase Flow and Fluidization*. Academic Press, San Diego.
Gidaspow, D., R. Bezburuah, and J. Ding (1992). *Hydrodynamics of circulating fluidized beds: kinetic theory approach*. Tech. rep. Illinois Inst. of Tech., Chicago, IL (United States). Dept. of Chemical Engineering.
Gleason, G. C. and J. Tullis (1995). “A flow law for dislocation creep of quartz aggregates determined with the molten salt cell”. In: *Tectonophysics* 247.1, pp. 1–23.
Glen, J. W. (1955). “The creep of polycrystalline ice”. In: *Proceedings of the Royal Society of London A: Mathematical, Physical and Engineering Sciences*. Vol. 228. 1175. The Royal Society, pp. 519–538.
Goldberg, D. N., C. Schoof, and O. V. Sergienko (2014). “Stick-slip motion of an Antarctic Ice Stream: The effects of viscoelasticity”. In: *Journal of Geophysical Research: Earth Surface* 119.7, pp. 1564–1580.
Goren, L. and E. Aharonov (2007). “Long runout landslides: The role of frictional heating and hydraulic diffusivity”. In: *Geophysical Research Letters* 34.7.
Goren, L., E. Aharonov, D. Sparks, and R. Toussaint (2010). “Pore pressure evolution in deforming granular material: A general formulation and the infinitely stiff approximation”. In: *Journal of Geophysical Research: Solid Earth* 115.B9.
— (2011). “The mechanical coupling of fluid-filled granular material under shear”. In: *Pure and Applied Geophysics* 168.12, pp. 2289–2323.
Griebel, M., T. Dornseifer, and T. Neunhoeffer (1998). *Numerical simulation in fluid dynamics*. Society for Industrial and Applied Mathematics.
Grinsted, A., J. C. Moore, and S. Jevrejeva (2010). “Reconstructing sea level from paleo and projected temperatures 200 to 2100 AD”. In: *Climate Dynamics* 34.4, pp. 461–472.

Gu, Y., S. Chialvo, and S. Sundaresan (2014). “Rheology of cohesive granular materials across multiple dense-flow regimes”. In: *Physical Review E* 90.3, p. 032206.
Gudmundsson, G. H. (2006). “Fortnightly variations in the flow velocity of Rutford Ice Stream, West Antarctica”. In: *Nature* 444.7122, pp. 1063–1064.
— (2007). “Tides and the flow of Rutford ice stream, West Antarctica”. In: *Journal of Geophysical Research: Earth Surface* 112.F4.
— (2011). “Ice-stream response to ocean tides and the form of the basal sliding law”. In: *The Cryosphere* 5.1, pp. 259–270.
Haldorsen, S. (1981). “Grain-size distribution of subglacial till and its relation to glacial crushing and abrasion”. In: *Boreas* 10.1, pp. 91–105.
Hallet, B., L. Hunter, and J. Bogen (1996). “Rates of erosion and sediment evacuation by glaciers: A review of field data and their implications”. In: *Global and Planetary Change* 12.1, pp. 213–235.
Handwerger, A. L., J. J. Roering, D. A. Schmidt, and A. W. Rempel (2015). “Kinematics of Earthflows in the Northern California Coast Ranges using Satellite Interferometry”. In: *Geomorphology*.
Harleman, D. R. F., P. F. Mehlhorn, and R. R. Rumer (1963). “Dispersion-permeability correlation in porous media”. In: *Journal of the Hydraulics Division American Society of Civil Engineers* 89, pp. 67–85.
Hart, J. K. (1994). “Till fabric associated with deformable beds”. In: *Earth Surface Processes and Landforms* 19.1, pp. 15–32.
— (1998). “The deforming bed/debris-rich basal ice continuum and its implications for the formation of glacial landforms (flutes) and sediments (melt-out till)”. In: *Quaternary Science Reviews* 17.8, pp. 737–754.
Hart, J. K., K. Martinez, R. Ong, A. Riddoch, K. C. Rose, and P. Padhy (2006). “A wireless multi-sensor subglacial probe: design and preliminary results”. In: *Journal of Glaciology* 52.178, pp. 389–397.
Hart, J. K., K. C. Rose, K. Martinez, and . Ong (2009). “Subglacial clast behaviour and its implication for till fabric development: new results derived from wireless subglacial probe experiments”. In: *Quaternary Science Reviews* 28.7, pp. 597–607.
Hart, J. K., K. C. Rose, and K. Martinez (2011). “Subglacial till behaviour derived from in situ wireless multi-sensor subglacial probes: Rheology, hydromechanical interactions and till formation”. In: *Quaternary Science Reviews* 30.1, pp. 234–247.
Hazen, A. (1911). “Discussion of dams on sand formation”. In: *Transactions of the American Society of Civil Engineers* 73, pp. 199–221.
Henderson, A., J. Ahrens, and C. Law (2007). *The ParaView Guide*. Kitware Clifton Park, NY.
Herrmann, H. J. (2001). “Structures in deformed granular packings”. In: *Granular Matter* 3.1, pp. 15–18.
— (2002). “Granular matter”. In: *Physica A: Statistical Mechanics and Its Applications* 313.1-2, pp. 188–210.
Hertz, H. (1882). “Über die Berührung fester elastischer Körper”. In: *J. reine angewandte Mathematik* 92, pp. 239–245.
Hewitt, I. J. (2011). “Modelling distributed and channelized subglacial drainage: the spacing of channels”. In: *Journal of Glaciology* 57.202, pp. 302–314.
Hicock, S. R. and A. Dreimanis (1992). “Deformation till in the Great Lakes region: implications for rapid flow along the south-central margin of the Laurentide Ice Sheet”. In: *Canadian Journal of Earth Sciences* 29.7, pp. 1565–1579.

Hiemstra, J. F. and K. F. Rijsdijk (2003). “Observing artificially induced strain: implications for subglacial deformation”. In: *Journal of Quaternary Science* 18.5, pp. 373–383.
Hindmarsh, R. C. A. (1997). “Deforming beds: viscous and plastic scales of deformation”. In: *Quaternary Science Reviews* 16.9, pp. 1039–1056.
— (1998). “The stability of a viscous till sheet coupled with ice flow, considered at wavelengths less than the ice thickness”. In: *Journal of Glaciology* 44.147, pp. 285–292.
Hinrichsen, H. and D. E. Wolf (2004). *The Physics of Granular Media*. Wiley-VCH.
Hjulstrom, F. (1939). “Transportation of detritus by moving water: Part 1. Transportation”. In:
Hooke, R. LeB. (1981). “Flow law for polycrystalline ice in glaciers: comparison of theoretical predictions, laboratory data, and field”. In: *Rev. Geophys. Space Phys* 19.4, pp. 664–672.
Hooke, R. LeB. and N. R. Iverson (1995). “Grain-size distribution in deforming subglacial tills: role of grain fracture”. In: *Geology* 23.1, pp. 57–60.
Hooke, R. LeB., B. Hanson, N. R. Iverson, P. Jansson, and U. H. Fischer (1997). “Rheology of till beneath Storglaciären, Sweden”. In: *Journal of Glaciology* 43.143, pp. 172–179.
Hoomans, B. P. B., J. A. M. Kuipers, W. J. Briels, and W. P. M. Van Swaaij (1996). “Discrete particle simulation of bubble and slug formation in a two-dimensional gas-fluidised bed: a hard-sphere approach”. In: *Chemical Engineering Science* 51.1, pp. 99–118.
Hooyer, T. S. and N. R. Iverson (2000a). “Clast-fabric development in a shearing granular material: Implications for subglacial till and fault gouge”. In: *Geological Society of America Bulletin* 112.5, p. 683.
— (2000b). “Diffusive mixing between shearing granular layers: constraints on bed deformation from till contacts”. In: *Journal of Glaciology* 46.155, pp. 641–651.
Hubbard, B. and M. Sharp (1989). “Basal ice formation and deformation: a review”. In: *Progress in Physical Geography* 13.4, pp. 529–558.
Hunter, J. D. (2007). “Matplotlib: A 2D graphics environment”. In: *Computing In Science & Engineering* 9.3, pp. 90–95.
Hutter, K., B. Svendsen, and D. Rickenmann (1994). “Debris flow modeling: A review”. In: *Continuum Mechanics and Thermodynamics* 8.1, pp. 1–35.
Huybrechts, P. and J. de Wolde (1999). “The dynamic response of the Greenland and Antarctic ice sheets to multiple-century climatic warming”. In: *Journal of Climate* 12.8, pp. 2169–2188.
IPCC (2013). *Climate Change 2013: The Physical Science Basis. Contribution of Working Group I to the Fifth Assessment Report of the Intergovernmental Panel on Climate Change*. Ed. by T. F. Stocker, D. Qin, G.-K. Plattner, M. Tignor, S. K. Allen, J. Boschung, A. Nauels, Y. Xia, V. Bex, and P. M. Midgley. Cambridge University Press Cambridge, United Kingdom, and New York, NY, USA, p. 1535.
Iken, A. (1981). “The effect of the subglacial water pressure on the sliding velocity of a glacier in an idealized numerical model”. In: *Journal of Glaciology* 27.97, pp. 407–421.
Iken, A. and M. Truffer (1997). “The relationship between subglacial water pressure and velocity of Findelengletscher, Switzerland, during its advance and retreat”. In: *Journal of Glaciology* 43.144, pp. 328–338.

Iverson, N. R. (1999). “Coupling between a glacier and a soft bed: II. Model results”. In: *Journal of Glaciology* 45.149, pp. 41–53.
— (2010). “Shear resistance and continuity of subglacial till: hydrology rules”. In: *Journal of Glaciology* 56.200, p. 1104.
Iverson, N. R. and R. M. Iverson (2001). “Distributed shear of subglacial till due to Coulomb slip”. In: *Journal of Glaciology* 47.158, pp. 481–488.
Iverson, N. R. and L. K. Zoet (2015). “Experiments on the dynamics and sedimentary products of glacier slip”. In: *Geomorphology*.
Iverson, N. R., P. Jansson, and R. LeB. Hooke (1994). “In-situ measurement of the strength of deforming subglacial till”. In: *Journal of Glaciology* 40.136, pp. 497–503.
Iverson, N. R., B. Hanson, R. LeB. Hooke, and P. Jansson (1995). “Flow mechanism of glaciers on soft beds”. In: *Science* 267.5194, p. 80.
Iverson, N. R., T. S. Hooyer, and R. LeB. Hooke (1996). “A laboratory study of sediment deformation: stress heterogeneity and grain-size evolution”. In: *Annals of Glaciology* 22, pp. 167–175.
Iverson, N. R., R. W. Baker, and T. S. Hooyer (1997a). “A ring-shear device for the study of till deformation: tests on tills with contrasting clay contents”. In: *Quaternary Science Reviews* 16.9, pp. 1057–1066.
Iverson, N. R., T. S. Hooyer, and R. W. Baker (1998). “Ring-shear studies of till deformation: Coulomb-plastic behavior and distributed strain in glacier beds”. In: *Journal of Glaciology* 148, pp. 634–642.
Iverson, N. R., R. W. Baker, R. LeB. Hooke, B. Hanson, and P. Jansson (1999). “Coupling between a glacier and a soft bed: I. A relation between effective pressure and local shear stress determined from till elasticity”. In: *Journal of Glaciology* 45.149, pp. 31–40.
Iverson, N. R., T. S. Hooyer, U. H. Fischer, D. Cohen, P. L. Moore, M. Jackson, G. Lappegard, and J. Kohler (2007). “Soft-bed experiments beneath Engabreen, Norway: regelation infiltration, basal slip and bed deformation”. In: *Journal of Glaciology* 53.182, pp. 323–340.
Iverson, N. R., T. S. Hooyer, J. F. Thomason, M. Graesch, and J. R. Shumway (2008). “The experimental basis for interpreting particle and magnetic fabrics of sheared till”. In: *Earth Surface Processes and Landforms* 33.4, pp. 627–645.
Iverson, N. R., J. E. Mann, and R. M. Iverson (2010). “Effects of soil aggregates on debris-flow mobilization: results from ring-shear experiments”. In: *Engineering Geology* 114.1, pp. 84–92.
Iverson, R. M. (1986). “Unsteady, nonuniform landslide motion: 2. Linearized theory and the kinematics of transient response”. In: *The Journal of Geology*, pp. 349–364.
Iverson, R. M. and J. J. Major (1987). “Rainfall, ground-water flow, and seasonal movement at Minor Creek landslide, northwestern California: Physical interpretation of empirical relations”. In: *Geological Society of America Bulletin* 99.4, pp. 579–594.
Iverson, R. M., M. E. Reid, and R. G. LaHusen (1997b). “Debris-flow mobilization from landslides”. In: *Annual Review of Earth and Planetary Sciences* 25.1, pp. 85–138.
Jaeger, H. M. and S. R. Nagel (1992). “Physics of the granular state”. In: *Science* 255.5051, pp. 1523–1531.
Jaeger, H. M., S. R. Nagel, and R. P. Behringer (1996). “Granular solids, liquids, and gases”. In: *Reviews of Modern Physics* 68.4, pp. 1259–1273.

Jajcevic, D., E. Siegmann, C. Radeke, and J. G. Khinast (2013). “Large-scale CFD–DEM simulations of fluidized granular systems”. In: *Chemical Engineering Science* 98, pp. 298–310.

Jeffery, G. B. (1922). “The motion of ellipsoidal particles immersed in a viscous fluid”. In: *Proceedings of the Royal Society of London. Series A, Containing Papers of a Mathematical and Physical Character* 102.715, pp. 161–179.

Jenson, J. W., P. U. Clark, D. R. MacAyeal, C. Ho, and J. C. Vela (1995). “Numerical modeling of advective transport of saturated deforming sediment beneath the Lake Michigan Lobe, Laurentide Ice Sheet”. In: *Geomorphology* 14.2, pp. 157–166.

Jenson, J. W., D. R. MacAyeal, P. U. Clark, C. L. Ho, and J. C. Vela (1996). “Numerical modeling of subglacial sediment deformation: Implications for the behavior of the Lake Michigan Lobe, Laurentide Ice Sheet”. In: *Journal of Geophysical Research: Solid Earth* 101.B4, pp. 8717–8728.

Johnson, K. L. (1985). *Contact mechanics*. Cambridge Univ Press.

Joughin, I., M. Fahnestock, D. MacAyeal, J. L. Bamber, and P. Gogineni (2001). “Observation and analysis of ice flow in the largest Greenland ice stream”. In: *Journal of Geophysical Research: Atmospheres (1984–2012)* 106.D24, pp. 34021–34034.

Joughin, I., D. R. MacAyeal, and S. Tulaczyk (2004). “Basal shear stress of the Ross ice streams from control method inversions”. In: *Journal of Geophysical Research: Solid Earth* 109.B9.

Joughin, I., S. Tulaczyk, J. L. Bamber, D. Blankenship, J. W. Holt, T. Scambos, and D. G. Vaughan (2009). “Basal conditions for Pine Island and Thwaites Glaciers, West Antarctica, determined using satellite and airborne data”. In: *Journal of Glaciology* 55.190, pp. 245–257.

Joughin, I., B. E. Smith, and B. Medley (2014). “Marine ice sheet collapse potentially under way for the Thwaites Glacier Basin, West Antarctica”. In: *Science* 344.6185, pp. 735–738.

Kamb, B. (1970). “Sliding motion of glaciers: theory and observation”. In: *Reviews of Geophysics* 8.4, pp. 673–728.

— (1991). “Rheological nonlinearity and flow instability in the deforming bed mechanism of ice stream motion”. In: *Journal of Geophysical Research* 96.B10, pp. 16585–16.

— (2001). “Basal zone of the West Antarctic ice streams and its role in lubrication of their rapid motion”. In: *The West Antarctic Ice Sheet: Behavior and Environment*, pp. 157–199.

Kavanaugh, J. L. and G. K. C. Clarke (2006). “Discrimination of the flow law for subglacial sediment using in situ measurements and an interpretation model”. In: *Journal of Geophysical Research: Earth Surface* 111.F1.

Kennedy, J. F. (1969). “The formation of sediment ripples, dunes, and antidunes”. In: *Annual Review of Fluid Mechanics* 1.1, pp. 147–168.

King, M. A., T. Murray, and A. M. Smith (2010). “Non-linear responses of Rutford Ice Stream, Antarctica, to semi-diurnal and diurnal tidal forcing”. In: *Journal of Glaciology* 56.195, pp. 167–176.

King, M. A., K. Makinson, and G. H. Gudmundsson (2011). “Nonlinear interaction between ocean tides and the Larsen C Ice Shelf system”. In: *Geophysical Research Letters* 38.8.

Kirk, D. B. and W-M. W. Hwu (2010). *Programming Massively Parallel Processors*. Morgan Kaufmann, Elsevier.

Kirkby, M. J. (1967). “Measurement and theory of soil creep”. In: *The Journal of Geology*, pp. 359–378.

Kjær, K. H., E. Larsen, J. van der Meer, Ó. Ingólfsson, J. Krüger, Í. Örn Benediktsson, C. G. Knudsen, and A. Schomacker (2006). “Subglacial decoupling at the sediment/bedrock interface: a new mechanism for rapid flowing ice”. In: *Quaternary Science Reviews* 25.21, pp. 2704–2712.

Kloss, C., C. Goniva, A. Hager, S. Amberger, and S. Pirker (2012). “Models, algorithms and validation for opensource DEM and CFD-DEM”. In: *Progress in Computational Fluid Dynamics* 12.2/3, pp. 140–152.

Kozeny, J. (1927). “Ueber kapillare leitung des wassers im boden”. In: *Sitzungsbericht der Akademie der Wissenschaften Wien* 136, pp. 271–306.

Krimer, D. O., S. Mahle, and M. Liu (2012). “Dip of the granular shear stress”. In: *Physical Review E* 86 (6), p. 061312.

Kruggel-Emden, H., E. Simsek, S. Rickelt, S. Wirtz, and V. Scherer (2007). “Review and extension of normal force models for the discrete element method”. In: *Powder Technology* 171.3, pp. 157–173.

Kruggel-Emden, H., M. Sturm, S. Wirtz, and V. Scherer (2008). “Selection of an appropriate time integration scheme for the discrete element method (DEM)”. In: *Computers & Chemical Engineering* 32.10, pp. 2263–2279.

Krumbein, W. C. and G. D. Monk (1943). “Permeability as a function of the size parameters of unconsolidated sand”. In: *Transactions of the American Institute of Mining Engineers* 151.01, pp. 153–163.

Kudrolli, A. (2004). “Size separation in vibrated granular matter”. In: *Reports on progress in Physics* 67, p. 209.

Kyrke-Smith, T. M. and A. C. Fowler (2014). “Subglacial swamps”. In: *Proceedings of the Royal Society A: Mathematical, Physical and Engineering Science* 470.2171, p. 20140340.

Kyrke-Smith, T. M., R. F. Katz, and A. C. Fowler (2014). “Subglacial hydrology and the formation of ice streams”. In: *Proceedings of the Royal Society A: Mathematical, Physical and Engineering Science* 470.2161, p. 20130494.

Langtangen, H. P., K.-A. Mardal, and R. Winther (2002). “Numerical methods for incompressible viscous flow”. In: *Advances in Water Resources* 25.8, pp. 1125–1146.

Larsen, N. K. and J. A. Piotrowski (2003). “Fabric pattern in a basal till succession and its significance for reconstructing subglacial processes”. In: *Journal of Sedimentary Research* 73.5, pp. 725–734.

Larsen, N. K., J. A. Piotrowski, and C. Kronborg (2004). “A multiproxy study of a basal till: a time-transgressive accretion and deformation hypothesis”. In: *Journal of Quaternary Science* 19.1, pp. 9–21.

Larsen, N. K., J. A. Piotrowski, and F. Christiansen (2006). “Microstructures and microshears as proxy for strain in subglacial diamicts: Implications for basal till formation”. In: *Geology* 34.10, p. 889.

Larsen, N. K., J. A. Piotrowski, and J. Menzies (2007). “Microstructural evidence of low-strain, time-transgressive subglacial deformation”. In: *Journal of Quaternary Science* 22.6, pp. 593–608.

Li, Y. R. and A. Aydin (2010). “Behavior of rounded granular materials in direct shear: Mechanisms and quantification of fluctuations”. In: *Engineering Geology* 115.1-2, pp. 96–104.

Lingle, C. S. and T. J. Brown (1987). “A subglacial aquifer bed model and water pressure dependent basal sliding relationship for a West Antarctic ice stream”. In: *Dynamics of the West Antarctic ice sheet*. Springer, pp. 249–285.
Lliboutry, L. (1968). “General theory of subglacial cavitation and sliding of temperate glaciers”. In: *Journal of Glaciology* 7, pp. 21–58.
Luding, S. (2008). “Introduction to discrete element methods: basic of contact force models and how to perform the micro-macro transition to continuum theory”. In: *European Journal of Environmental and Civil Engineering* 12.7-8, pp. 785–826.
MacAyeal, D. R. (1992). “Irregular oscillations of the West Antarctic ice sheet”. In: *Nature* 359.6390, pp. 29–32.
MacAyeal, D. R., R. A. Bindschadler, and T. A. Scambos (1995). “Basal friction of Ice Stream E, West Antarctica”. In: *Journal of Glaciology* 41.138, pp. 247–262.
MacClintock, P. and A. Dreimanis (1964). “Orientation of till fabric by overriding glacier in the Saint Lawrence Valley”. In: *American Journal of Science* 262.1, pp. 133–142.
Mair, K. and S. Abe (2008). “3D numerical simulations of fault gouge evolution during shear: Grain size reduction and strain localization”. In: *Earth and Planetary Science Letters* 274.1-2, pp. 72–81.
Mair, K. and J. F. Hazzard (2007). “Nature of stress accommodation in sheared granular material: Insights from 3D numerical modeling”. In: *Earth and Planetary Science Letters* 259.3, pp. 469–485.
Mair, K., K. M. Frye, and C. Marone (2002). “Influence of grain characteristics on the friction of granular shear zones”. In: *Journal of Geophysical Research: Solid Earth* 107.B10, ECV–4.
Malet, J.-P., O. Maquaire, and E. Calais (2002). “The use of Global Positioning System techniques for the continuous monitoring of landslides: application to the Super-Sauze earthflow (Alpes-de-Haute-Provence, France)”. In: *Geomorphology* 43.1, pp. 33–54.
Mangeney, A., L. S. Tsimring, D. Volfson, I. S. Aranson, and F. Bouchut (2007). “Avalanche mobility induced by the presence of an erodible bed and associated entrainment”. In: *Geophysical Research Letters* 34.22.
March, A. (1932). “Mathematische Theorie der Regelung nach der Korngestalt bei affiner Deformation”. In: *Zeitschrift für Kristallographie* 81, pp. 285–297.
Mark, D. M. (1973). “Analysis of axial orientation data, including till fabrics”. In: *Geological Society of America Bulletin* 84.4, pp. 1369–1374.
Martinez, K., J. K. Hart, and R. Ong (2009). “Deploying a wireless sensor network in Iceland”. In: *GeoSensor Networks*. Springer, pp. 131–137.
McGee, W.J. (1894). “Glacial cañons”. In: *The Journal of Geology* 2.4, pp. 350–364.
McNamara, S., E. G. Flekkøy, and K. J. Måløy (2000). “Grains and gas flow: Molecular dynamics with hydrodynamic interactions”. In: *Physical Review E* 61 (4), pp. 4054–4059.
Mead, W. J. (1925). “The geologic role of dilatancy”. In: *Journal of Geology* 33.7, pp. 685–698.
Meer, J. J. M. van der (1993). “Microscopic evidence of subglacial deformation”. In: *Quaternary Science Reviews* 12.7, pp. 553–587.
— (1996). “Micromorphology.” In: *Glacial environments, vol. 2: Past glacial environments-processes, sediments and landforms*, pp. 335–355.
— (1997). “Particle and aggregate mobility in till: microscopic evidence of subglacial processes”. In: *Quaternary Science Reviews* 16.8, pp. 827–831.

Menzies, J. (2000). “Micromorphological analyses of microfabrics and microstructures indicative of deformation processes in glacial sediments”. In: *Geological Society, London, Special Publications* 176.1, pp. 245–257.
Mitchell, J. K. and K. Soga (2005). *Fundamentals of soil behavior*. Wiley New York.
Moore, P. L. and N. R. Iverson (2002). “Slow episodic shear of granular materials regulated by dilatant strengthening”. In: *Geology* 30.9, pp. 843–846.
Morgan, J. K. (1999). “Numerical simulations of granular shear zones using the distinct element method 2. Effects of particle size distribution and interparticle friction on mechanical behavior”. In: *Journal of Geophysical Research* 104.B2, pp. 2721–2732.
— (2004). “Particle Dynamics Simulations of Rate- and State-dependent Frictional Sliding of Granular Fault Gouge”. In: *Pure and Applied Geophysics* 161.9, pp. 1877–1891.
Morgan, J. K. and M. S. Boettcher (1999). “Numerical simulations of granular shear zones using the distinct element method 1. Shear zone kinematics and the micromechanics of localization”. In: *Journal of Geophysical Research* 104.B2, pp. 2703–2719.
Morgan, V. I., T. H. Jacka, G. J. Akerman, and A. L. Clarke (1983). “Outlet glacier and mass-budget studies in Enderby, Kemp and Mac. Robertson lands, Antarctica”. In: *Annals of Glaciology* 3, pp. 204–210.
Mueth, D. M., G. F. Debregeas, G. S. Karczmar, P. J. Eng, S. R. Nagel, and H. M. Jaeger (2000). “Signatures of granular microstructure in dense shear flows”. In: *Nature* 406.6794, pp. 385–389.
Müller, B. U. and C. Schlüchter (2000). “Influence of the glacier bed lithology on the formation of a subglacial till sequence–ring-shear experiments as a tool for the classification of subglacial tills”. In: *Quaternary Science Reviews* 20.10, pp. 1113–1125.
Murray, T. (1997). “Assessing the paradigm shift: deformable glacier beds”. In: *Quaternary Science Reviews* 16.9, pp. 995–1016.
Murray, T and G. K. C. Clarke (1995). “Black-box modeling of the subglacial water system”. In: *Journal of Geophysical Research: Solid Earth* 100.B6, pp. 10231–10245.
Murray, T., G. W. Stuart, P. J. Miller, J. Woodward, A. M. Smith, P. R. Porter, and H. Jiskoot (2000). “Glacier surge propagation by thermal evolution”. In: *Journal of Geophysical Research* 105.B6, pp. 13–491.
Murray, T., T. Strozzi, A. Luckman, H. Jiskoot, and P. Christakos (2003). “Is there a single surge mechanism? Contrasts in dynamics between glacier surges in Svalbard and other regions”. In: *Journal of Geophysical Research* 108.B5, p. 2237.
Mutabaruka, P., J.-Y. Delenne, K. Soga, and F. Radjai (2014). “Initiation of immersed granular avalanches”. In: *Physical Review E* 89.5, p. 052203.
NVIDIA (2013a). *CUDA C Best Practices Guide Version*. 5.0. CA Patent 95,050. NVIDIA Corporation: Santa Clara, CA, USA.
— (2013b). *CUDA C Programming Guide*. 5.0. NVIDIA Corporation: Santa Clara, CA, USA, 183 pp.
Nedderman, R. M. (1992). *Statics and kinematics of granular materials*. Cambridge University Press, Cambridge.
Ng, F. S. L. (2000a). “Canals under sediment-based ice sheets”. In: *Annals of Glaciology* 30, pp. 146–152.
— (2000b). “Coupled ice-till deformation near subglacial channels and cavities”. In: *Journal of Glaciology* 46.155, pp. 580–598.

Nye, J. F. (1952). “The mechanics of glacier flow”. In: *Journal of Glaciology* 2.12, pp. 82–93.
— (1976). “Water flow in glaciers: jökulhlaups, tunnels and veins”. In: *Journal of Glaciology* 17, pp. 181–207.
Nygård, A., H. P. Sejrup, H. Haflidason, W. A. H. Lekens, C. D. Clark, and G. R. Bigg (2007). “Extreme sediment and ice discharge from marine-based ice streams: New evidence from the North Sea”. In: *Geology* 35.5, pp. 395–398.
O’Sullivan, C. and J. D. Bray (2004). “Selecting a suitable time step for discrete element simulations that use the central difference time integration scheme”. In: *Engineering Computations: Int J for Computer-Aided Engineering, 21* 2.3, pp. 278–303.
Obermayr, M., K. Dressler, C. Vrettos, and P. Eberhard (2013). “A bonded-particle model for cemented sand”. In: *Computers and Geotechnics* 49, pp. 299–313.
Okada, Y., K. Sassa, and H. Fukuoka (2004). “Excess pore pressure and grain crushing of sands by means of undrained and naturally drained ring-shear tests”. In: *Engineering geology* 75.3-4, pp. 325–343.
Overpeck, J. T., B. L. Otto-Bliesner, G. H. Miller, D. R. Muhs, R. B. Alley, and J. T. Kiehl (2006). “Paleoclimatic evidence for future ice-sheet instability and rapid sea-level rise”. In: *Science* 311.5768, pp. 1747–1750.
Pailha, M., M. Nicolas, and O. Pouliquen (2008). “Initiation of underwater granular avalanches: Influence of the initial volume fraction”. In: *Physics of Fluids* 20.11, p. 111701.
Paolo, F. S., H. A. Fricker, and L. Padman (2015). “Volume loss from Antarctic ice shelves is accelerating”. In: *Science* 348.6232, pp. 327–331.
Patankar, S. V. (1980). *Numerical Heat Transfer and Fluid Flow*. CRC Press.
Phillips, E., J. Everest, and H. Reeves (2013). “Micromorphological evidence for subglacial multiphase sedimentation and deformation during overpressurized fluid flow associated with with hydrofracturing”. In: *Boreas* 42, pp. 395–427.
Piotrowski, J. A. (1987). “Genesis of the Woodstock drumlin field, southern Ontario, Canada”. In: *Boreas* 16.3, pp. 249–265.
— (1997). “Subglacial hydrology in north-western Germany during the last glaciation: groundwater flow, tunnel valleys and hydrological cycles”. In: *Quaternary Science Reviews* 16.2, pp. 169–185.
Piotrowski, J. A. and S. Tulaczyk (1999). “Subglacial conditions under the last ice sheet in northwest Germany: ice-bed separation and enhanced basal sliding?” In: *Quaternary Science Reviews* 18.6, pp. 737–751.
Piotrowski, J. A., D. M. Mickelson, S. Tulaczyk, D. Krzyszkowski, and F. W. Junge (2001). “Were deforming subglacial beds beneath past ice sheets really widespread?” In: *Quaternary International* 86.1, pp. 139–150.
Piotrowski, J. A., N. K. Larsen, and F. W. Junge (2004). “Reflections on soft subglacial beds as a mosaic of deforming and stable spots”. In: *Quaternary Science Reviews* 23.9, pp. 993–1000.
Piotrowski, J. A., N. K. Larsen, J. Menzies, and W. Wysota (2006). “Formation of subglacial till under transient bed conditions: deposition, deformation, and basal decoupling under a Weichselian ice sheet lobe, central Poland”. In: *Sedimentology* 53.1, pp. 83–106.
Pollard, D. and R. M. DeConto (2009). “Modelling West Antarctic ice sheet growth and collapse through the past five million years”. In: *Nature* 458.7236, pp. 329–332.

Porter, P. R. and T. Murray (2001). “Mechanical and hydraulic properties of till beneath Bakaninbreen, Svalbard”. In: *Journal of Glaciology* 47.157, pp. 167–175.

Potyondy, D. O. and P. A. Cundall (2004). “A bonded-particle model for rock”. In: *International journal of rock mechanics and mining sciences* 41.8, pp. 1329–1364.

Press, W. H., S. A. Teukolsky, W. T. Vetterling, and B. P. Flannery (2007). *Numerical recipes 3rd edition: The art of scientific computing*. Cambridge University Press.

Price, S. F., C. L. Bindschadler, C. L. Hulbe, and D. D. Blankenship (2002). “Force balance along an inland tributary and onset to Ice Stream D, West Antarctica”. In: *Journal of Glaciology* 48.160, pp. 20–30.

Radjaï, F. and F. Dubois (2009). “Contact dynamics as a nonsmooth discrete element method”. In: *Mechanics of Materials* 41, pp. 715–728.

— (2011). *Discrete-Element Modeling of Granular Materials*. Wiley-Iste, p. 425.

Rathbun, A. P, C. Marone, R. B. Alley, and S. Anandakrishnan (2008). “Laboratory study of the frictional rheology of sheared till”. In: *Journal of Geophysical Research* 113.F2, F02020.

Rathbun, A. P., F. Renard, and S. Abe (2013). “Numerical investigation of the interplay between wall geometry and friction in granular fault gouge”. In: *Journal of Geophysical Research: Solid Earth*.

Raymond, C. (1996). “Shear margins in glaciers and ice sheets”. In: *Journal of Glaciology* 42.140, pp. 90–102.

Rempel, A. W., J. R. Rice, and L. M. Jacques (2003). “Fault zone drainage, heating and melting during earthquake slip”. In: *AGU Fall Meeting Abstracts*. Vol. 1, p. 0183.

Reynolds, O. (1885). “On the dilatancy of media composed of rigid particles in contact”. In: *Philosophical Magazine* 20.5, p. 46.

Rignot, E. and R. H. Thomas (2002). “Mass balance of polar ice sheets”. In: *Science* 297.5586, pp. 1502–1506.

Rignot, E., G. Casassa, P. Gogineni, W. Krabill, A.u. Rivera, and R. Thomas (2004). “Accelerated ice discharge from the Antarctic Peninsula following the collapse of Larsen B ice shelf”. In: *Geophysical Research Letters* 31.18.

Rignot, E., J. Mouginot, and B. Scheuchl (2011). “Ice flow of the Antarctic ice sheet”. In: *Science* 333.6048, pp. 1427–1430.

Roering, J. J., J. W. Kirchner, L. S. Sklar, and W. E. Dietrich (2001). “Hillslope evolution by nonlinear creep and landsliding: An experimental study”. In: *Geology* 29.2, pp. 143–146.

Rondon, L., O. Pouliquen, and P. Aussillous (2011). “Granular collapse in a fluid: role of the initial volume fraction”. In: *Physics of Fluids* 23.7, p. 073301.

Rosato, A. D., D. L. Blackmore, N. Zhang, and Y. Lan (2002). “A perspective on vibration-induced size segregation of granular materials”. In: *Chemical Engineering Science* 57.2, pp. 265–275.

Rosier, S. H. R., G. H. Gudmundsson, and J. A. M. Green (2014). “Insights into ice stream dynamics through modelling their response to tidal forcing”. In: *The Cryosphere* 8.5, pp. 1763–1775.

— (2015). “Temporal variations in the flow of a large Antarctic ice-stream controlled by tidally induced changes in the subglacial water system”. In: *The Cryosphere Discussions* 9, pp. 2397–2429.

Röthlisberger, H. (1969). “Water pressure in subglacial channels”. In: *Union Géodésique et Géophysique Internationale. Association Internationale d’Hydrologie Scientifique.*

Commission de Neiges et Glaces. Symposium on the hydrology of Glaciers, Cambridge, 7, p. 97.
— (1972). "Water pressure in intra-and subglacial channels". In: *Journal of Glaciology* 11.62, pp. 177–203.
Ruddiman, W. F. (2007). *Earth's Climate: past and future*. Macmillan.
Rudnicki, J. W. and J. R. Rice (1975). "Conditions for the localization of deformation in pressure-sensitive dilatant materials". In: *Journal of the Mechanics and Physics of Solids* 23.6, pp. 371–394.
Scambos, T. A., J. A. Bohlander, C. A. Shuman, and P. Skvarca (2004). "Glacier acceleration and thinning after ice shelf collapse in the Larsen B embayment, Antarctica". In: *Geophysical Research Letters* 31.18.
Schellart, W. P. (2000). "Shear test results for cohesion and friction coefficients for different granular materials: scaling implications for their usage in analogue modelling". In: *Tectonophysics* 324.1, pp. 1–16.
Schofield, A. N. and P. Wroth (1968). *Critical State Soil Mechanics*. McGraw-Hill London.
Schoof, C. (2005). "The effect of cavitation on glacier sliding". In: *Proceedings of the Royal Society of London A*. Vol. 461. 2055. The Royal Society, pp. 609–627.
— (2006). "A variational approach to ice stream flow". In: *Journal of Fluid Mechanics* 556.1, pp. 227–251.
— (2007). "Pressure-dependent viscosity and interfacial instability in coupled ice–sediment flow". In: *Journal of Fluid Mechanics* 570, pp. 227–252.
— (2010a). "Coulomb friction and other sliding laws in a higher order glacier flow model". In: *Math. Models. Meth. Appl. Sci* 20.1, pp. 157–189.
— (2010b). "Ice-sheet acceleration driven by melt supply variability". In: *Nature* 468.7325, pp. 803–806.
Schulz, W. H., J. W. Kean, and G. Wang (2009). "Landslide movement in southwest Colorado triggered by atmospheric tides". In: *Nature Geoscience* 2.12, pp. 863–866.
Schwartz, F. W. and H. Zhang (2003). *Fundamentals of Ground Water*. Wiley New York.
Segall, P. (2010). *Earthquake and Volcano deformation*. Princeton University Press.
Sergienko, O. V. and R. C. A. Hindmarsh (2013). "Regular Patterns in Frictional Resistance of Ice-Stream Beds Seen by Surface Data Inversion". In: *Science* 342.6162, pp. 1086–1089.
Shamy, U. E. and M. Zeghal (2005). "Coupled Continuum-Discrete Model for Saturated Granular Soils". In: *Journal of Engineering Mechanics* 131.4, pp. 413–426.
Shoemaker, E. M. (1986). "Subglacial hydrology for an ice sheet resting on a deformable aquifer". In: *Journal of Glaciology* 32.110, pp. 20–30.
Spiegel, M. R., S. Lipschutz, and J Liu (1968). *Schaum's Outlines Mathematical Handbook of Formulas and Tables*. Schaum Pub. Co.
Stevens, L. A., M. D. Behn, J. J. McGuire, S. B. Das, I. Joughin, T. Herring, D. E. Shean, and M. A. King (2015). "Greenland supraglacial lake drainages triggered by hydrologically induced basal slip". In: *Nature* 522.7554, pp. 73–76.
Stokes, C. R., C. D. Clark, O. B. Lian, and S. Tulaczyk (2007). "Ice stream sticky spots: a review of their identification and influence beneath contemporary and palaeo-ice streams". In: *Earth-Science Reviews* 81.3–4, pp. 217–249.

Sun, Q., G. Wang, and Y. Xu (2001). “DEM applications to aeolian sediment transport and impact process in saltation”. In: *Particulate science and technology* 19.4, pp. 339–353.
Swithinbank, C. W. M. (1954). “Ice streams”. In: *Polar Record* 7.48, pp. 185–186.
Tchalenko, J. S. (1970). “Similarities between shear zones of different magnitudes”. In: *Geological Society of America Bulletin* 81.6, pp. 1625–1640.
Tedesco, M., ed. (2015). *Remote Sensing of the Cryosphere*. Wiley Blackwell.
Temam, R. (1969). “Sur l’approximation de la solution des équations de Navier-Stokes par la méthode des pas fractionnaires (II)”. In: *Archive for Rational Mechanics and Analysis* 33.5, pp. 377–385.
Terzaghi, K. (1943). *Theoretical Soil Mechanics*. Wiley.
— (1951). *Mechanism of landslides*. Harvard University, Department of Engineering.
Terzaghi, K., R. B. Peck, and G. Mesri (1996). *Soil mechanics in engineering practice*. John Wiley & Sons.
Thomas, R. et al. (2004). “Accelerated sea-level rise from West Antarctica”. In: *Science* 306.5694, pp. 255–258.
Thomason, J. F. and N. R. Iverson (2006). “Microfabric and microshear evolution in deformed till”. In: *Quaternary Science Reviews* 25.9-10, pp. 1027–1038.
— (2008). “A laboratory study of particle ploughing and pore-pressure feedback: A velocity-weakening mechanism for soft glacier beds”. In: *Journal of Glaciology* 54.184, pp. 169–181.
Thompson, J., M. Simons, and V. C. Tsai (2014). “Modeling the elastic transmission of tidal stresses to great distances inland in channelized ice streams”. In: *The Cryosphere* 8.6, pp. 2007–2029.
Topin, V., F. Dubois, Y. Monerie, F. Perales, and A. Wachs (2011). “Micro-rheology of dense particulate flows: Application to immersed avalanches”. In: *Journal of Non-Newtonian Fluid Mechanics* 166.1, pp. 63–72.
Truffer, M., W. D. Harrison, and K. A. Echelmeyer (2000). “Glacier motion dominated by processes deep in underlying till”. In: *Journal of Glaciology* 46.153, pp. 213–221.
Tsuji, T., T. Kawaguchi, and T. Tanaka (1993). “Discrete particle simulation of 2-dimensional fluidized-bed”. In: *Powder Technology* 77, pp. 79–87.
Tsuji, Y., T. Tanaka, and T. Ishida (1992). “Lagrangian numerical simulation of plug flow of cohesionless particles in a horizontal pipe”. In: *Powder Technology* 71, pp. 239–250.
Tulaczyk, S. M., R. P. Sherer, and C. D. Clark (2001). “A ploughing model for the origin of weak tills beneath ice streams: a qualitative treatment”. In: *Quaternary International* 86, pp. 59–70.
Tulaczyk, S. (1999). “Ice sliding over weak, fine-grained tills: dependence of ice-till interactions on till granulometry”. In: *Geological Society of America Special Papers* 337, pp. 159–177.
— (2006). “Scale independence of till rheology”. In: *Journal of Glaciology* 52.178, pp. 377–380.
Tulaczyk, S., B. Kamb, R. P. Scherer, and H. F Engelhardt (1998). “Sedimentary processes at the base of a West Antarctic ice stream: constraints from textural and compositional properties of subglacial debris”. In: *Journal of Sedimentary Research* 68.3.

Tulaczyk, S., W. B. Kamb, and H. F. Engelhardt (2000a). “Basal mechanics of ice stream B, West Antarctica I. Till mechanics”. In: *Journal of Geophysical Research* 105.B1, pp. 463–481.
— (2000b). “Basal mechanics of ice stream B, West Antarctica II. Undrained plastic-bed model”. In: *Journal of Geophysical Research* 105.B1, pp. 483–494.
Turrin, J. B., R. R. Forster, J. M. Sauber, D. K. Hall, and R. L. Bruhn (2014). “Effects of bedrock lithology and subglacial till on the motion of Ruth Glacier, Alaska, deduced from five pulses from 1973 to 2012”. In: *Journal of Glaciology* 60.222, p. 771.
Tylmann, K., J. A. Piotrowski, and W. Wysota (2013). “The ice/bed interface mosaic: deforming spots intervening with stable areas under the fringe of the Scandinavian Ice Sheet at Sampława, Poland”. In: *Boreas* 42.2, pp. 428–441.
Vaughan-Hirsch, D. P., E. Phillips, J. R. Lee, and J. K. Hart (2013). “Micromorphological analysis of poly-phase deformation associated with the transport and emplacement of glaciotectonic rafts at West Runton, north Norfolk, UK”. In: *Boreas* 42, pp. 376–394.
Wafid, M. A., K. Sassa, H. Fukuoka, and G. Wang (2004). “Evolution of shear-zone structure in undrained ring-shear tests”. In: *Landslides* 1.2, pp. 101–112.
Walder, J. S. and A. Fowler (1994). “Channelized subglacial drainage over a deformable bed”. In: *Journal of Glaciology* 40.134.
Walker, R. T., K. Christianson, B. R. Parizek, S. Anandakrishnan, and R. B. Alley (2012). “A viscoelastic flowline model applied to tidal forcing of Bindschadler Ice Stream, West Antarctica”. In: *Earth and Planetary Science Letters* 319, pp. 128–132.
Walker, R. T., B. R. Parizek, R. B. Alley, S. Anandakrishnan, K. L. Riverman, and K. Christianson (2013). “Ice-shelf tidal flexure and subglacial pressure variations”. In: *Earth and Planetary Science Letters* 361, pp. 422–428.
Walton, O. R. and R. L. Braun (1986). “Viscosity, granular-temperature, and stress calculations for shearing assemblies of inelastic, frictional disks”. In: *Journal of Rheology* 30.5, pp. 949–980.
Wang, B., K. W. Chu, and A. B. Yu (2007). “Numerical study of particle-fluid flow in a hydrocyclone”. In: *Industrial & Engineering Chemistry Research* 46.13, pp. 4695–4705.
Wang, Y. (2009). “A new algorithm to model the dynamics of 3-D bonded rigid bodies with rotations”. In: *Acta Geotechnica* 4.2, pp. 117–127.
Wang, Y., S. Abe, S. Latham, and P. Mora (2006). “Implementation of particle-scale rotation in the 3-D lattice solid model”. In: *Pure and Applied Geophysics* 163.9, pp. 1769–1785.
Weatherley, D., B. Wruck, W. Hancock, and G. P Chitombo (2012). “Investigations on comminution of sheared prismatic granular materials using the discrete element method”. In: *Geophysical Research Abstracts*. Vol. 14. EGU General Assembly 2012.
Weertman, J. (1957). “On the sliding of glaciers”. In: *Journal of Glaciology* 3.21, pp. 33–38.
— (1968). “Diffusion law for the dispersion of hard particles in an ice matrix that undergoes simple shear deformation”. In: *Journal of Glaciology* 7.50, pp. 161–165.
Wel, N., P. Christoffersen, and M. Bougamont (2013). “The influence of subglacial hydrology on the flow of Kamb Ice Stream, West Antarctica”. In: *Journal of Geophysical Research: Earth Surface* 118.1, pp. 97–110.

Wen, C. and Y. Yu (1966). “Mechanics of fluidization”. In: *Chemical Engineering Progress* 62.62, pp. 100–111.
Werder, M. A., I. J. Hewitt, C. G. Schoof, and G. E. Flowers (2013). “Modeling channelized and distributed subglacial drainage in two dimensions”. In: *Journal of Geophysical Research: Earth Surface* 118.4, pp. 2140–2158.
Werner, B. T. (1995). “Eolian dunes: computer simulations and attractor interpretation”. In: *Geology* 23.12, pp. 1107–1110.
Whillans, I. M. and C. J. van der Veen (1997). “The role of lateral drag in the dynamics of Ice Stream B, Antarctica”. In: *Journal of Glaciology* 43.144, pp. 231–237.
Whipple, K. X. and G. E. Tucker (1999). “Dynamics of the stream-power river incision model: Implications for height limits of mountain ranges, landscape response timescales, and research needs”. In: *Journal of Geophysical Research: Solid Earth* 104.B8, pp. 17661–17674.
Wilcock, P. R. (1998). “Two-fraction model of initial sediment motion in gravel-bed rivers”. In: *Science* 280.5362, pp. 410–412.
Willis, I. C. (1995). “Intra-annual variations in glacier motion: a review”. In: *Progress in Physical Geography* 19.1, pp. 61–106.
Winberry, J. P., S. Anandakrishnan, R. B. Alley, R. A. Bindschadler, and M. A. King (2009). “Basal mechanics of ice streams: Insights from the stick-slip motion of Whillans Ice Stream, West Antarctica”. In: *Journal of Geophysical Research* 114, F01016.
Winberry, J. P., S. Anandakrishnan, D. A. Wiens, R. B. Alley, and K. Christianson (2011). “Dynamics of stick–slip motion, Whillans Ice Stream, Antarctica”. In: *Earth and Planetary Science Letters* 305.3, pp. 283–289.
Wuite, J., H. Rott, M. Hetzenecker, D. Floricioiu, J. De Rydt, G. H. Gudmundsson, T. Nagler, and M. Kern (2015). “Evolution of surface velocities and ice discharge of Larsen B outlet glaciers from 1995 to 2013”. In: *The Cryosphere* 9.3, pp. 957–969.
Xu, B. H. and A. B. Yu (1997). “Numerical simulation of the gas-solid flow in a fluidized bed by combining discrete particle method with computational fluid dynamics”. In: *Chemical Engineering Science* 52.16, pp. 2785–2809.
Xu, B. H., Y. Q. Feng, A. B. Yu, S. J. Chew, and P. Zulli (2001). “A numerical and experimental study of the gas-solid flow in a fluid bed reactor”. In: *Powder Handling and Processing* 13.1, pp. 71–76.
Yao, M. and A. Anandarajah (2003). “Three-Dimensional Discrete Element Method of Analysis of Clays”. In: *Journal of Engineering Mechanics* 129.
Yohannes, B., L. Hsu, W. E. Dietrich, and K. M. Hill (2012). “Boundary stresses due to impacts from dry granular flows”. In: *Journal of Geophysical Research* 117.F2, F02027.
Zhang, Y. and C. S. Campbell (1992). “The interface between fluid-like and solid-like behaviour in two-dimensional granular flows”. In: *J. Fluid Mech* 237, p. 541.
Zhao, J. and T. Shan (2013). “Coupled CFD-DEM simulation of fluid-particle interaction in geomechanics”. In: *Powder Technology* 239, pp. 248–258.
Zhou, Z. Y., S. B. Kuang, K. W. Chu, and A. B. Yu (2010). “Discrete particle simulation of particle-fluid flow: model formulations and their applicability”. In: *Journal of Fluid Mechanics* 661, pp. 482–510.
Zhu, H. P., Z. Y. Zhou, R. Y. Yang, and A. B. Yu (2007). “Discrete particle simulation of particulate systems: Theoretical developments”. In: *Chemical Engineering Science* 62, pp. 3378–3396.

Zoet, L. K. and N. R. Iverson (2015). “Experimental determination of a double-valued drag relationship for glacier sliding”. In: *Journal of Glaciology* 61.225.
Zwally, H. J., W. Abdalati, T. Herring, K. Larson, J. Saba, and K. Steffen (2002). “Surface Melt-Induced Acceleration of Greenland Ice-Sheet Flow”. In: *Science* 297.5579, pp. 218–222.

Index